HIGH FIELD ELECTRON SPIN RESONANCE IN THE HALDANE MATERIALS

by

Koichi KINDO

DISSERTATION IN PHYSICS

THE OSAKA UNIVERSITY

GRADUATE SCHOOL OF SCIENCE

TOYONAKA, OSAKA

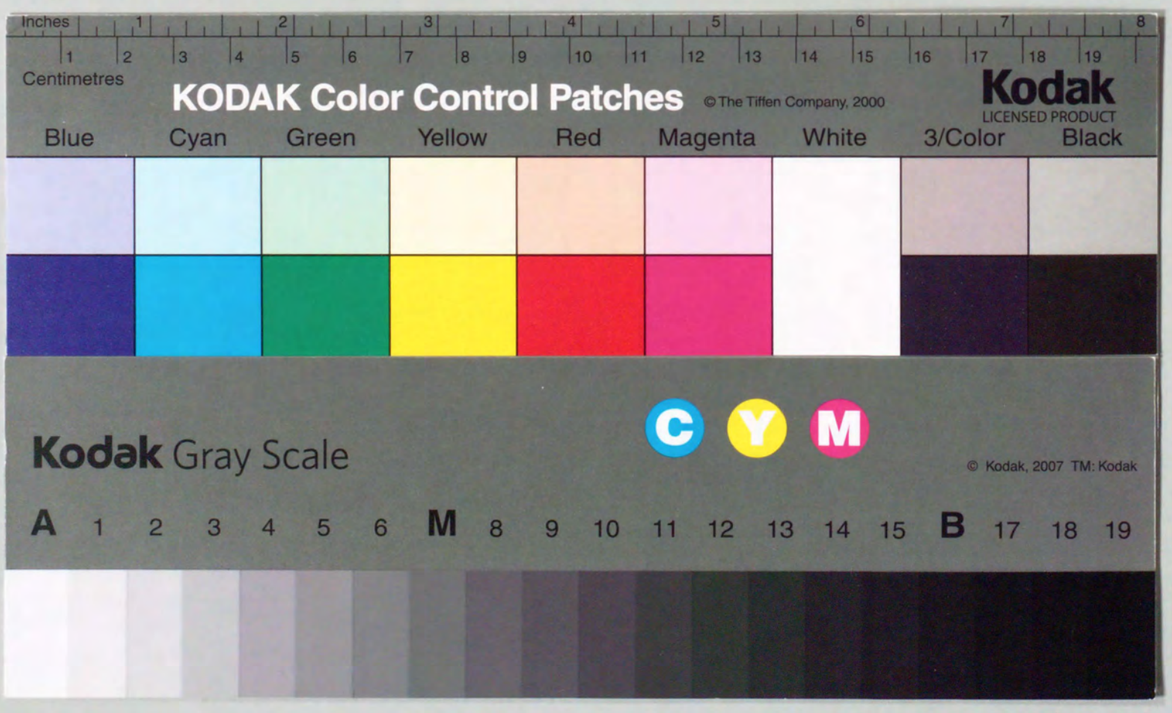

HIGH FIELD ELECTRON SPIN RESONANCE

IN

THE HALDANE MATERIALS

by

Koichi KINDO

DISSERTATION IN PHYSICS

THE OSAKA UNIVERSITY

GRADUATE SCHOOL OF SCIENCE

TOYONAKA, OSAKA

FEBRUARY, 1992

CONTENTS

PART I

TECHNIQUES FOR MICROWAVE ELECTRON SPIN RESONANCE IN PULSED HIGH MAGNETIC FIELD

ABSTRACT

Experimental techniques of microwave Electron Spin Resonance (ESR) spectroscopy in pulsed high magnetic field are described. Microwaves with the wave length of 6 ~ 8 mm are tested in the system. The standard reflection type wave guide system is used for the spectrometer with the pulsed magnetic field up to 40 Tesla with the width of 40 msec. Both the rectangular and cylindrical resonant cavities are tested and the latter system gives better results. Typical applications for paramagnetic and antiferromagnetic materials are presented. CuO, a parent material of the oxide high T_c superconductors, is investigated and a very broad paramagnetic resonance line is found. The linewidth is larger than one Tesla and it is proved that the pulse field resonance is better than usual field modulation method when the linewidth is extremely large. Other two examples, the antiferromagnetic resonance (AFMR) in Nd_2CuO_4 and Mn impurity spin resonance in $CsCoCl_3$ are described.

1. Introduction

The electron spin resonance (ESR) gives informations around the resonance center and much work has been done in various magnetic systems. Recently, there is an increasing interest in highly correlated electron systems such as heavy fermions[1], high T_c superconductors[2], low dimensional frustrating spin systems[3] and Haldane materials[4]. Generally speaking, however, the spin resonance in these systems needs wide energy range with high magnetic field because the highly correlated electron systems are also ruled by strong spin-spin correlations and the resonance condition is scattered from usual paramagnetic framework. Therefore, the standard X-band ESR spectrometer is not enough to cover these resonances. The present thesis aims to describe the development of a new ESR equipment combined with a pulsed high field so as to be able to observe broad and weak resonance lines in highly correlated spin systems.

During last several decades a number of researchers have constructed high magnetic field facilities on pulsed or static manner. The pulsed field techniques were pioneered by Kapitza[5] around 1925. He first used a battery discharge through a small low resistance coil. Later, he developed an electromechanical system by which stored kinetic energy in a rotor was transferred to a magnet coil to produce over 30 Tesla(T)[6]. On the other hand, Bitter constructed a D.C. high field magnets at MIT[7] and this was a breakthrough in high D.C. field beyond the iron core magnet system. Nowadays, the superconducting magnet can produce

D.C. field up to about 20 T[8] and a steady field of 31.1 T is produced by the hybrid magnet[9].

So far, the magnetic field higher than 40 T can only be obtained by the pulsed system. The maximum field attainable is limited by the mechanical strength of the coil. Date[10] avoided this difficulty by using multi-layer coil and produced a field of 107 T. The current densities of all coils are controlled so as to keep equal forces within the material strength. For practical use, one-layer coil with maximum field of 50 T in 60 mm bore and two-layer coil with 70 T in 20 mm bore are available with pulse duration of 0.4 msec.

Many kinds of measurements such as the magnetization, magneto-resistance, magneto-striction, magneto-optics and submillimeter wave or far infrared electron spin resonance (FIR-ESR) have been carried out by using a series of multi-layer coils in the High Magnetic Field Laboratory at the Research Center for Extreme Materials of Osaka University[11]. The standard pulse magnets in Osaka University first established as the multilayer coils are now called "short-pulse magnet" because the pulse width is less than 1 msec. The short-pulse magnets are regarded as the central facility in our Research Center because the maximum field is 70 Tesla(T) and the experiments below 1 K are also available. In FIR-ESR, for example, much work such as a discovery of Si^3 term[12], experiment of exchange splitting[13] and various resonances in low dimensional magnets[14] has been done. However, the short-pulse magnet is not convenient for the microwave ESR because the usual metallic resonant cavity is not applicable to the ESR study because of a heavy eddy current

effect and a strong squeezed force acting on the cavity. Considering these facts, we have developed another "long-pulse magnet" with the pulse width of 40 msec. Although the maximum field is 40 T and it is about half of the short-pulse magnet, the skin depth is about ten times larger than in the short-pulse magnet and the difficulty in the cavity design is removed. The Part I of the present paper gives the technical development of the microwave ESR in use of the long-pulse magnet.

Historically speaking, high field ESR in the microwave region was initiated by Foner[15] in 1957 in National Magnet Laboratory of MIT. He used so called Foner-Kolm magnet which is made of beryllium-copper helix coil. He observed AFMR in MnF_2[15] and Cr_2O_3[16] and EPR with large zero-field splittings such as V^{3+} in Al_2O_3[17]. However, his magnet was not so convenient for general microwave measurement because of the short pulse duration of about μsec. Moreover, it was difficult to make a large and high quality pulse magnet with the Foner-Kolm design.

Soon after, Date and Motokawa begun to observe microwave high field ESR at Osaka University, using polyhelical coil with electrolytic capacitor bank which produced more conveient magnetic field up to 20 T in liquid helium dewar. They observed a new type magnetic resonance in $CoCl_2 2H_2O$[18] in 1965 and it was analyzed as the spin-cluster resonance[19], which was the first discovery of an excitation of localized magnons in the Ising-like spin system. The similar resonance was done in $FeCl_2$[20]. A typical high field AFMR was found in $NiCl_2 6H_2O$[21]. The impurity

spin resonance of Mn^{2+} in $CoCl_2 2H_2O$[22] and Mn^{2+} or Fe^{3+} in $FeCl_2$[23] were investigated to see the interaction between the host and the impurity spins.

In a decade of 1970, the microwave ESR work was closed in Osaka University because of the new development of multilayer magnet systems and main effort was pointed to the FIR-ESR, as is described. However, it is revitalized by the prsent author since the construction of a long-pulse magnet. The present paper describes the technical details in Part I and main experimental results with a special interest in the Haldane gap problem[4] will be shown in Part II.

2. Experimental System

2.1 Microwave System

Microwaves are generated by klystrons and the standard reflection type wave guide system is adopted, as shown in Fig. 1. No FM, AM and magnetic field modulations are used because these are inadequate to apply to the pulse field spin resonance. Therefore, the ESR sensitivity is not so high compared to the superheterodyne or field modulation systems. However, the transient ESR signal under the pulsed field scanning gives high frequency Fourier components which are amplified by a band-pass amplifier and the minimum detectable spins with the linewidth of one gauss are substantially in the order of 10^{15} spins/cc[22]. Moreover, the present method is very effective to observe broad resonance lines such as the width larger than 1 T, as will be shown later. Klystrons of 35V11 and 50V10 made by OKI Electrc Industries are used through the present study. The former generates 30~40 GHz and the latter gives around 50 GHz waves. The comparison diagram of the research region for the resonance energy covered by the present work and the FIR-ESR study is shown in Fig. 2. It is noted that the magnetic field of 40 T corresponds to the standard paramagnetic resonance of about 1 THz and use of Carcinotrons may be a desirable extension in future. The coaxial cavity may be necessary when low frequency microwaves, 10 GHz for example, are used. High Q-value of the cavity is not expected in this case so it is not tested in the present work.

In the previous work, Date and Motokawa used the

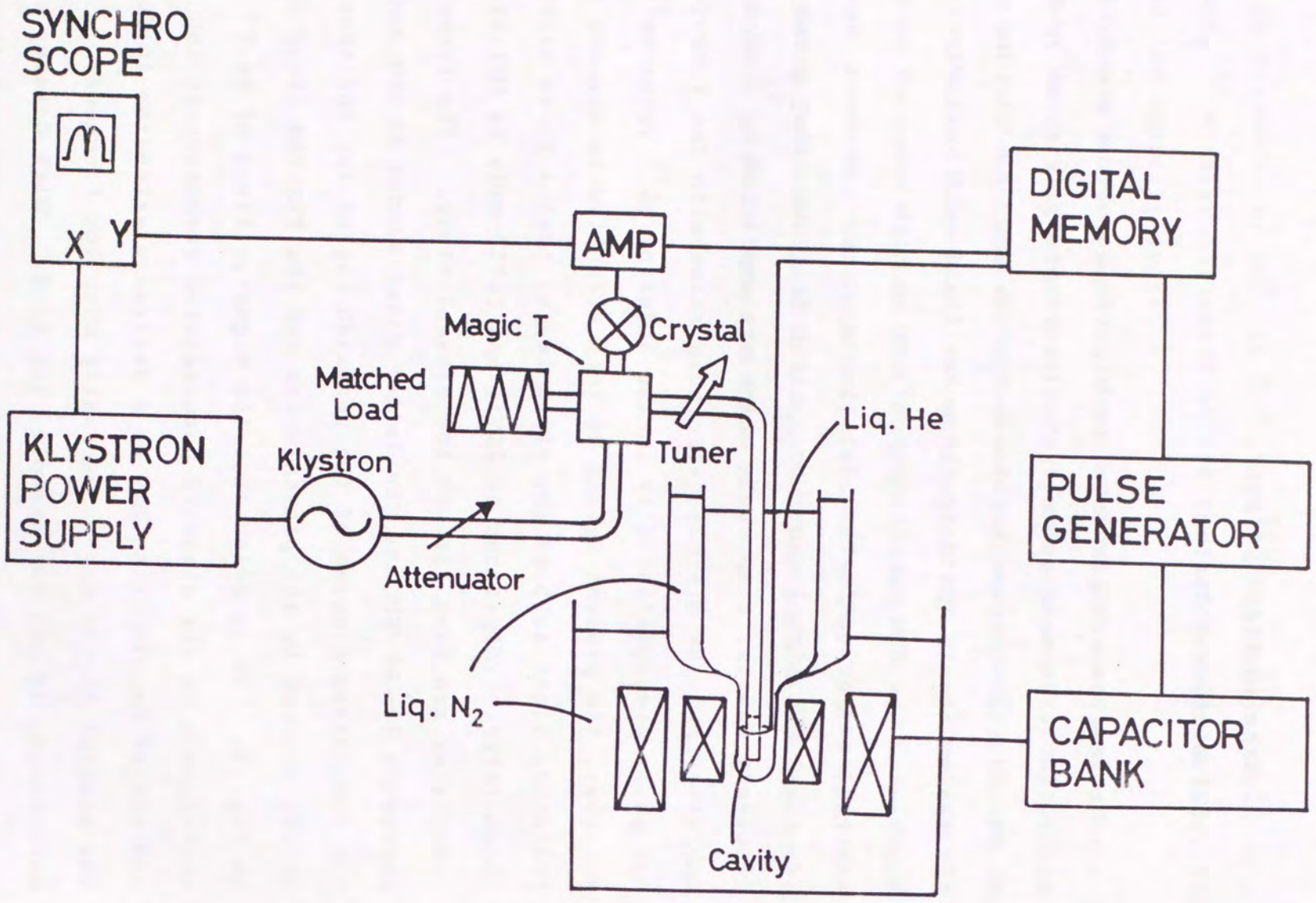

Fig. 1. Block diagram of microwave high-field ESR measurement.

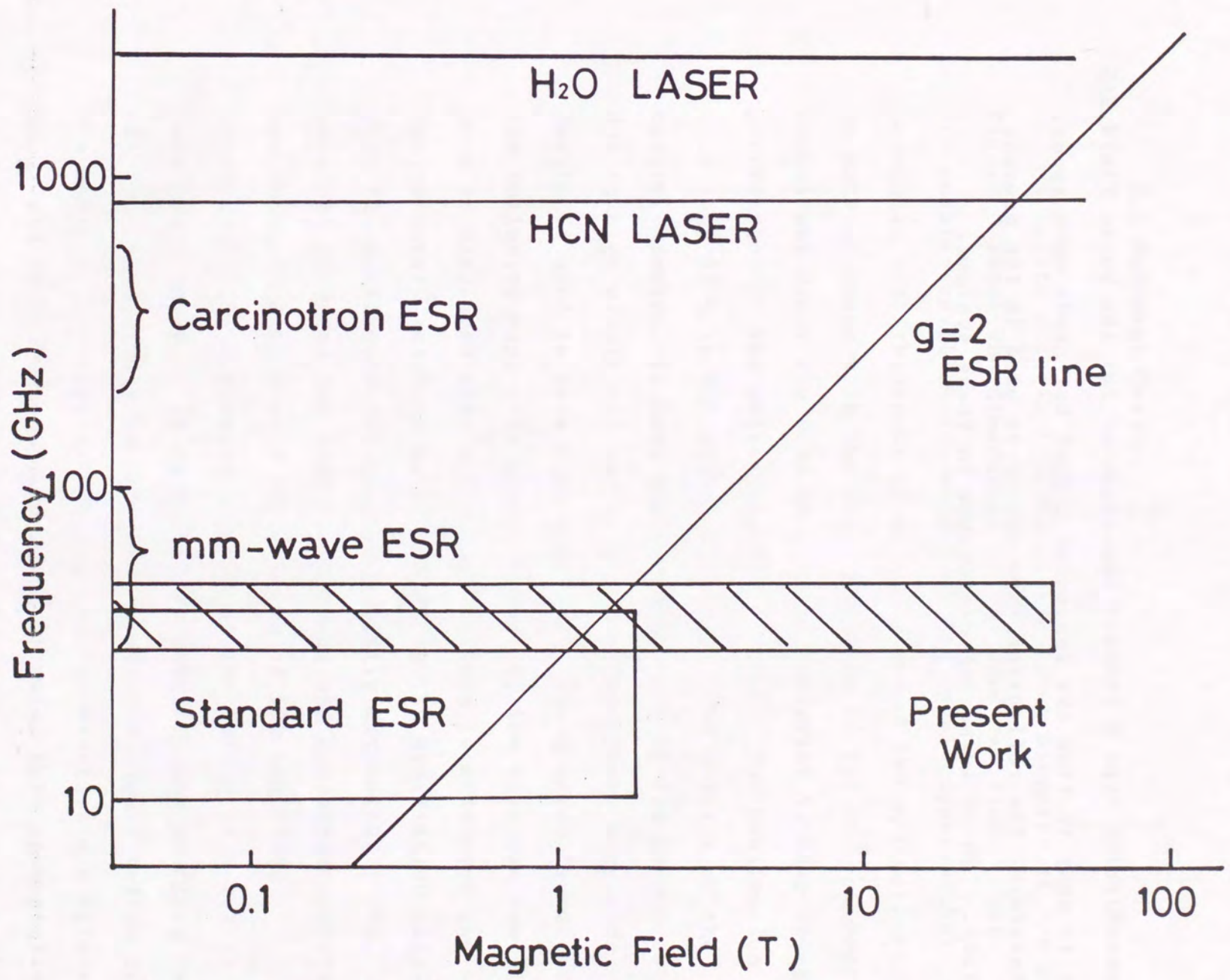

Fig. 2. Comparative diagram of the research region for the rf-energy versus magnetic field.

transmission type microwave spectrometer for the pulse field ESR. It is easy to find the resonance signal but needs much space. Therefore, the reflection type cavity is used in the present study. There is no big difference in these systems.

2.2 Resonant Cavity

A cavity size is limited by the inner diameter of the dewar. Figure 3 shows the dimensions of employed cavities. The rectangular cavities are made from the usual copper-nickel waveguide with thickness of 0.3~0.5 mm and the cylindrical cavity is made of brass with the wall thickness of 0.3 mm. Copper-nickel and brass are used as a cavity material to keep enough penetration of the pulsed magnetic field. The penetration is more than 99 % in our cavity systems. The Q-value of the cavity, however, is much smaller than that of the copper cavity due to high electrical resistivity. Therefore, a cylindrical cavity is used to have high Q-value. The Q-value is measured in the following way. As shown in Fig. 4, the klystron oscillation mode is displayed when reflection voltage is modulated and a dip due to cavity resonant mode appears in the oscillation mode. Then the Q-value of the cavity is easily estimated. The obtained Q-curves for both rectangular and cylindrical cavities are shown in Fig. 5 with the Q-value of 900 and 2500, respectively. A plunger is used at the bottom of a cavity to have best tuning. It is useful to insert choke plungers in the cavity. The cavity is shielded to prevent liquid helium inside. The modes of rectangular and cylindrical cavities are referred to TE_{10n} and TE_{11n} respectively, both of which have rf-magnetic field perpendicular to the pulsed field- direction at the bottom of the cavity, as shown in Fig. 6.

The optimum sensitivity is achieved by tuning the coupling coefficient β defined by the cavity Q-value Q_0 and the coupling Q

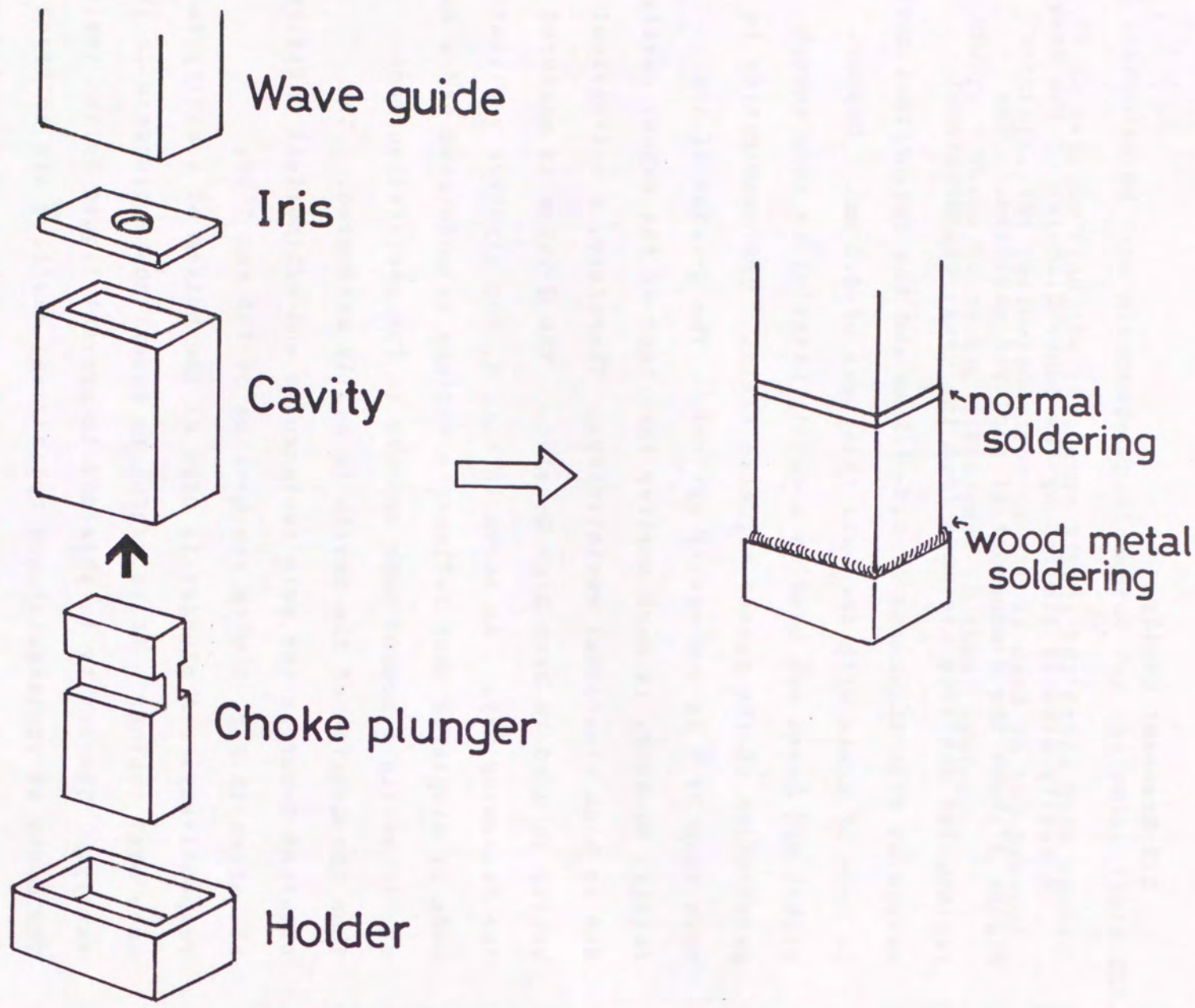

Fig. 3. Schematic view of cavity systems.

Fig. 4. FM-modulated display of cavity Q-curve.

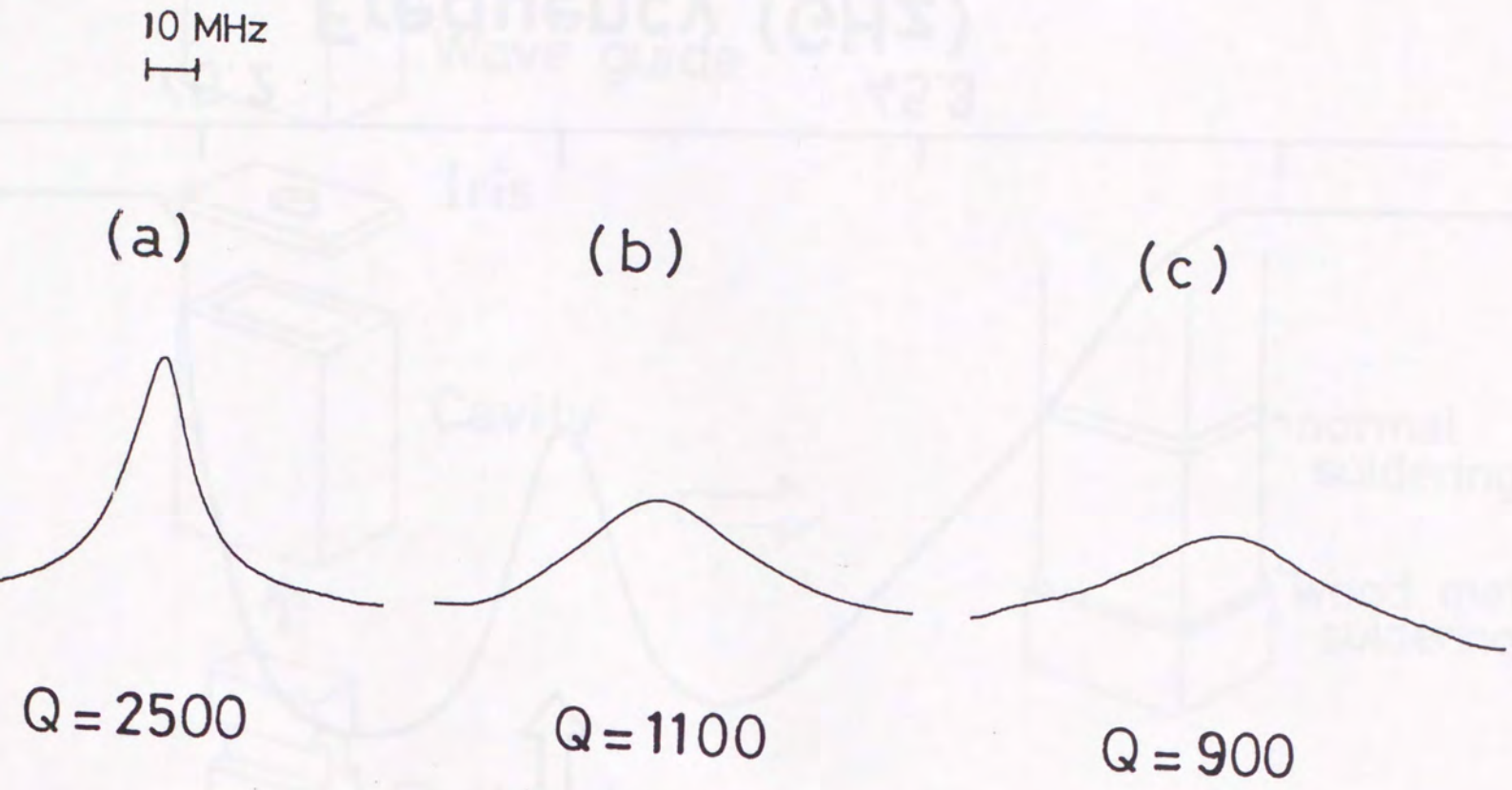

Fig. 5. Comparison of Q-curves of brass cavities with $\beta = 1$, $\lambda_g/2$ at room temperature. (a) Cylindrical cavity with choke, (b) cylindrical cavity without choke, (c) rectangular cavity with choke.

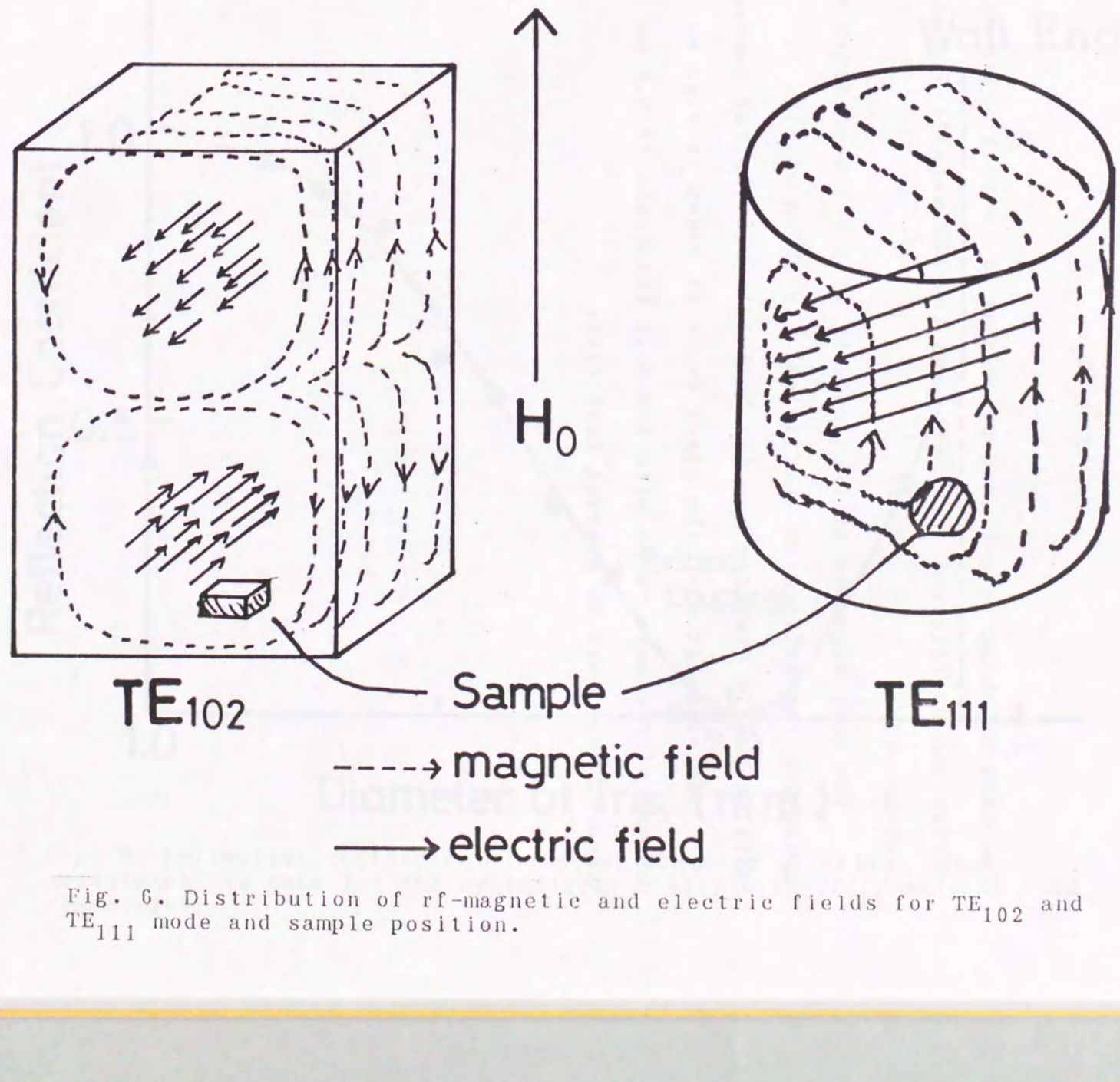

Fig. 6. Distribution of rf-magnetic and electric fields for TE_{102} and TE_{111} mode and sample position.

of Q_x as

$$\beta = Q_0 / Q_x . \qquad (1)$$

The best matching is achieved by chosing β to be 1 where the reflection coefficient Γ is zero and the ESR sensitivity has the maximum value.

The best diameter of the coupling iris has been detrmined by measuring the reflection coefficient, as shown in Fig. 7. Two millimeters in diameter was the best iris size in our case.

The cryostat with the glass dewar is shown in Fig. 8. German silver wave guide with the wall thickness of 0.3 mm is used in the dewar to prevent heat flow.

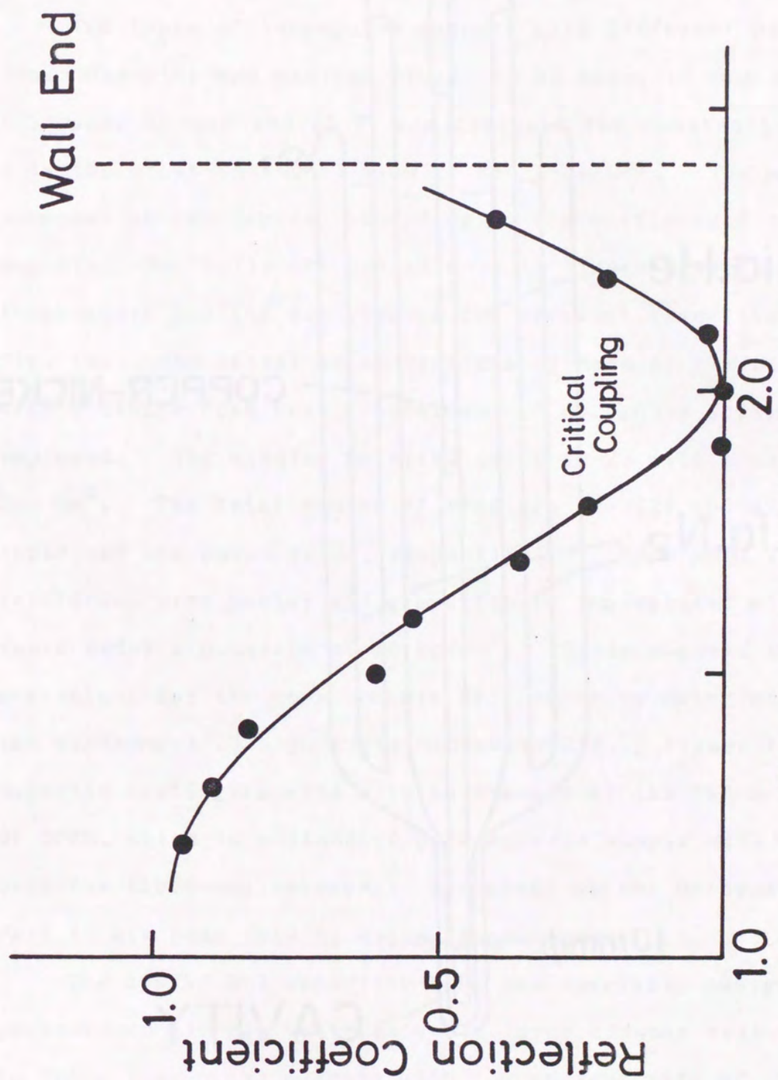

Fig. 7. Reflection coefficient Γ versus diameter of iris. The measurement is done for the cylindrical cavity with TE_{112} mode at room temperature.

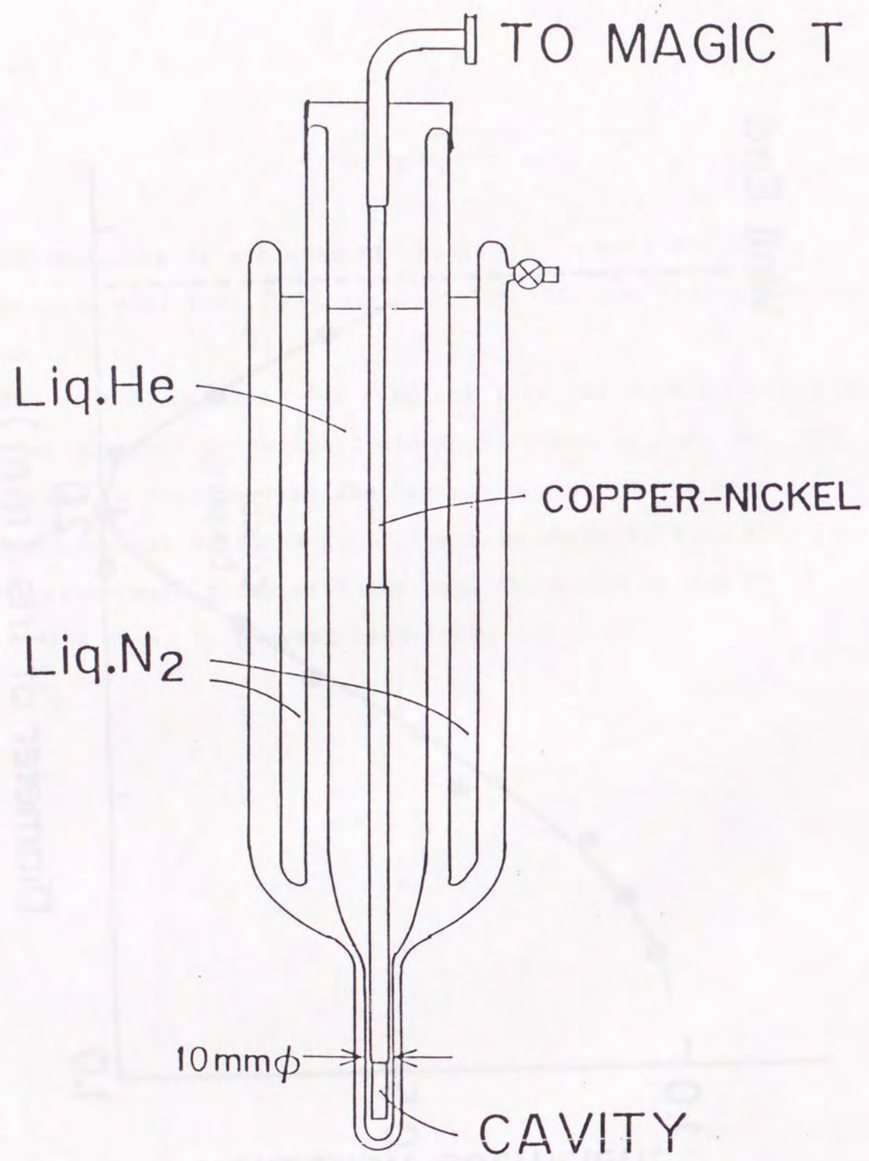

Fig. 8. Cut-view of the ESR cryostat setting in the dewar.

2.3 Pulsed Magnet

Two types of long-pulse magnets with different pulse width, inner diameter and maximum field (A: 80 msec, 18 mmϕ and 40 T; B: 150 msec, 28 mmϕ and 26 T) are designed and constructed. Figure 9 is the cross-sectional view of the A-magnet. The magnet is composed of two layers, according to the multi-layer theory of magnet. The coils are cooled down to liquid nitrogen temperature and the cut view of the cryostat vessel is shown in Fig. 10. The vessel is conventionally made of stainless bowl with urethane foam heat insulation and no vacuum system is employed. The winding material is Cu-Cr-Zr with a cross-section 2x3 mm^2. The total number of windings are 220 and 490 for the inner and the outer coils, respectively. Each coil is reinforced with Kevlar and glass fibers impregnated with epoxy resin under a pressure of 50 kg/cm^2. These magnets are convenient for the measurements of conductive materials and for the experiment of high-field microwave ESR. Figure 11 shows the magnetic field generated with an example of the ESR measurement of DPPH, which is a standard paramagnetic sample with g=2.0 and used for field-calibration. The study on the Haldane problem in Part II has been done by using the A-magnet.

The 500 kJ D-1 capacitor bank has specially designed pressurized air gap switches and a large crowbar resistance (1 Ω) to drive long-pulse magnets with low current rate of 10 kA.

A series of test of the pulse field effect on the copper pipes was done in the course of development as shown in Fig. 12. The metal tube is compressed by the force acting on the field-

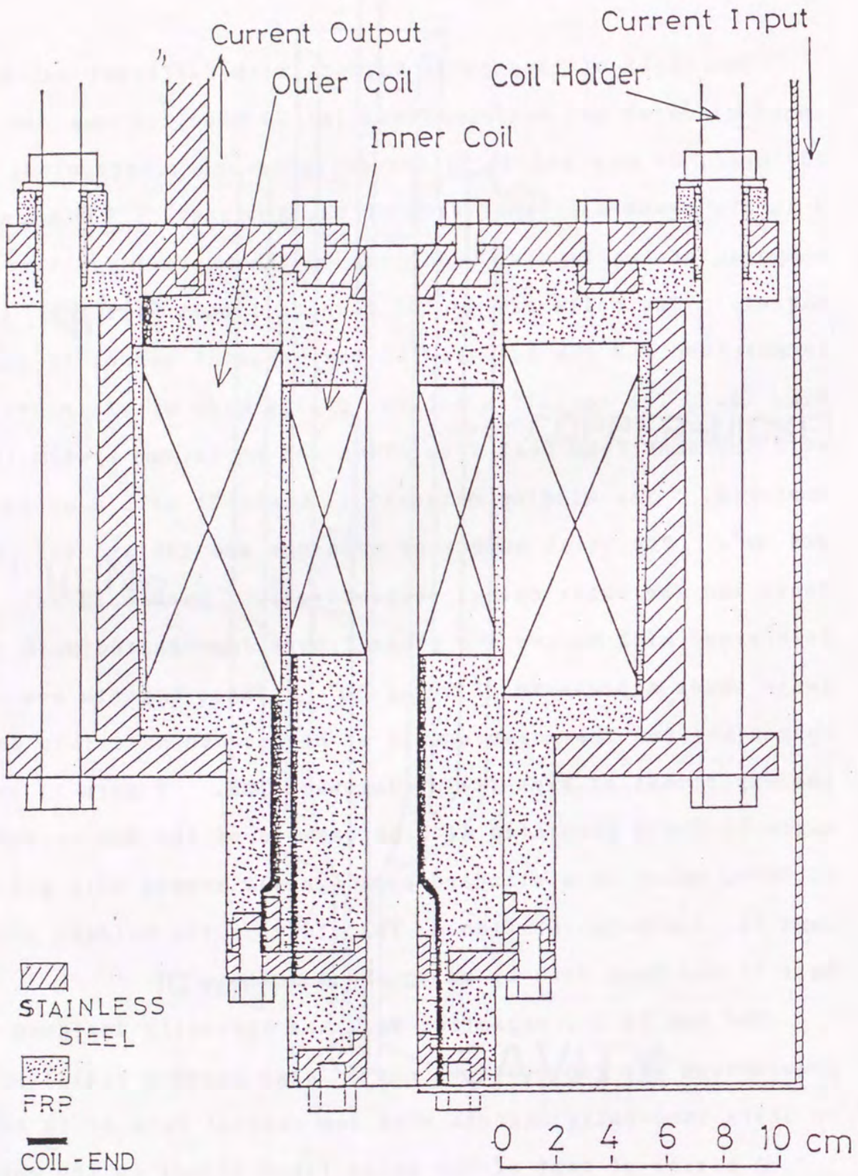

Fig. 9. Cut-view of the long-pulse magnet.

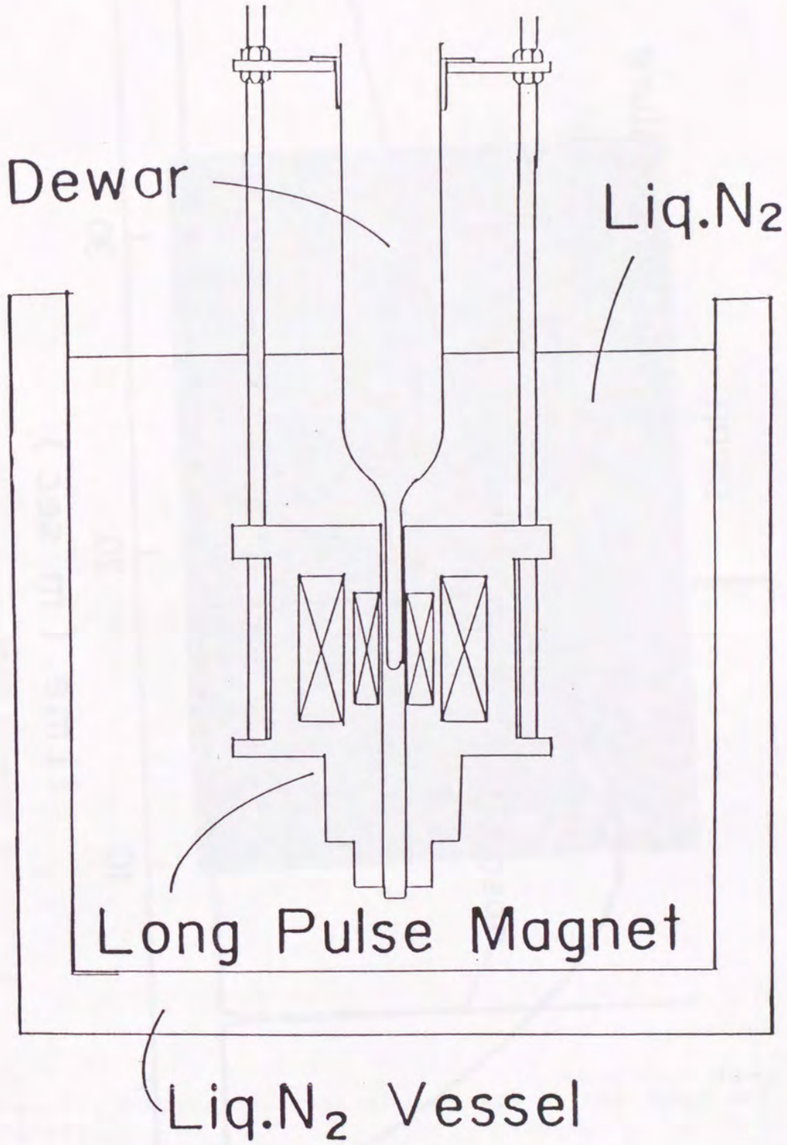

Fig. 10. Cut-view of the dewar setting in the long-pulse magnet and liquid nitrogen vessel.

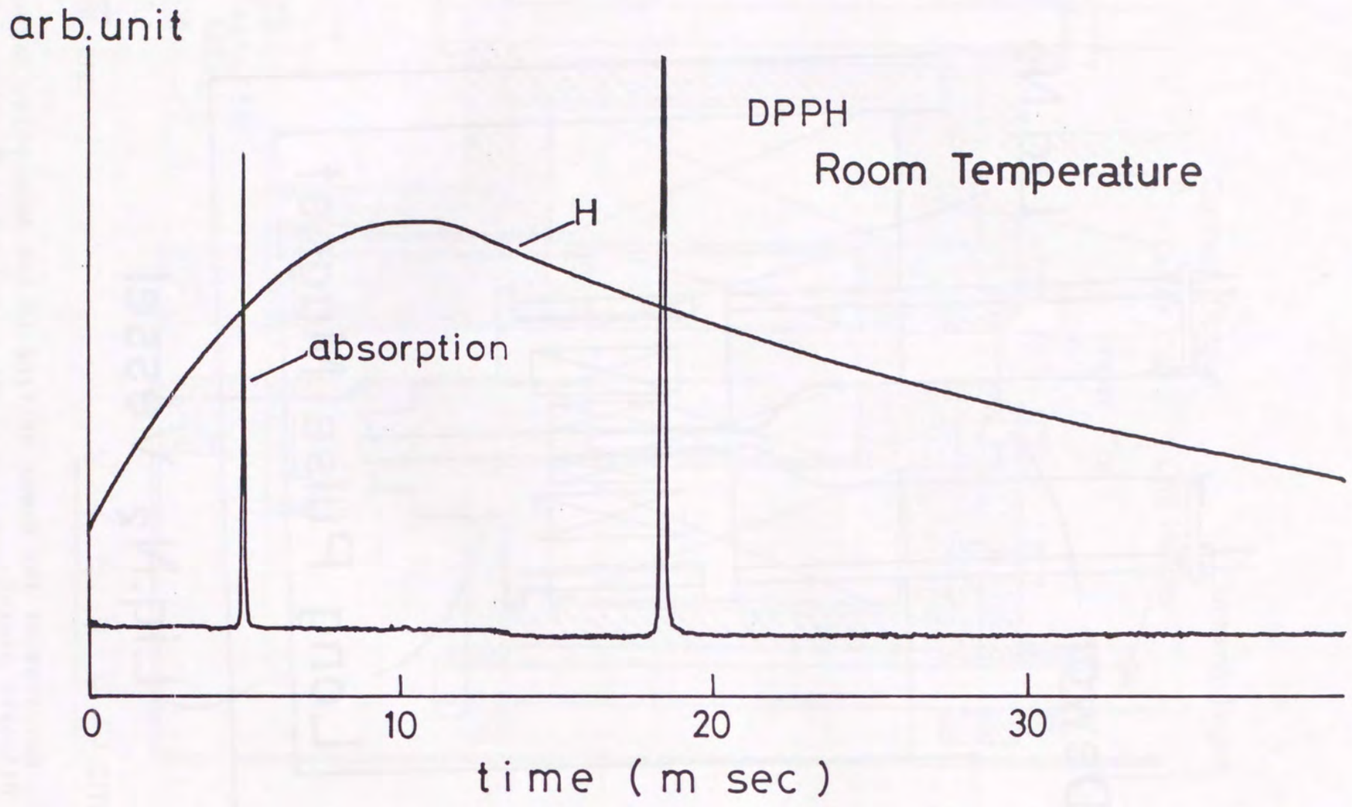

Fig. 11. Absorption curve of DPPH at room temperature and the curve of magnetic field.

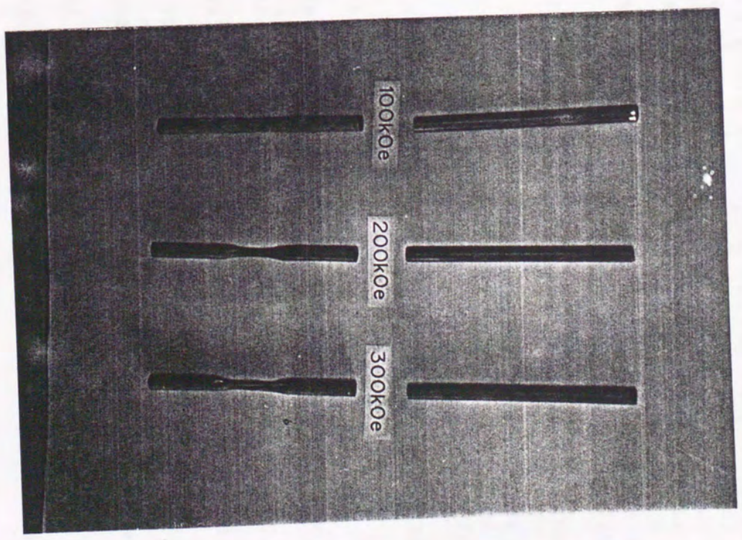

Fig. 12. Compression test of Cu-tubes by the long- and short- pulse magnets.

induced electrical current in the tube. The effect of the short-pulse magnet is seen in the lower photograph, where the copper tubes are squeezed seriously, whereas the upper tubes, exposed in the long-pulse magnet, are not deformed at all. Therefore, use of the long-pulse magnet is very effective when metal block are necessarily introduced in magnetic field.

2.4 Test Experiment for the System

ESR experimental test was done using paramagnetic $MnSO_4 4H_2O$ at room temperature and DPPH which is a standard paramagnetic sample with g=2.0 at liquid helium temperature. The data at room temperature are shown in Figs. 13 and 14. Two absorption peaks are found in Fig. 13: one is observed in the increasing field and the other is seen in the corresponding decreasing field. Figure 14 displays the magnetic resonance as a function of magnetic field. In decreasing temperature, the resonance frequency of the cavity shifts to the higher frequency due to the contraction of the cavity. The frequency shift from room temperature to liquid nitrogen temperature is large, whereas the shift below liquid nitrogen temperature is very small. The cavity was sealed by soldering wood metal to prevent liquid helium inside the cavity to avoid the resonant frequency shift and bubbling noise. Figure 15 shows the noise level of the cavity with liquid helium. A large noise level is quenched by extracting liquid helium from the cavity.

O_2 contamination in the cavity should also be noticed in the experimental process. As well known, O_2 molecule has spin $S=1$[24] and air contains 20 % of oxygen. The data shown in Fig. 16 are obtained when oscillatory magnetic field is applied. It is noted that zero field corresponds to the center of chart. the ESR absorption is seen from room temperature (O_2 gas) to liquid nytrogen temperature (O_2 liquid). The O_2 signal is eliminated by exchanging air with helium gas.

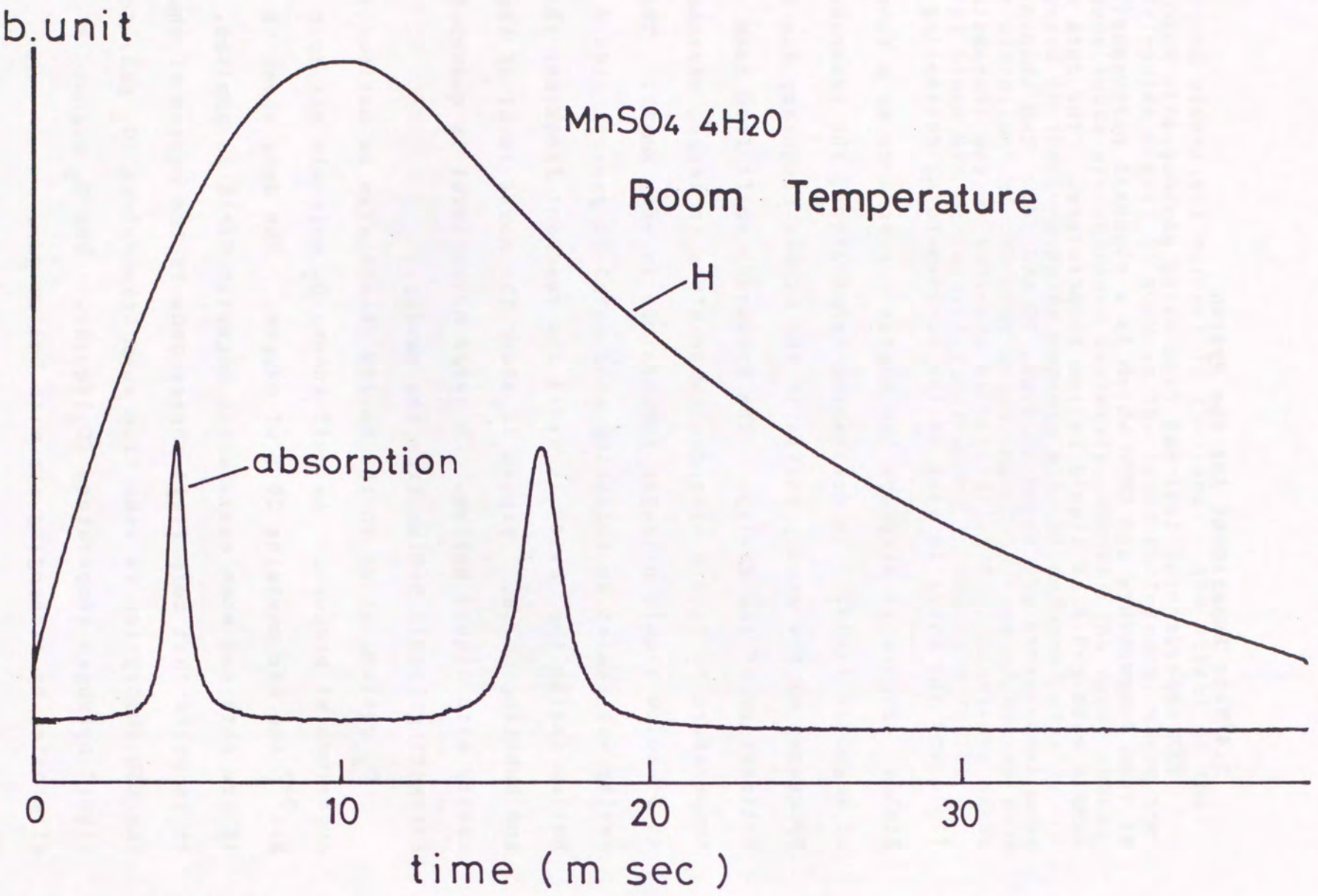

Fig. 13. Magnetic field profile and the absorption curve of $MnSO_4 4H_2O$ at room temperature.

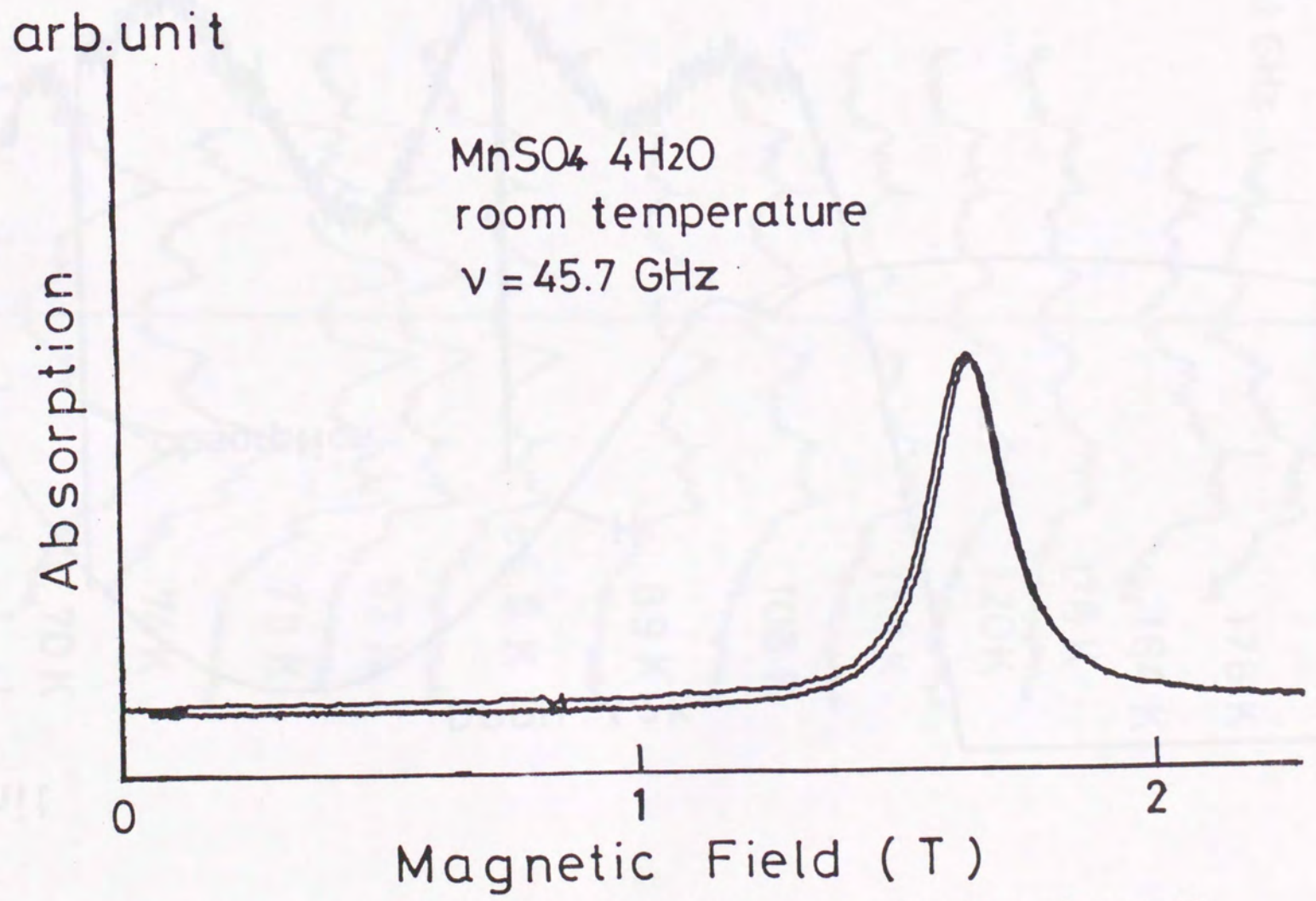

Fig. 14. The absorption curve of $MnSO_4 4H_2O$ as a function of magnetic field.

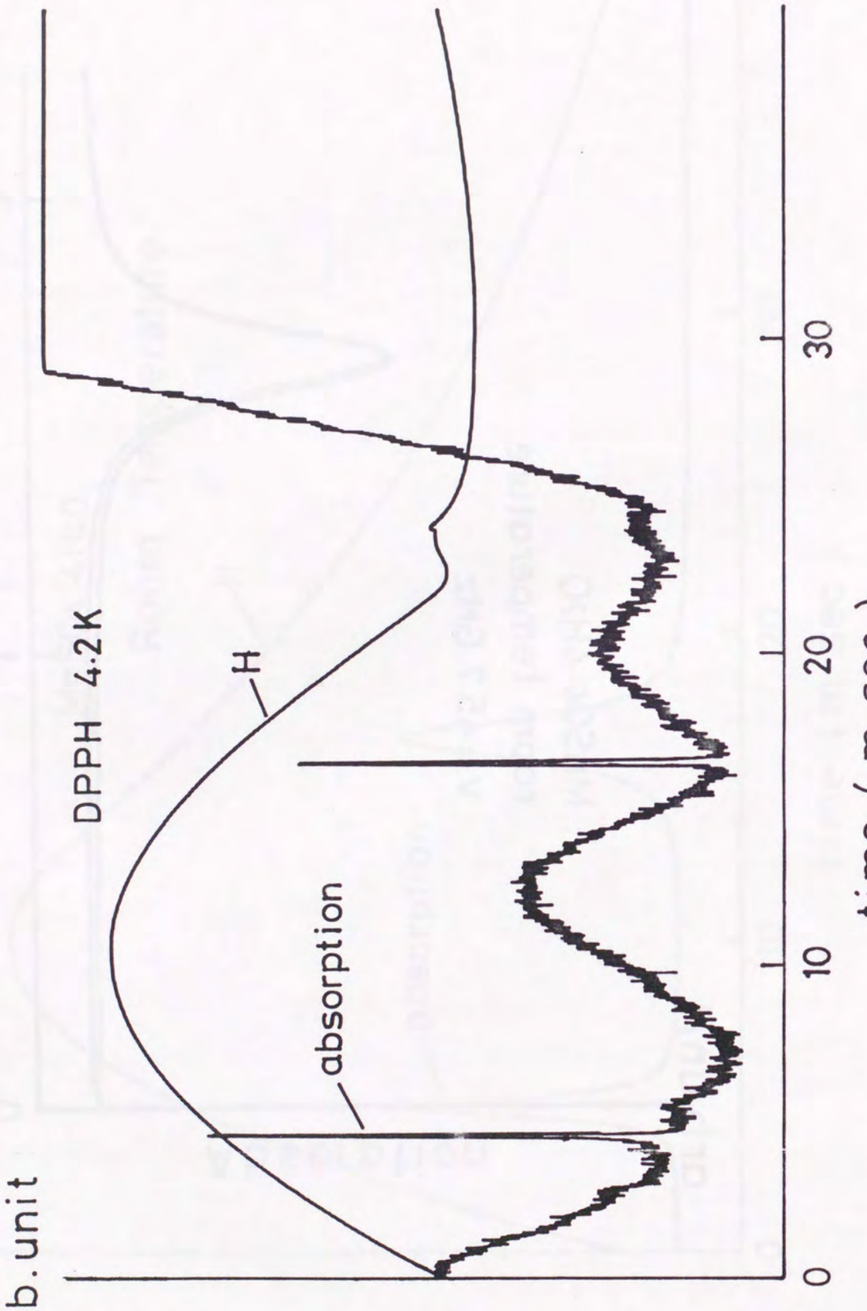

Fig. 15. Absorption curve of DPPH in liquid helium bubbling noise.

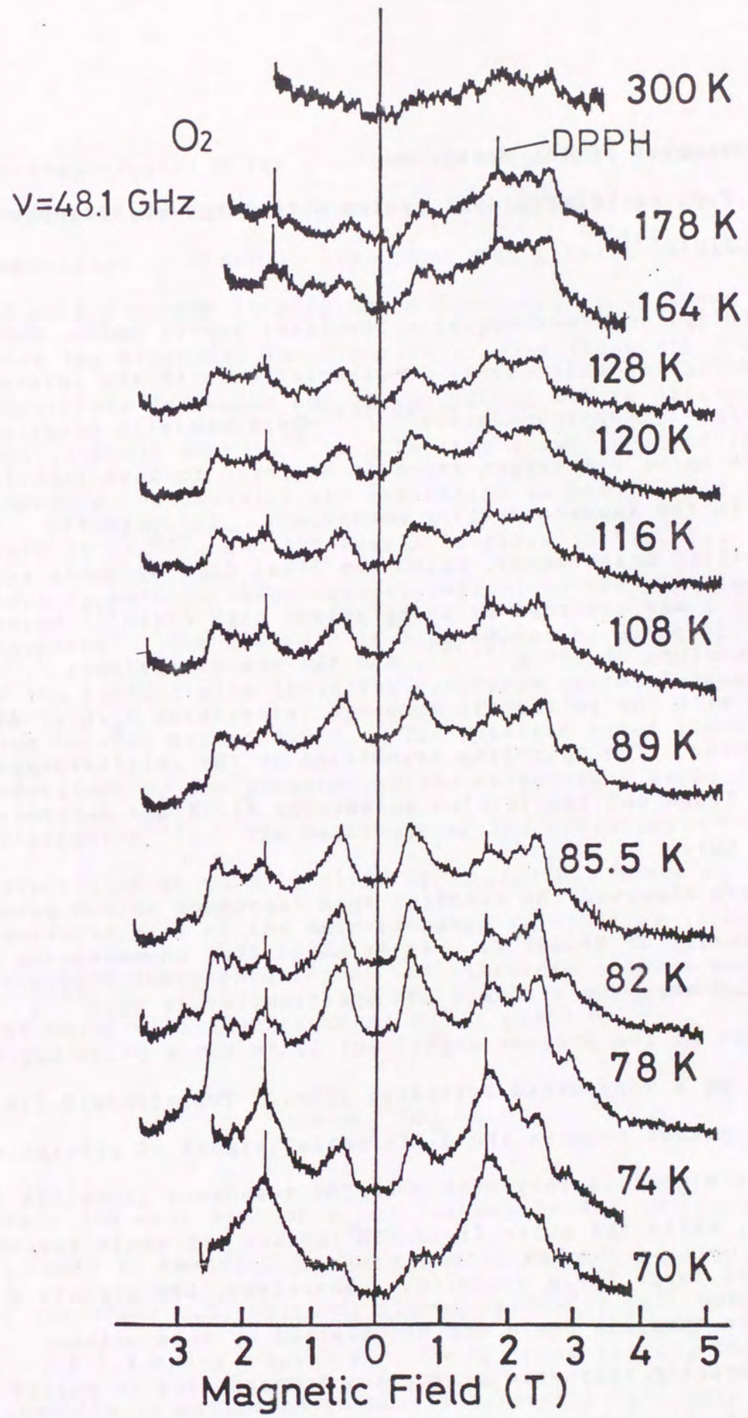

Fig. 16. Temperature dependence of ESR signal of O_2 gas and liquid.

3. Examples of the Measurement

3.1 CuO; one-dimensional system with large anisotropic exchange field[25)]

Recently, antiferromagnetic insulator cupric oxide, CuO, has been investigated extensively in association with the interest in cuprate high T_c superconductors[26-30)] where magnetic coupling between Cu spins via oxygen atoms is believed to have important relation to the superconducting mechanism. The magnetic susceptibility measurement, which was first done by Honda and Ishiwara[31)], was extended by using pulsed high field[27)] below the Neel temperature of 230 K[32,33)], and the one-dimensional character with the intrachain exchange interaction J_0/k of 400 K was obtained. The spin-flop transition in the antiferromagnetic state was found and the related anisotropy field was determined to be 1.0 kOe.

We have observed the electron spin resonance in CuO powder with the purity of 99.999 %. It is noted that no resonance is found in CuO when the standard ESR spectrometer is used[26)]. The central idea of the present experiment is to use a pulse magnet for detecting a very broad resonance line. The standard field modulation method detects the differential signal of absorption so that the signal is very weak when the resonance linewidth is very broad, while the pulse field ESR can see the whole resonance profile with large field scanning. Therefore, ESR signals with width higher than one Tesla can be observed by this method.

Paramagnetic resonance at various temperatures in pulsed high magnetic field has been performed with the reflection type

rectangular cavity for a microwave of 45 GHz. The observed paramagnetic resonance line with the width of about 1.6 T at room temperature is shown in Fig. 17. The g value is estimated to be 2.0 with a slight temperature dependence, as is shown in Fig. 18, where the linewidth is also given. The linewidth decreases as temperature decreases and the broadning due to critical slowing down is found near T_N[34)]. The line shape is investigated by comparing the Gaussian and Lorentzian shapes, as was done by Dietz et al.[35)], and the result is given in Fig. 19. The line shape is between these curves, reflecting the one-dimensional character. The analysis is carried out by using the line shape in the field region above the resonance center because a small kink is seen around 1.0 T. The observed broad linewidth may be understood by the presence of the anisotropic exchange interaction[36)]. The magnitude of the anisotropic exchange interaction is usually given by $(\Delta g/g)^2 J_0$, where J_0 is the isotropic part of the main exchange interaction in CuO. The frequency representation of the linewidth under a strong exchange narrowing with the frequency ω_e is given by[37)]

$$\omega = \omega_p^2/\omega_e \qquad (2)$$

where the main part of ω_p in CuO may be due to $(\Delta g/g)^2 J_0$. J_0/k is found to be 400 K by the magnetic susceptibility, and $\Delta g/g$ is of the order 0.2, which is common value for Cu^{2+} because of usual $g_\perp = 2.0\text{-}2.2$ and $g_{/\!/} = 2.2\text{-}2.4$. Using these values, the order of the linewidth is estimated to be 0.5 T for the Cu^{2+} spin. This value is not so far from the observed half width of 0.8 T.

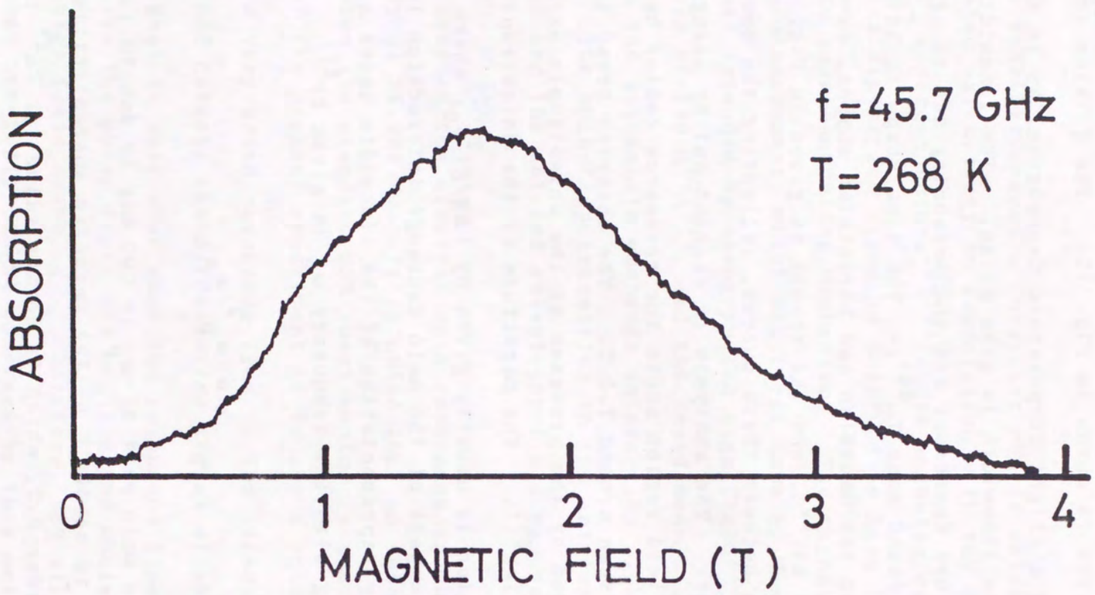

Fig. 17. Paramagnetic resonance of CuO powder at 268 K.

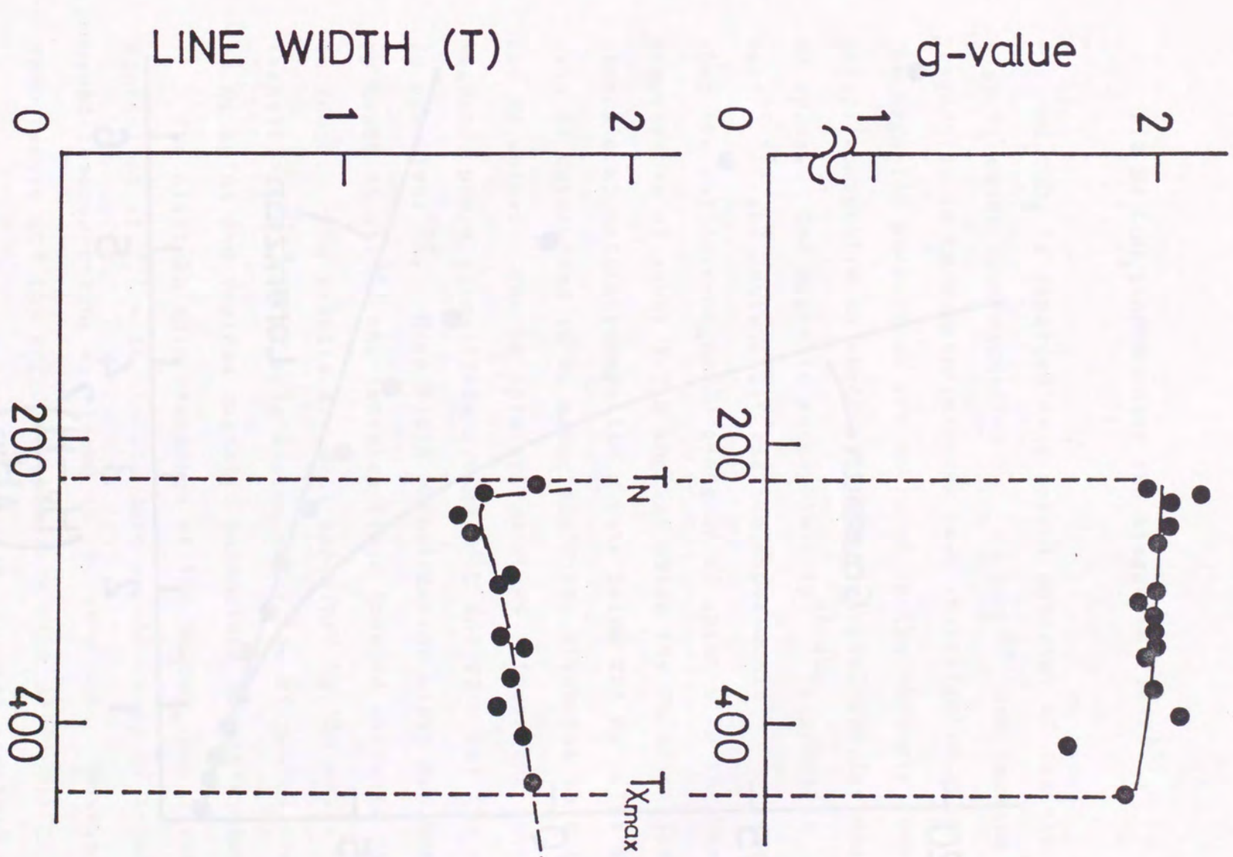

Fig. 18. Temperature dependence of g-value and linewidth in CuO.

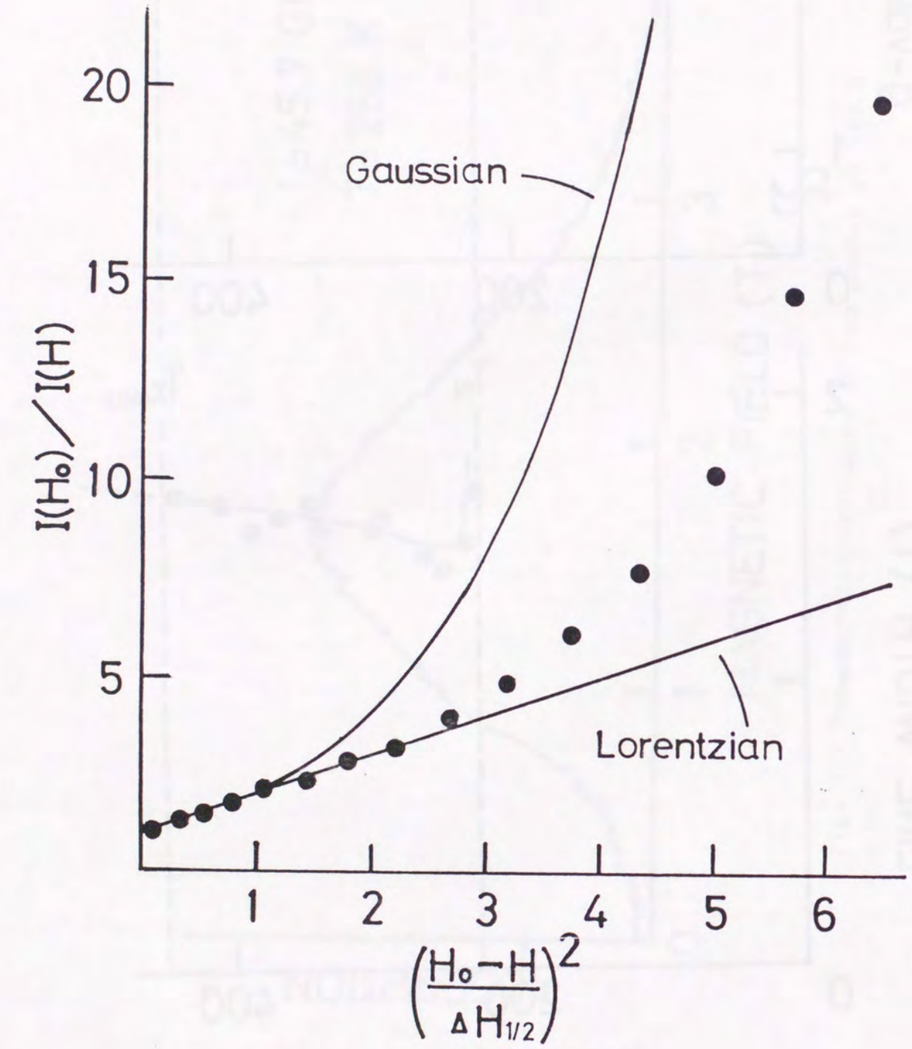

Fig. 19. Line shape of paramagnetic resonance in CuO.

3.2 Nd_2CuO_4; AFMR under the staggered field[38)]

Nd_2CuO_4 is regarded as a parent material of the electron high T_c oxide superconductor $Nd_{2-x}Ce_xCuO_4$[39)] and various electronic properties on this material have been investigated recently. The magnetic properties are sketched by the strongly coupled antiferromagnetic Cu sheet and weakly coupled antiferromagnetic Nd spins. The magnetic susceptibility[40-42)], specific heat[40,43)] and neutron diffraction experiments[44-47)] revealed that the antiferromagnetic order of Nd spins with the Neel temperature of about 1.7 K appears while the Cu spins form two-dimensional antiferromagnetic sheets below 255 K. The spin easy axis is determined to be along the [110] direction both for Cu and Nd spins. The Cu spin system shows interesting successive magnetic phase transitions around 80 K and 40 K but the mechanism is not clear[46)]. High field magnetization study has been done by Kondo et al.[48)] and two-step field induced magnetic transition is found. The results are well explained by the phase transitions of the Nd spin system under the staggered field due to Cu spins and various magnetic parameters are determined.

The electron spin resonance of the Nd_2CuO_4 was tried by Kontani et al.[49)] with the standard spectroscopy of X-band and a broad resonance line was found in the ab-plane. However, the temperature and the angular dependence were difficult to understand by the usual theory and the results remained without explanation. Recently, the experiment is extended to the millimeter microwave region with the high field ESR up to 10 T

and new resonance lines including the critical field resonance are found. The whole data are analyzed and it is found that the observed resonance are attributed to the AFMR of the Nd spin network under the molecular field acts as the staggered field on each Nd spin as if the field is regarded as an anisotropy field on the Nd spin.

The material is chemically similar to the first group of cuprate superconductor discovered by Bednorz and Muller with the formula of $La_{2-x}(Ba,Sr)_xCuO_y$. The crystal structure of Nd_2CuO_4 has the tetragonal symmetry and is schematically shown in Fig. 20. The structure is different from that of La_2CuO_4 because Cu atom has no apical oxygen atoms. The lattice constants are a=3.945 A and c=12.171 A. The spin structure is determined by the neutron diffraction and the result below T_N is illustrated in Fig. 20. The Cu spins form antiferromagnetic sheets in the Cu-O plane with ferromagnetic spin arrangement along the c-axis and two Nd spins between two Cu ions along the c-axis also point in the same direction. The Nd spin sheet in a c-plane has an antiferromagnetic arrangement. The magnetic interaction between the Cu and Nd spins are shown in the left figure (a) of Fig. 21. The hatched circle, Nd spin, is surrounded by five Cu spins. Four Cu spins in a c-plane are antiferromagnetically ordered so that no net field on the Nd spin is expected. However, the exchange field from another Cu spin is not cancelled and the field can be regarded as the staggered field because the field is antiferromagnetically distributed in the crystal. The net spin system is then sketched by a four-sublattice model in a Fig. 21

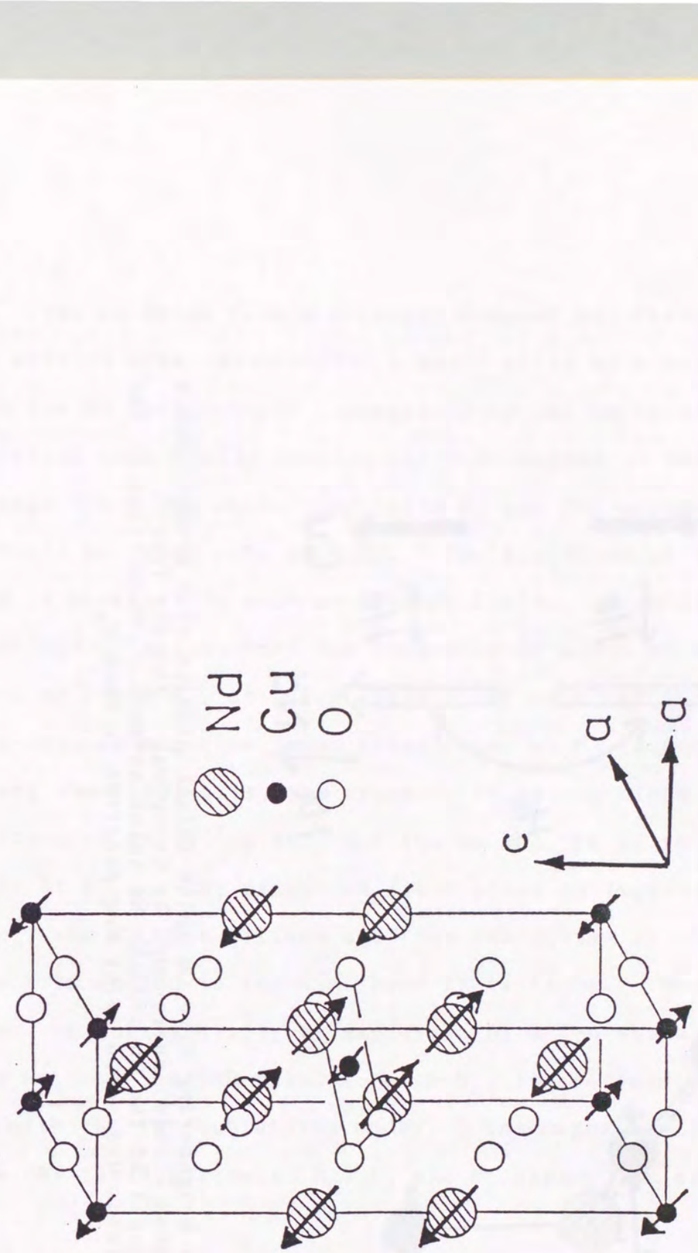

Fig. 20. Crystal and spin structures of Nd_2CuO_4. The spin easy axis is parallel to the [110] direction.

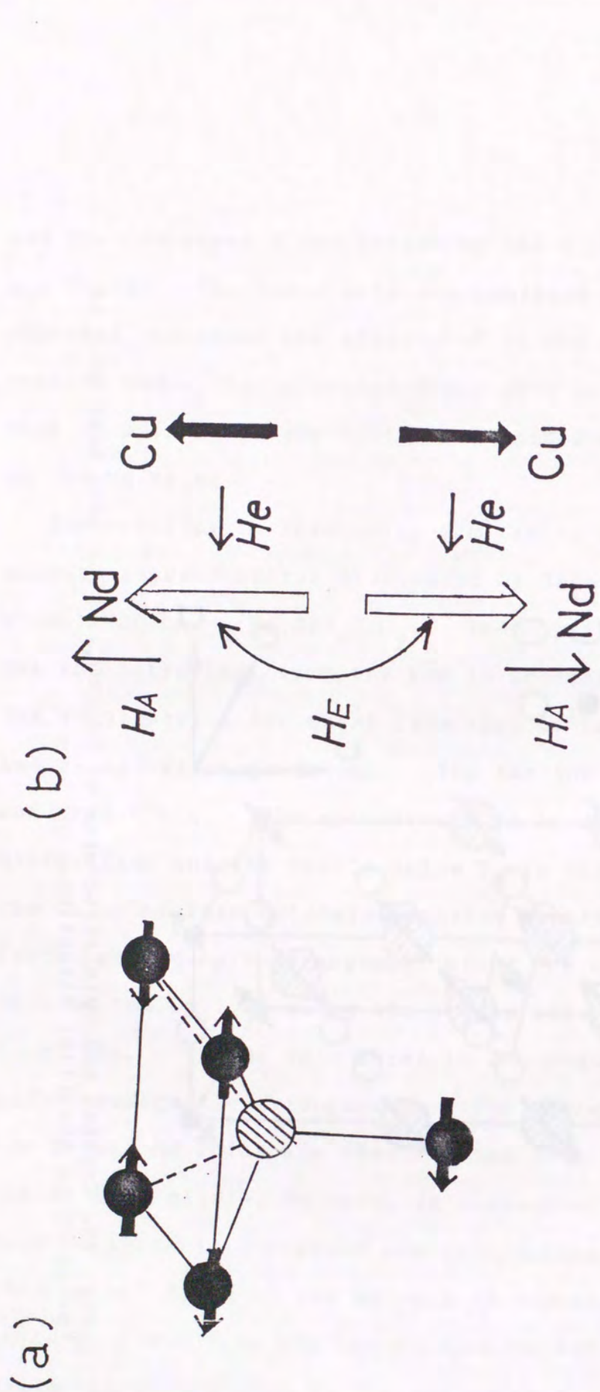

Fig. 21. (a) Neighboring five Cu spins (black circles with arrows) and a Nd ion (hatched circle) surrounded by Cu spins. (b) The four-sublattice model of the Cu and the Nd spins network. Directions of the staggered fields due to Cu spins are parallel to each H_A.

(b). The Cu spins from a strongly coupled antiferromagnetic spin network with two-sublattice model given by black arrows while the Nd spin network represented by two white arrows is understood as a weakly coupled antiferromagnet in which the main exchange field H_E, anisotropy field H_A and the staggered field H_e should be taken into account. The direction of the staggered field is parallel to each anisotropy field. High field magnetization measurement has been done by Kondo et al. and the spin-flop field H_{sf} at 0.7 T along [110] axis and two anomalous field-induced magnetic phase transitions at H_{c1}=2.5 T and H_{c2}=4.5 T along the [110] axis, are found. It is now clear that the simultaneous spin-flop both for the Cu and the Nd spin systems occurs at H_{sf}. The staggered field plays an important role for the H_{c1} and H_{c2} transitions and four-sublattice of the Nd spin network is needed to explain these transitions. However, the system can substantially be expressed by a two-sublattice model below H_{c1} and the ESR results below H_{c1} is analyzed by the Nd-AFMR with the two-sublattice model. The magnetization study gives the field parameter H_E, H_A and H_e around 1 K as

$$H_E=3.0\ \text{T},\ H_A=0.1\ \text{T},\ H_e=0.5\ \text{T}. \qquad (3)$$

Those values are compared with those obtained by the AFMR study as will be shown later.

High quality single crystals of Nd_2CuO_4 were grown by the flux method in the Nippon Telegraph and Telephone (NTT) Optoelectronics Laboratories. The sample size is 3x1x1 mm^3 with well developed (100) planes. The ESR study at 9.33 GHz is done

by using the standard ESR spectrometer of Varian E-109 under the field up to about 1 T with the field modulation of 270 Hz. The lowest temperature of the study is 1.8 K which is higher than T_N of 1.7 K. However, observed ESR data are explained by the AFMR model as will be shown later and this fact suggests that a considerable amount of the short range order exists above T_N in accord with other magnetic measurements.

The high field ESR data are shown in Fig. 22, where an external magnetic field is applied along the spin easy axis at 1.3 K. It is noted that the resonance peak near 0.8 T does not show the frequency dependence. Considering the fact that the critical field, the spin-flop field H_{sf}, is about 0.75 T at 1.3 K, the observed resonance is attributed to the critical field resonance as is seen in $CuCl_2 2H_2O$[50]. Another absorption line is separated from the critical field resonance at 30.7 GHz given by dotted resonance line with the peak near 2.2 T. The temperature and angular dependences of the resonance line at 9.33 GHz are shown in Fig. 23 by black circles. No angular dependence is seen at 10 K reflecting pure paramagnetic resonance signal at this temperature. This signal is found between 10 K and 30 K and no resonance is found above 30 K probably due to rapid spin-lattice relaxation time. The g-value is 0.85 which is not so far from the free ion value of 0.73. A noticeable angular dependence of the resonance point appears in the c-plane below 10 K and the temperature dependence of the resonance point along the spin easy axis is given in Fig. 24. Noticing the fact that T_N of Nd spin system is around 1.7 K, the observed resonance shift may be due

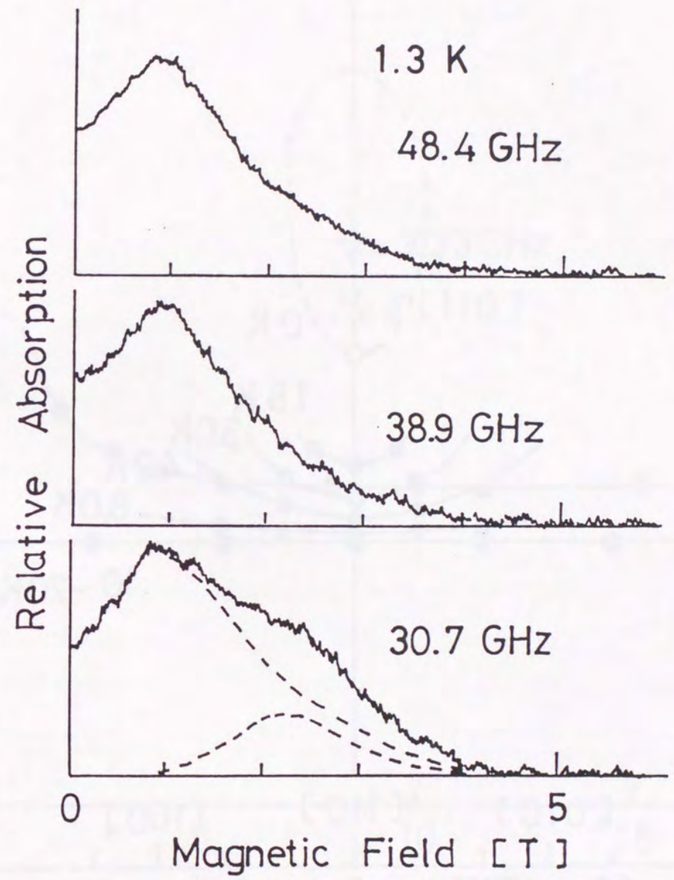

Fig. 22. High-field ESR data in Nd_2CuO_4. Two dotted lines at 30.7 GHz show the separated absorptions from the superposed line profile.

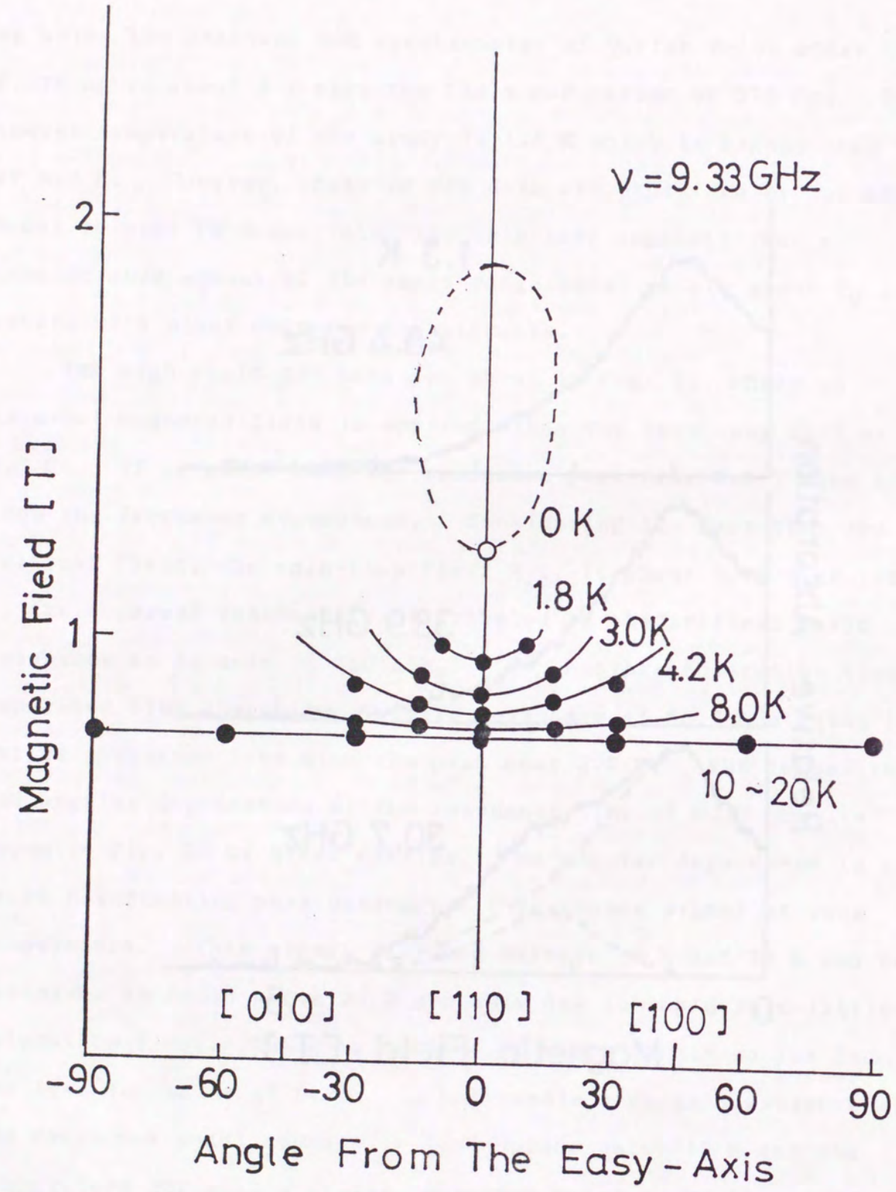

Fig. 23. Temperature and angular dependences of the resonance at 9.33 GHz in the c-plane. An elliptic curve shows a theoretical calculation at 0 K using the Nagamiya theory with the resonance parameters in the text.

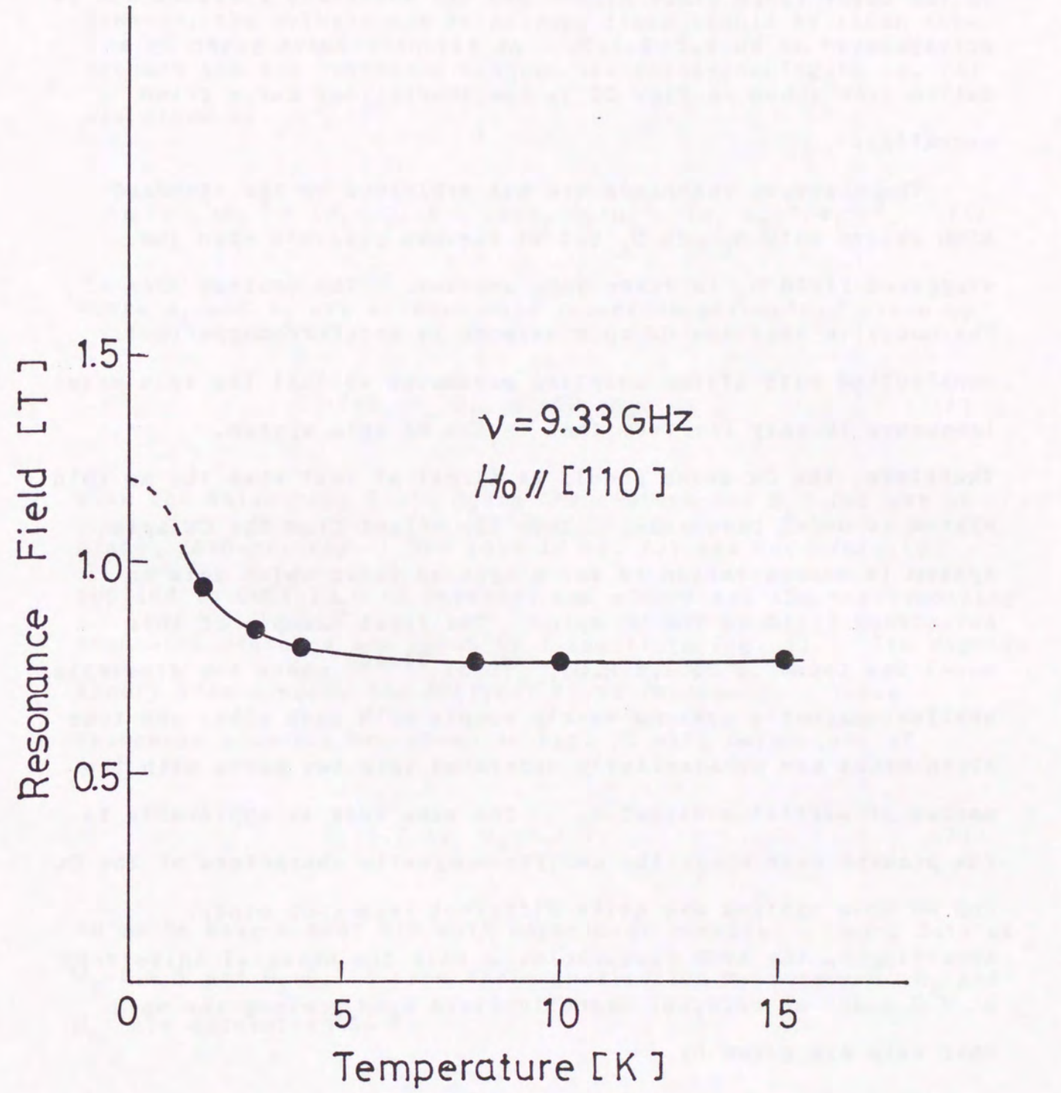

Fig. 24. Temperature dependence of the resonance field at 9.33 GHz along the spin easy axis.

to the short range order effect and the resonance field at 0 K is extrapolated to be 1.2±0.1 T. An elliptic curve given by a dotted line shown in Fig. 23 is the theoretical curve given hereafter.

The observed resonance are not explained by the standard AFMR theory with H_E and H_A but it becomes possible when the staggered field H_e is taken into account. The central idea of the model is that the Cu spin network is antiferromagnetically constructed with strong coupling parameter so that the spin wave frequency is very far from that in the Nd spin system. Therefore, the Cu spins should be almost at rest when the Nd spin system is under resonance. Then the effect from the Cu spin system is concentration to the staggered field which acts an anisotropy field on the Nd spin. The first example of this model was found in $CoCl_2 6(H_2O)_{1-x}(D_2O)_x$ [51,52] where two dissimilar antiferromagnetic systems weakly couple with each other and four eigen modes are substantially separated into two parts with the manner of partial oscillation. The same idea is applicable to the present case where the antiferromagnetic characters of the Cu and Nd spin systems are quite different from each other. Accordingly, the AFMR frequencies ω with the uniaxial anisotropy at 0 K under an external magnetic field $H_0 < H_{sf}$ along the spin easy axis are given by

$$\omega/\gamma = \{2H_E(H_A+H_e) + (H_A+H_e)^2\}^{1/2} + H_0, \qquad (4)$$

where γ is the magneto-machanical ratio. The term $(H_A+H_e)^2$ in eq. (4) is usually negligible. In the practical Nd spin system,

however, the orthrhombic anisotropy field should be taken into account and the resonance frequencies corresponding to eq. (4) are given by

$$(\omega/\gamma)^2 = H_0^2 + (c_1+c_2)/2 + \{2(c_1+c_2)H_0^2 + (c_1-c_2)^2/4\}^{1/2}, \qquad (5)$$

where c_1 and c_2 are orthorhombic resonance parameters given by

$$C_1 = 2(H_A+H_e)H_E, \quad c_2 = 2H_A'H_E, \qquad (6)$$

with the anisotropy field H_A in the c-plane and H_A' for out of plane, respectively. The formula eq. (5) was successfully applied to $CuCl_2 2H_2O$ by Nagamiya and others and the corresponding resonance branches are shown by I and II in Fig. 25. The Nagmiya theory also expects the critical field resonance. These resonance branches are shown in Fig. 25 with parameters of

$$C_1 = 1.7 \text{ T}, \quad C_2 = 3.3 \text{ T}, \qquad (7)$$

so as to have a best fit with experiment results. Using data of $H_E = 3.0$ T and $H_A = 0.1$ T from the magnetization measurement, H_e and H_A' are determined as

$$H_e = 0.4 \text{ T}, \quad H_A' = 1.8 \text{ T}. \qquad (8)$$

An important difference from the Nagamiya theory is that the critical field resonance is not observed on the dotted line AB in

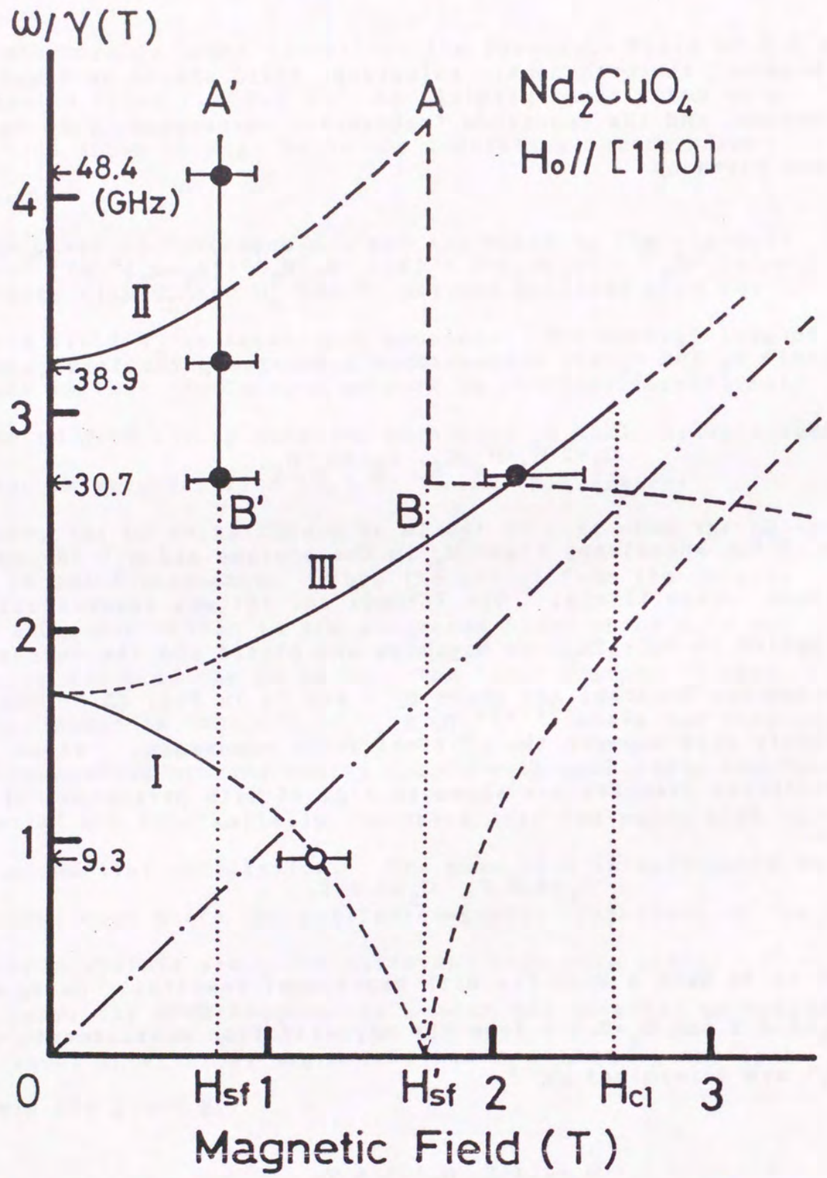

Fig. 25. Frequency-field diagram of the AFMR in Nd_2CuO_4. Three branches I, II and III are shown. Full lines are observable and broken lines are not observable. A bar-dot line is the paramagnetic resonance line. The closed circles represent the observed resonances and an open circle is an extrapolated resonance point with the resonance parameters given in the text.

Fig. 25 but is found at the spin-flop field H_{sf} of 0.8 T given by the A'B' line. This is quite natural because the true spin-flop appears at H_{sf} and H_{sf}' is the virtual spin flop field in the resonance theory. A resonance point at 2.2 T on the branch III comes from the spin configuration where the Nd and Cu spins undergo the spin-flop field transition and the Nd spins have their substantial spin easy axis perpendicular to the magnetic field. The resonance condition is given by

$$(\omega/\gamma)^2=C_1+H_0^2. \tag{9}$$

It is noted that the branch III is seen only in between H_{sf} and H_{c1} because the spin configuration corresponding to the branch III is only stable between these two fields. The resonance point at 9.33 GHz region shown by an open circle is the extrapolated point to 0 K and the calculated resonance ellipse is shown in Fig. 23.

Thus the experimental results are well explained by the antiferromagnetic resonance model with the staggered field from the Cu spin. The estimated staggered field is 0.4 T which is not so far from the value of 0.5 T determined by the high field magnetization study.

3.3 Mn^{2+} in $CsCoCl_3$: impurity spin resonance in an antiferromgnet

A typical impurity spin resonance in high field has been reported in Mn-doped $CoCl_2 2H_2O$[22], where the exchange interaction between Co and Mn spins gives an additional field to the resonance condition. Impurity resonance in $CsCoCl_3$ has been done as an example of microwave high-field ESR and various kinds of Mn-impurity resonances are found. $CsCoCl_3$[53] is one of hexagonal ABX_3 type compounds and is known to be a good example of a quasi one-dimensional Ising-like antiferromagnet. The magnetic Co^{2+} ions lie in the chains parallel to the c-axis as shown in Fig. 26. The high field magnetization measurement has been done extensively by Hori et al.[54], and the intrachain exchange J_0 of -54 cm^{-1} and the interchain exchange J_1 of -5.8 cm^{-1} are obtained. Kikuchi and Ajiro[55] observed one absorption line with g=2.0 and it is attributed to the resonance coming from an excited state where the net effective field is cancelled.

High-field ESR has been carried out at liquid helium temperature up to 15 T. Typical results at the frequency of 48.2 GHz are shown in Fig. 27, where many resonance lines are seen. The frequency dependence of these lines are investigated and the results are shown in Fig. 28. As Mn ion has spin S=5/2, five fine structure lines are expected when the uniaxial anisotropy DS_z^2 term exists in the spin hamiltonian, as is in $CoCl_2 2H_2O$. However, the experimental results show that not only S=5/2 line but also S=7/2 and 9/2 lines are observed. Moreover, two sets for S=7/2 and 9/2 lines are found whereas only one set for the S=5/2 lines is observed in the low field region. The

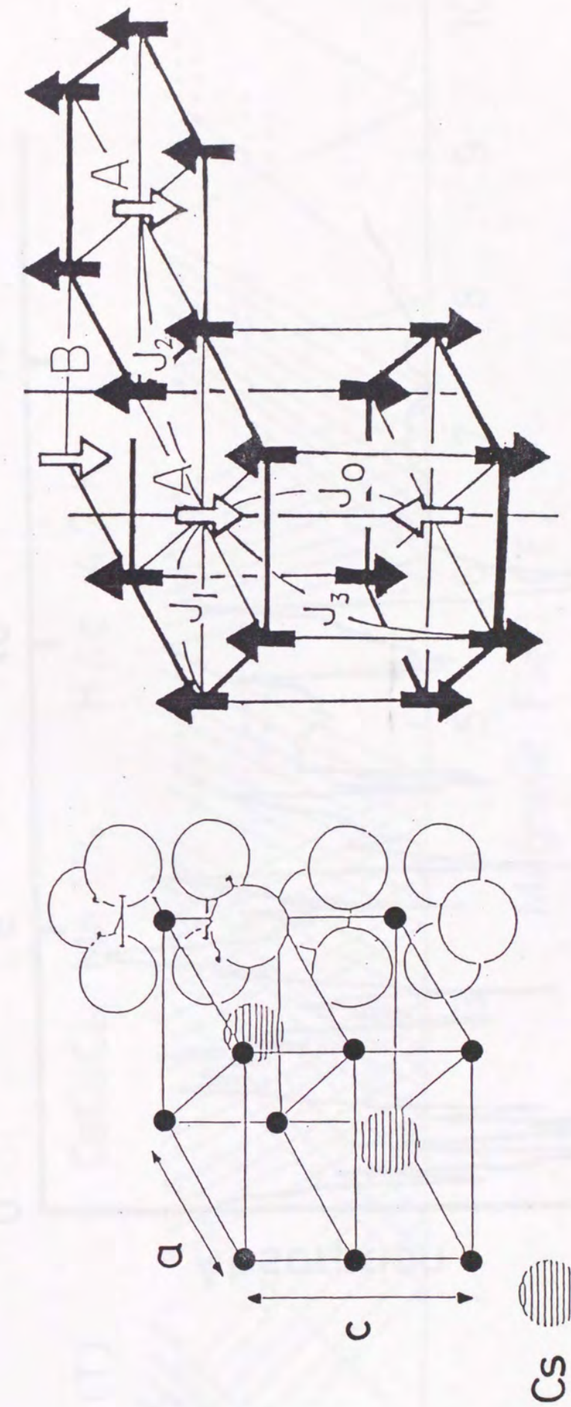

Fig. 26. Crystal and spin structures of $CsCoCl_3$. $CsCoCl_3$ has two magnetic cobalt sites. Interchain exchange fields on the B-site are cancelled.

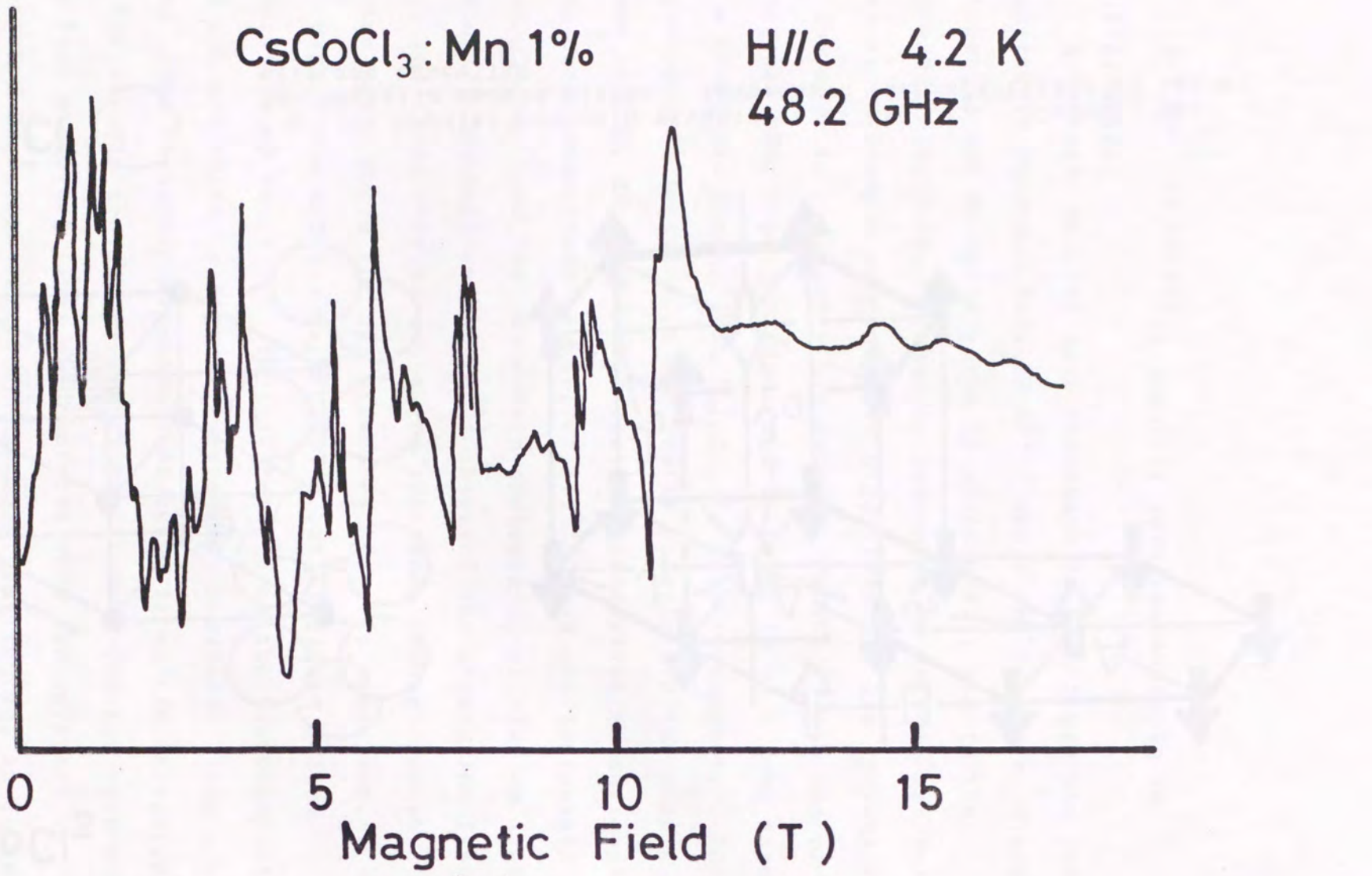

Fig. 27. High field ESR data of Mn^{2+} impurity in $CsCoCl_3$. Magnetic field is applied along c-axis.

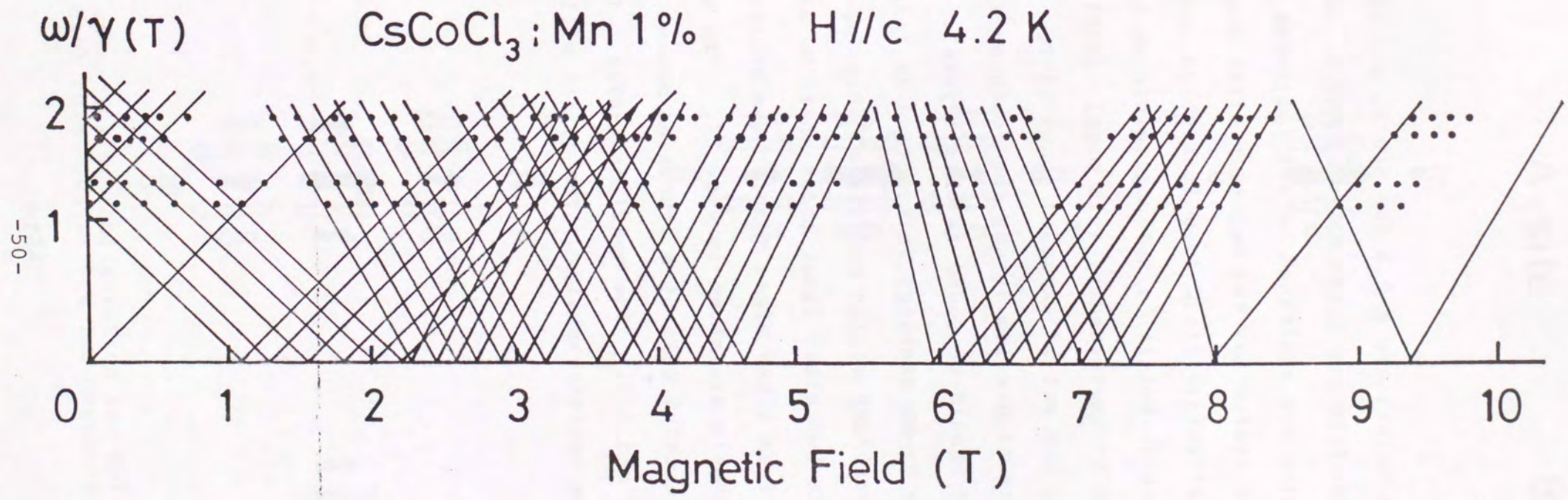

Fig. 28. Frequency-field diagram of Mn^{2+} impurity resonance in $CsCoCl_3$.

corresponding g-values are g=2.0 for S=5/2, g=3.46 and 3.79 for S=7/2 and g=8.18~4.50 and 2.54~3.40 for S=9/2, respectively.

These results are explained in the following way. As shown in Fig. 26, this system has two magnetic sites denoted by A- and B-sites. The effective field from interchain interactions does not affect on B-site but it is not negligible on A-site. The observed two-set is explained by this model except the case of S=5/2. Another 5/2 set is expected above 10 T. An important point of the present problem is why the resonances with net spins of S=7/2 and 9/2 should be found in this crystal. The central idea is that the Co-Mn exchange interaction is fairly large so that a simple localized motion associated only impurity spin is not a unique mode but other local modes where Mn and a few Co spins couple to form a new eigen mode. The analyzed spin set related to new models are shown in Fig. 29. The set of black spin form a new quantum unit of a truncated moment with the net spin of 5/2, 7/2 and 9/2. The model can explain the experimental data satisfactorily. The detail will be shown in other papers[56].

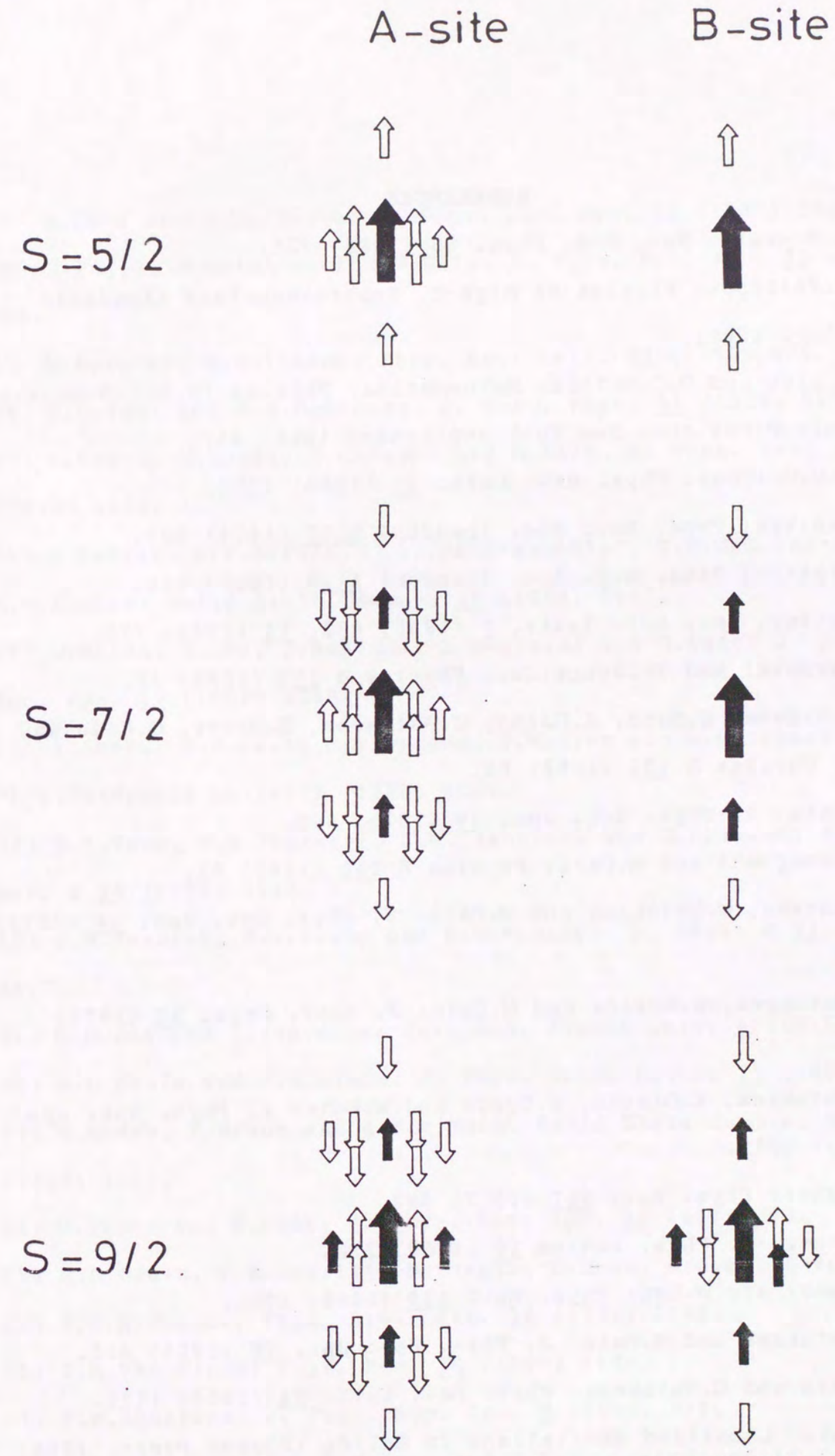

Fig. 29. Locked spin-cluster configuration for S=5/2, 7/2 and 9/2, respectively. Each spin-cluster has two magnetic sites.

REFERENCES

1) G.R.Stewart: Rev. Mod. Phys. 56 (1984) 755.

2) J.C.Philipps: Physics of High-T_c Superconductors (Academic Press Inc. 1989).

3) E.H.Lieb and D.C.Mattis: Mathematical Physics in One Dimension (Academic Press Inc. New York and London 1966) 457.

4) F.D.M.Haldane: Phys. Rev. Lett. 50 (1983) 1153.

5) P.Kapitza: Proc. Roy. Soc. (London) A105 (1924) 691.

6) P.Kapitza: Proc. Roy. Soc. (London) A115 (1927) 658.

7) F.Bitter: Rev. Sci. Instr. 7 (1936) 482, 10 (1939) 373.

8) P.Turowski and Th.Schneider: Physica B 155 (1989) 87.

9) Y.Nakagawa, K.Noto, A.Hoshi, K.Watanabe, S.Miura, G.Kido and Y.Muto: Physica B 155 (1989) 69.

10) M.Date: J. Phys. Soc. Jpn. 39 (1975) 892.

11) A.Yamagishi and M.Date: Physica B 155 (1989) 91.

12) S.Kuroda, M.Motokawa and M.Date: J. Phys. Soc. Jpn. 44 (1978) 1797.

13) M.Motokawa, S.Kuroda and M.Date: J. Appl. Phys. 50 (1979) 7762.

14) M.Motokawa, A.Otsuka, C.Uyeda and M.Date: J. Phys. Soc. Jpn. 53 (1984) 1857.

15) S.Foner: Phys. Rev. 107 (1957) 683.

16) S.Foner: J. Phys. radium 20 (1959) 336.

17) S.Foner and W.Low: Phys. Rev. 120 (1960) 1585.

18) M.Motokawa and M.Date: J. Phys. Soc. Jpn. 20 (1965) 465.

19) M.Date and M.Motokawa: Phys. Rev. Lett. 24 (1966) 1111.

20) M.Date: Localized Excitations in Solids (Plenum Press, 1968)

358.

21) M.Date and M.Motokawa: J. Phys. Soc. Jpn. 22 (1967) 165.

22) N.Fujii, M.Motokawa and M.Date: J. Phys. Soc. Jpn. 25 (1968) 700.

23) M.Date and M.Motokawa: Phys. Rev. Lett. 22 (1965) 854.

24) S.C.Tasi and G.W.Robinson: J. Chem. Phys. 51 (1969) 3559.

25) K.Kindo, M.Honda, T.Kohashi and M.Date: J. Phys. Soc. Jpn. 59 (1990) 2332.

26) F.Mehran, S.E.Barnes, G.V.Chandrashekhar, T.R.McGuire and M.W.Shafer: Solid State Commun. 67 (1988) 1187.

27) O.Kondo, M.Ono, E.Sugiura, K.Sugiyama and M.Date: J. Phys. Soc. Jpn. 57 (1988) 3293.

28) A.Junod, D.Eckert, G.Triscone, J.Muller and W.Reichardt: J. Phys:Condensed Matter 1 (1989) 8021.

29) B.X.Yang, T.R.Thurston, J.M.Tranquada and G.Shirane: Phys. Rev. B 39 (1989) 4343.

30) J.B.Forsyth, P.J.Brown and B.M.Wanklyn: J. Phys. C 21 (1988) 2917.

31) K.Honda and T.Ishiwara: Sci. Rep. Tohoku Univ. 4 (1915) 215.

32) M.O'Keefe and F.S.Stone: J. Phys. Chem. Solids 23 (1962) 261.

33) B.Roden, E.Braun and A.Freimuth: Solid State Commun. 64 (1987) 1051.

34) M.Ikebe and M.Date: J. Phys. Soc. Jpn. 30 (1971) 93.

35) R.E.Dietz, F.R.Merritt, R.Dingle, D.Hone, B.G.Shilbernagel and P.M.Richards: Phys. Rev. Lett. 26 (1971) 1186.

36) J.H.Van Vleck: Phys. Rev. 74 (1948) 1168.

37) P.W.Anderson: J. Phys. Soc. Jpn. 9 (1954) 316.

38) K.Kindo, Y.Chiba, Y.Hidaka and M.Date: submitted to J. Phys.

Soc. Jpn.

39) Y.Tokura, H.Takagi and S. Uchida: Nature (London) 337 (1989) 345.

40) M.F.Hundley, J.D.Thompson, S.W.Cheong, Z.Fisk and S.B.Oseroff: Physica C158 (1989) 102.

41) C.L.Seaman, N.Y.Ayoub, T.Bjørnholm, E.A.Early, S.Ghamaty, B.W.Lee, J.T.Markert, J.J.Neumeier, P.K.tsai and M.B.Maple: Physica C159 (1989) 391.

42) R.Saezpuch, M.Norton, T.R.White and W.S.Glaunsinger: J. Solid State Chem. 50 (1983) 281.

43) J.T.Markert, E.A.Early, T.Bjørnholm, S.Ghamaty, B.W.Lee, J.J.Neumeier, R.D.Price, C.L.Seaman and M.B.Maple: Physica C158 (1989) 178.

44) Y.Endo, M.Matsuda, K.Yamada, K.Kakurai, G.Shirane and R.J.Birgeneau: Phys. Rev. B40 (1989) 7023.

45) J.W.Lynn, I.W.Smarlin, S.Skanthakmar, W.H.Li, R.N.Skelton, J.L.Peng, Z.Fisk and S-W.Cheong: Phys. Rev. B41 (1990) 2569.

46) J.Akimitsu, H.Sawa, T.Kobayashi, H.Fujiki and Y.Yamada: J. Phys. Soc. Jpn. 58 (1989) 2646.

47) M.Matsuda, K.Yamada, K.Kakurai, H.Kadawaki, T.R.Thurston, Y.Endo, Y.Hidaka, R.J.Birgeneau, P.M.Gehring, A.H.Moudden and G.Shirane: to be published in Phys. Rev. B

48) O.Kondo, M.Ono, T.Yosida, N.Kontani, Y.Chiba, K.Sugiyama, A.Yamagishi, M.Hikita, Y.Hidaka and M.Date: J. Magn. & Magn. Mater. 90-91 (1990) 79.

49) N.Kontani, Y.Chiba, K.Sugiyama, Y.Hidaka and M.Date: J. Phys. Soc. Jpn. 59 (1990) 3019.

50) T.Nagamiya, K.Yosida and R.Kubo: Advances in Phys. 13 (1955) 1.

51) M.Date, A.Nakanishi and K.Oshima: Int. Conf. on Magn. IV Moscow (1973) 98.

52) A.Nakanishi, M.Motokawa and M.Date: J. Phys. Soc. Jpn. 60 (1991) 2080.

53) N.Achiwa: J. Phys. Soc. Jpn. 27 (1969) 561.

54) H.Hori, K.Amaya, J.Nakahara, I.Shiozaki, M.Ishizuka, Y.Ajiro, T.Sakakibara and M.Date: J. de Phys. 49 (1988) 1455.

55) H.Kikuchi and Y.Ajiro: J. Phys. Soc. Jpn. 58 (1989) 2531.

56) K.Kindo, H.Kikuchi, Y.Ajiro and M.Date: to be published in J. Phys. Soc. Jpn.

PART II

HIGH-FIELD ESR IN THE HALDANE MATERIALS

ABSTRACT

High magnetic field electron spin resonance (ESR)in the Haldane materials NENP: $Ni(C_2H_8N_2)_2NO_2(ClO_4)$ and NINO: $Ni(C_3H_{10}N_2)_2NO_2(ClO_4)$ has been done up to 10 T in the microwave range of 30~50 GHz. A paramagnetic resonance line with strong exchange narrowing is found at high temperatures and a new resonance line with the width of about 1 Tesla is observed below 30 K. The resonance is quite different from normal paramagnetic or antiferromagnetic resonances of the ground state. The resonance line intensity decreases with decreasing temperature and it is attributed to the excited state resonance with the Haldane energy gap E_G above the ground state. The angular dependence of the excited state can be sketched by a truncated spin hamiltonian with S=1. The effective anisotropy parameters D and E for the excited states are determined to be -7.5, -0.67 cm^{-1} for NENP and -11.5, 1.05 cm^{-1} for NINO, respectively. The observed negative sign of D in the excited state has important meaning because the Ni^{2+} spin in the chain has the positive D value with nearly same magnitude and the same sign in D is expected if the excitation is described by usual spin waves. The discrepancy is well explained by introducing a localized two-spin bound state model for the soliton-like excitation. The energy gap E_G was found to be 9.5 cm^{-1} for both materials.

1. Introduction

One-dimensional antiferromagnetic chains show various quantum effects in magnetic field. A quantum spin chain with S=1/2 has been studied extensively both theoretically and experimentally. The eigen state energy is obtained exactly by Bethe[1], and the spin wave energy spectrum is calculated by Bonner and Fisher[2]. The systems had been believed to be no enrgy gap above the ground state irrespective of the spin value. In 1983, however, Haldane[3] conjectured that the linear chain Heisenberg antiferromagnet with integer spin has an energy gap above the singlet ground state and it has been called the Haldane conjecture.

Much theoretical work[4)-10)] about his conjecture has been reported including computer simulations with finite spin chain and most of the theoretical work supports the conjecture. The corresponding experimental work to verify the Haldane gap has been done for various materials. $CsNiCl_3$ had been considered as one of the candidates[11),12)] but the crystal has the Néel temperature at 4.9 K, reflecting the presence of interchain interactions, so that it is not a good candidate. Renard et al.[13)] have done magnetic and neutron diffraction experiments on NENP: $Ni(C_2H_8N_2)_2NO_2(ClO_4)$ and NINO: $Ni(C_3H_{10}N_2)_2NO_2(ClO_4)$, and concluded that these are better materials for testing the gap. The high-temperature magnetic susceptibilities are well under tood by the antiferromagnetic linear-chain model but exponential decreasing in the susceptibility is found at low

temperatures. This is not explained by the Bonner-Fisher theory but the result is well understood by the presence of the energy gap. No long-range order is found down to 0.5 K, reflecting negligible interchain interactions. Neutron diffraction measurement in NENP shows the existence of anisotropic energy gap and the magnetic field dependence of the spin wave band above E_G is found.

A high-field magnetization study up to 50 T(Tesla) is done by Katsumata et al.[14], and field-induced quenching of the gap is found. No magnetization is found at low field reflecting the gap but a linear magnetization appears above the critical field H_T which is angular dependent. Similar magnetization data were obtained by Ajiro et al.[15]. Katsumata et al. proposed the following model[14] to explain the magnetization profile. They put the triplet excited state just below the excited spin wave continuum as is expected by Haldane. The triplet splits under magnetic field and low-lying level crosses with the ground state at H_T. Then, the Haldane gap is quenched and usual antiferromagnetic state appears. The observed anisotropy in H_T is explained by the effective anisotropy in the triplet. Accordingly, the electron spin resonance in the triplet may be expected if the Katsumata model is correct.

Experimentally speaking, the standard ESR spectrometer with 10 GHz may not be enough to cover whole profile of the triplet because the gap energy is of the order of 10 cm^{-1}. Considering the fact, high field ESR is tried to see the Haldane ESR. It is noted that the impurity doped ESR comes to the standard ESR regimes and Cu-doped NENP is studied by Hagiwara et al.[16].

A brief survey of the crystal structure is given in the next section and the magnetic properties in NENP and NINO are summarized in the section 3. The experimental procedure is described in the section 4 and the obtained results are summarized in the section 5. The analysis and discussions are shown in the section 6 and a general feature of the excited state is sketched by introducing a localized two-spin bound state model.

2. Crystal structure

NENP and NINO have similar crystallographic structures with orthorhombic symmetry as schematically shown in Fig. 1. NENP[17] has a space group of the $Pn2_1a$ or Pnma, and NINO belongs to the $Pbn2_1$ space group. The lattice constants are determined to be a=15.223, b=10.300 and c=8.295 A for NENP, a=15.384, b=10.590 and c=8.507 A for NINO. In both compounds, the nickel ions are located one-dimensionally along the b-axis and the chains of nickel ions are well separated from each other by the perchlorate anions. The nickel ions are linked by the NO_2 group along the b-axis with covalent bond and each nickel ion is surrounded by four nitrogen atoms belonging to two diamine molecules. The Ni-4N plane is nearly perpendicular to the b-axis. Therefore, the nickel ion is regarded at the center of a distorted nitrogen octahedron. Only a difference between these two compounds is seen in the bridge of ligand molecules.

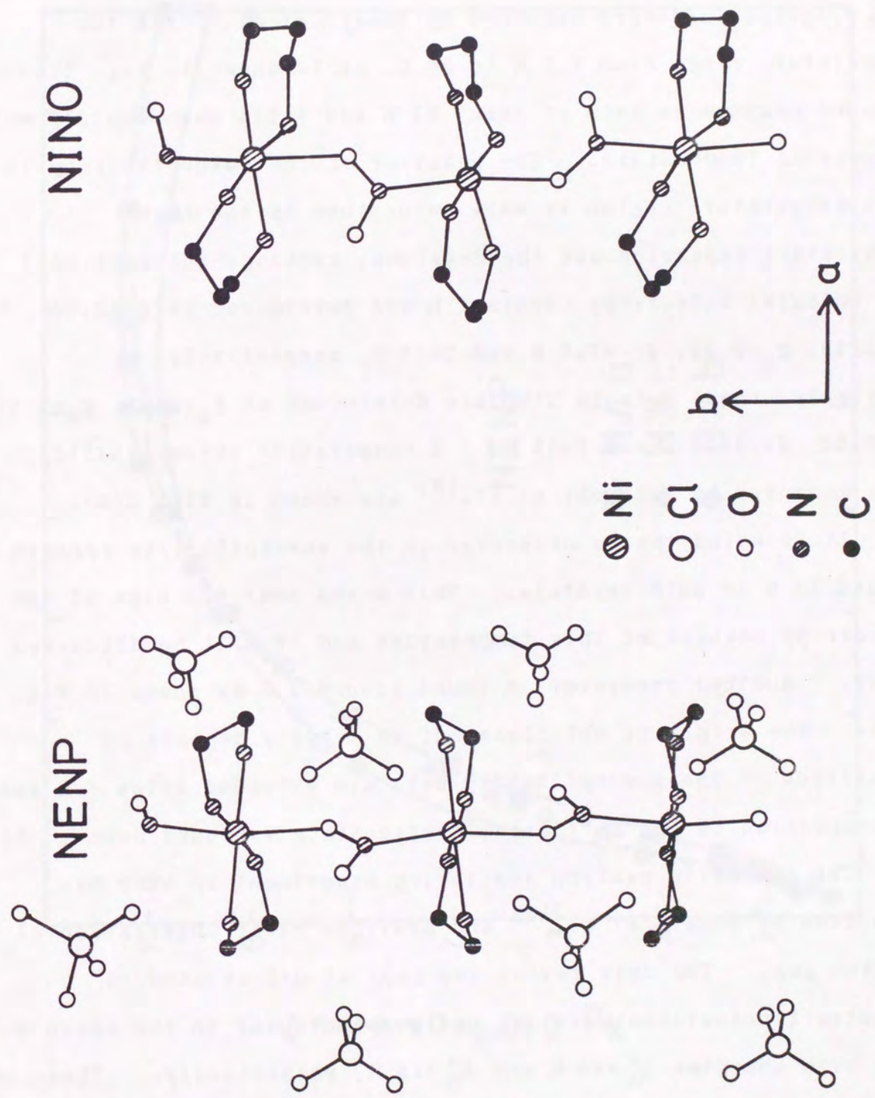

Fig. 1. Schematic view of crystal structure of NENP and NINO.

3. Magnetic Properties

The magnetic susceptibilities of NENP single crystals along the principal axes are obtained by Renard et al.[13] in the temperature range from 1.7 K to 90 K, as is shown in Fig. 2(A). A round maximum is seen at about 60 K and falls down rapidly with decreasing temperature. The behavior of the susceptibility in high temperature region is well understood by the high temperature expansion and the g-values, exchange interaction J and uniaxial anisotropy constant D are determined as g_a=2.23, g_b=2.15, g_c=2.21, J=-47.5 K and D=12 K, respectively. Similarly, these data in NINO are determined as g_a=2.23, g_b=2.17, g_c=2.22, J=-49.9 K and D=18 K. A comparative susceptibility data measured by Takeuchi et al.[18] are shown in Fig. 2(B).

It is noted that a crossover in the susceptibility appears around 35 K in both crystals. This means that the sign of the anisotropy changes at this temperature and it will be discussed later. Another crossover is found around 3 K as shown in Fig. 2(A). The origin is not clear but it largely depends on impurities. The susceptibility data are extended below 1 K and no transition to the antiferromagnetic state is found down to 30 mK.

The inelastic neutron scattering experiment on NENP has been done by Renard et al.[13] and provides clear observation of Haldane gap. The data reveal two gaps at q=1 related to magnetic fluctuations parallel and perpendicular to the chain b-axis with energies $E_G^{//}$=30 K and $E_G^{\perp}$=14 K, respectively. These two gaps result from the splittings of the Haldane gap of the pure

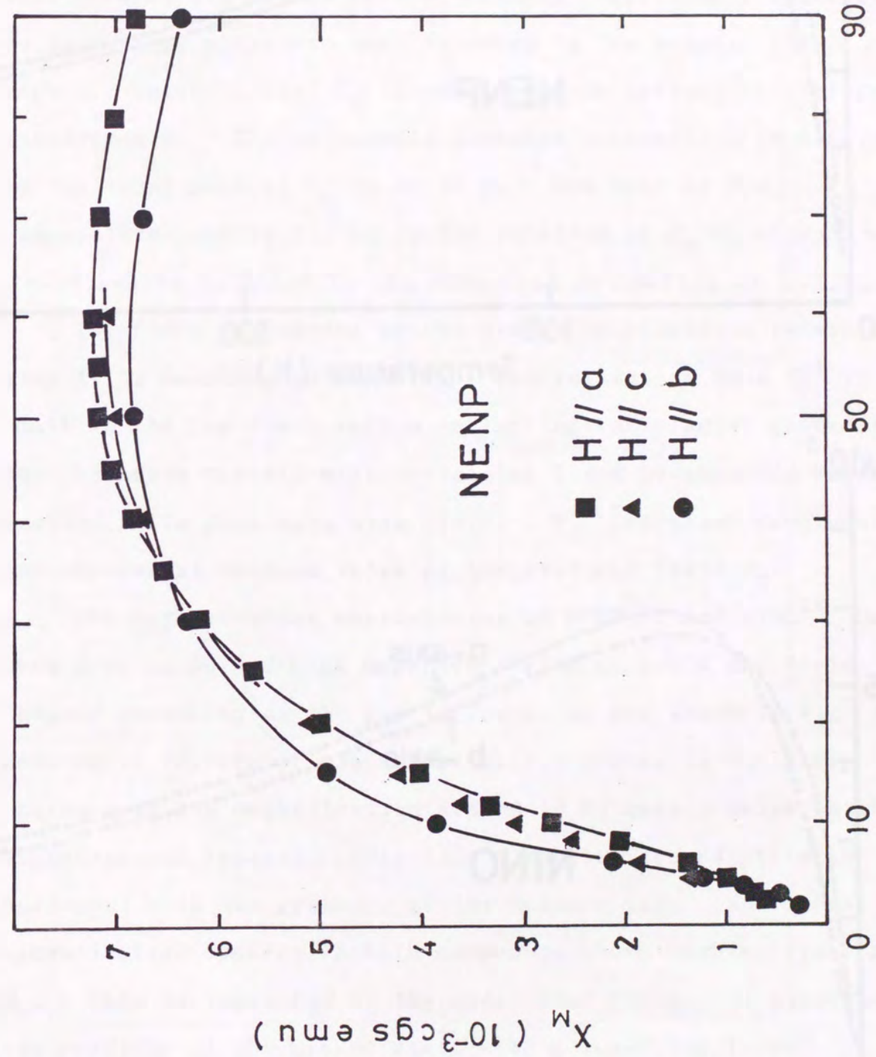

Fig. 2. (A) Magnetic susceptibility in NENP below 90 K. Crossover of anisotropy is found around 35 K.

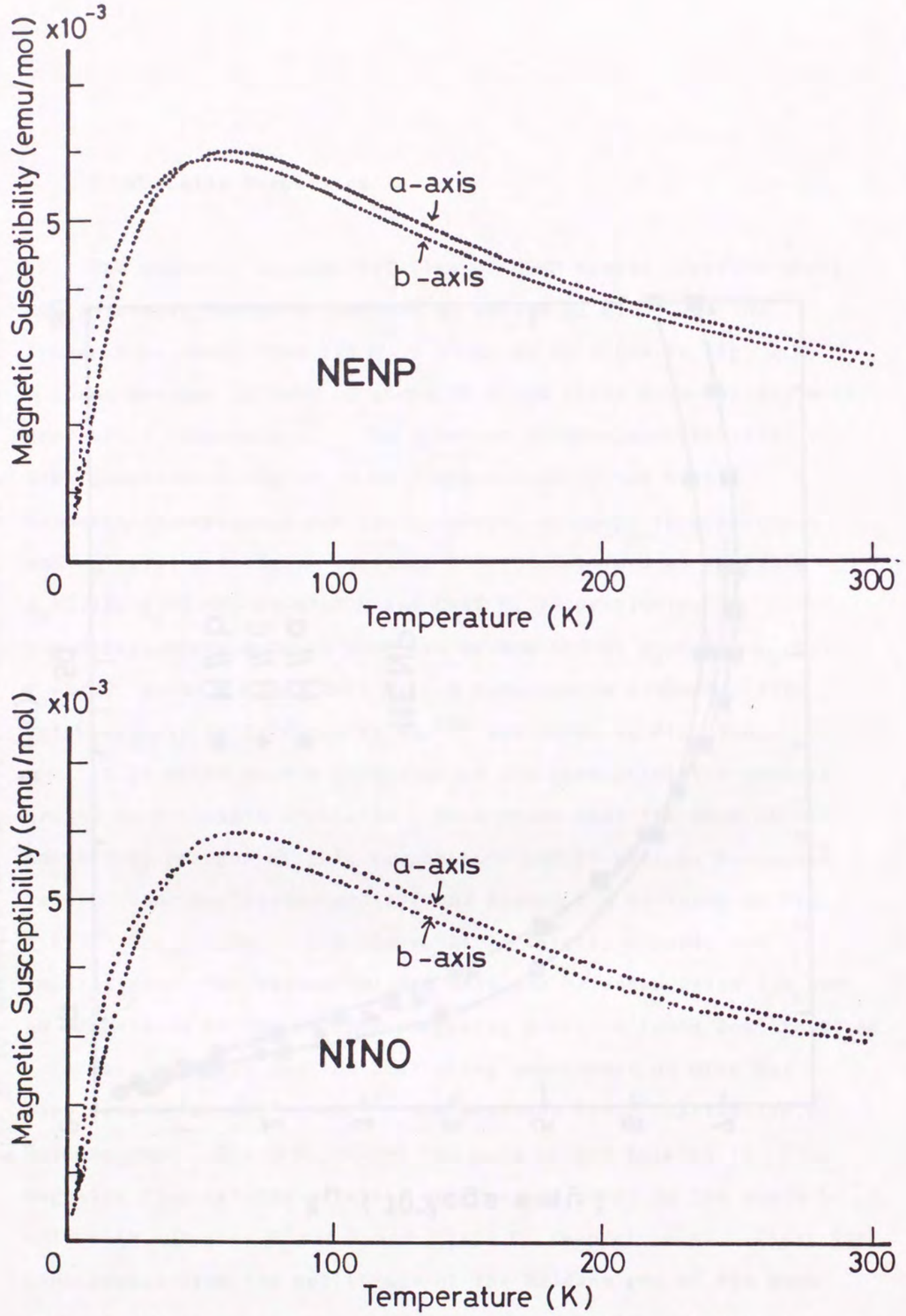

Fig. 2. (B) Comparative susceptibilities in NENP and NINO from room temperature down to 1.7 K.

Heisenberg chain by the single ion anisotropy D. The D-value is obtained to be 10 K.

Standard specific heat measurements[19] have been performed in NENP between 1.2 and 20 K. No anomaly indicating a transition to long range order has been detected in the range. The magnetic specific heat C_m is obtained from optical birefringence measurements. The intrachain exchange interaction is determined by the round peak of C_m to be 50 K. The data at low temperatures can be fitted by the relation of $C_m=C_0(kT/J)^{\alpha}$ with $\alpha=1.4$, which is close to the numerical estimation of $\alpha=1.6$.

The field dependence of the proton spin-lattice relaxation time T_1 is measured in NENP[20]. The relaxation rate T_1^{-1} is quite small in the low field region reflecting the singlet ground state but increases rapidly with increasing field because the magnetic excited state goes down with field. T_1^{-1} increases monotonously and reaches at maximum value at the critical field H_T.

The magnetization measurements on NENP[14] and NINO[18] have been done in pulsed high magnetic fields at 1.3 K and field-induced quenching of the gap is found, as are shown in Fig. 3. Remarkable feature of the magnetization curves is the sharp increase in the magnetization around 10 T(Tesla), below which no magnetization appears, reflecting a singlet ground state in agreement with the presence of the Haldane gap. The linear magnetization appears in both compounds above each critical field H_T. This is explained by the model that the gap is quenched by the crossing of the ground state with a low-lying level. The possible origin of the anisotropy in H_T is suggested by Katsumata et al.[14]. They assumed a triplet excited state at the bottom

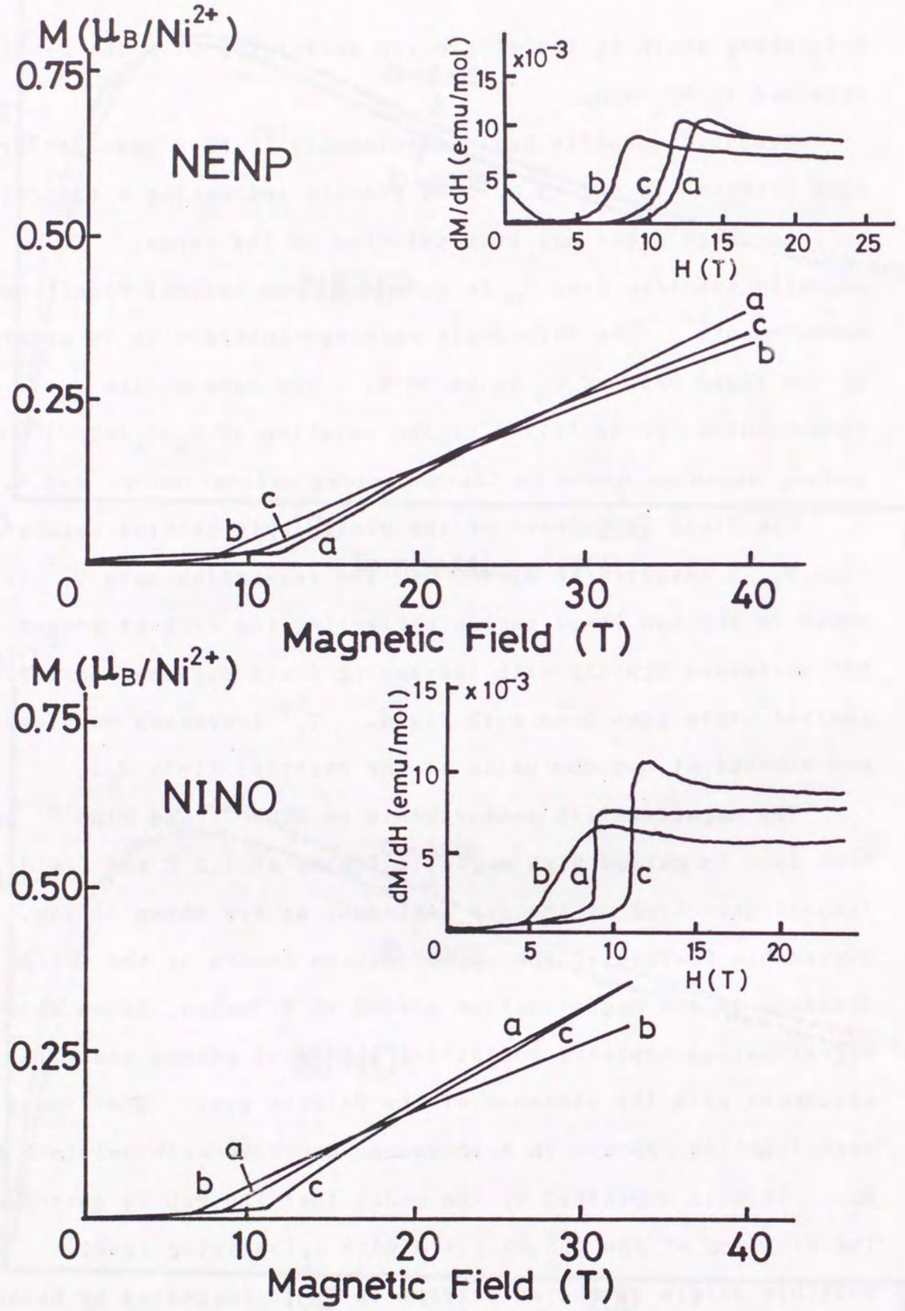

Fig. 3. Comparative magnetization curves in NENP and NINO.

of the spin wave continuum. The triplet has three sublevels and an effective uniaxial anisotropy constant splits into a singlet and a doublet. Assuming a negative sign for D in the excited triplet, a low-lying level energy E is expressed for the field along the b-axis as

$$E=E_G-D/3-g_b\mu_B H'', \tag{1}$$

where E_G is the Haldane gap energy in zero external field and H'' means the field along the b-axis. Then, the crossover occurs at the field given by

$$H_T''=(E_G-D/3)/g_b\mu_B. \tag{2}$$

When H is directed perpendicular to the b-axis, the field-dependent gap energy is expressed as

$$E=E_G+D/6-(D^2+4g_\perp^2\mu_B^2H^2)^{1/2}/2. \tag{3}$$

The transition field perpendicular to the b-axis $H_T^\perp$ is then given by

$$H_T^\perp=(E_G^2+E_GD/3-2D^2/9)^{1/2}/g_\perp\mu_B, \tag{4}$$

where small orthorhombic anisotropy is neglected. Putting the experimental values for H_T and g into eqs. (2) and (4), the values 17 K for E_G and -16 K for D are obtained. The value of E_G

is close to that of $E_G^{\perp}$ estimated from the susceptibility data, while the D value is negative and it is quite different from that of each Ni^{2+} spins of D=12 K.

Thus, high field magnetization results are well explained by introducing the anisotropic energy in the excited triplet with a negative D value. However, the origin of the negative D-value for the excited state has been a mystery in NENP. One of the motivation of the present work was to solve the mystery by observing the direct transition in the excited triplet.

4. ESR experimental procedure

4.1 Preparation of the specimen

The specimens used in this experiment were grown by means of slow evaporation from the aqueous solution with equimolars of $Ni(ClO_4)_2 6H_2O$, ethanediamine and $NaNO_2$ for NENP and propanediamine instead of ethanediamine for NINO. The crystal of NENP has cleavage along the ab-plane and it is the bc-plane for NINO. Typical crystal forms are shown in Fig. 4. Care should be paid to the crystal directions because well developed direction in NENP is the b-axis while it is the c-axis in NINO.

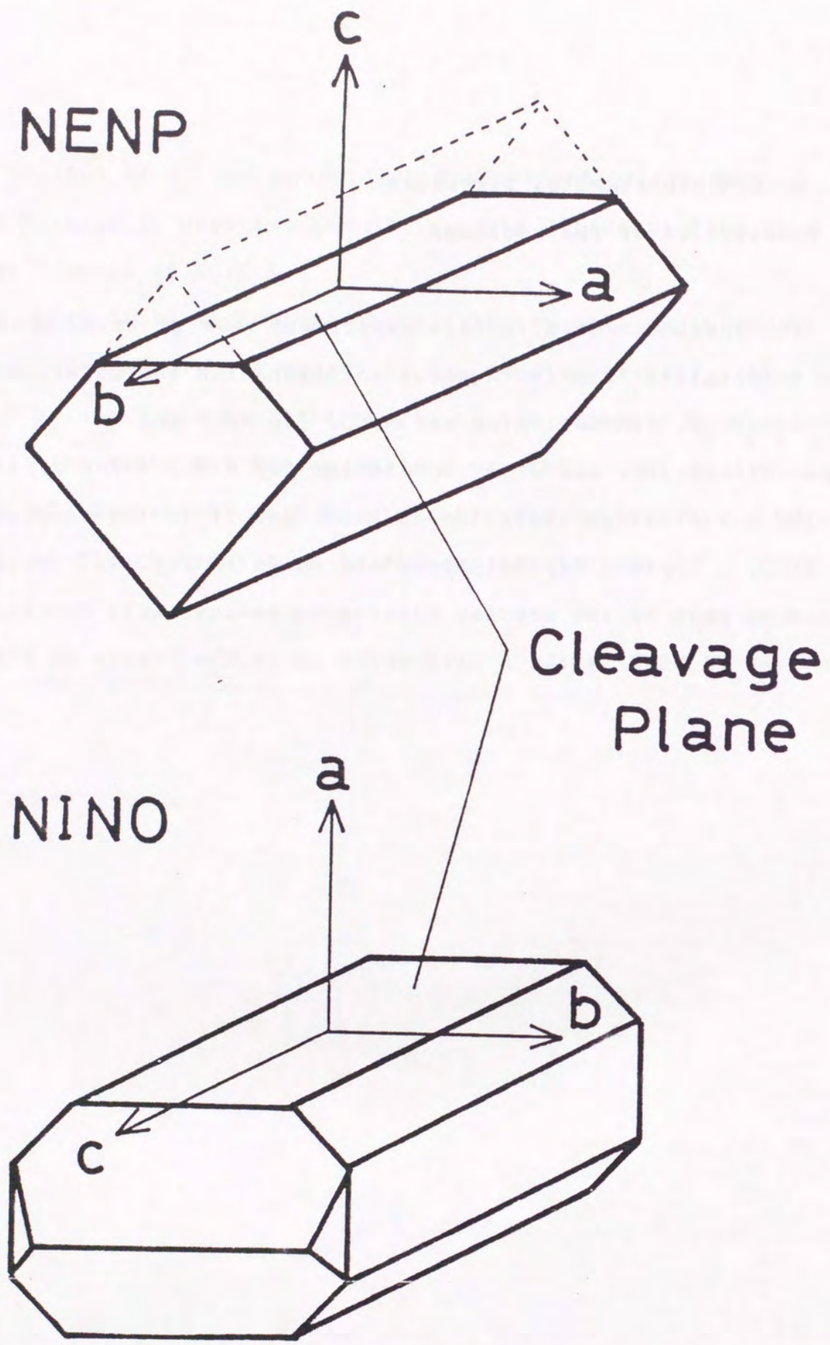

Fig. 4. Sketch of single crystals NENP and NINO.

4.2 Microwave equipment in pulsed high magnetic field

The block diagram of microwave ESR in pulsed magnetic field is shown in Fig. 1 of Part I. Microwave used for the experiment is the frequency ranges of 35 and 50 GHz bands, generated by klystrons 35V10 and 50V11, respectively. Standard experimental apparatus and techniques are used to observe the resonance in NENP and NINO. The reflection type of cylindrical cavity with TE_{11n} mode with n of 2~3 is adopted for the measurements.

The high magnetic field microwave ESR measurements are done in the Research Center for Extreme Materials of Osaka University. The magnet coil is the type of 170(2LP)18, which is A-type coil in Part I and has outer diameter of 170 mm and inner one of 18 mm with energy source of 0.5 MJ. This can produce magnetic field up to 41 T with the pulse duration of 40 msec. The magnetic field is monitored by a field pick-up coil and recorded in the digital recorder. The field value is calibrated with ESR signal of DPPH.

5 Experimental results

Only a broad paramagnetic resonance is found from room temperature down to 30～35 K with g=2.0, and it is understood by exchange-mixed paramagnetic resonance[21] where the fine structure components are amalgamated by the intrachain exchange interaction. Figure 5 shows the signal with the DPPH spike. Paramagnetic resonance disappears around 20 K.

A new resonance line with a width of 1 T is found below 20～25 K where the paramagnetic resonance disappears, as is seen in Fig. 5. The absorption intensity decreases below 7 K and the temperature dependence is given in Fig. 6. The result shows that the signal comes from excited states. Solid curve in Fig. 6 is calculated by spin-cluster resonance model[22], as will be discussed in the section 6. The temperature dependence of the intensity shows a good agreement with the spin-cluster excitation model. Angular dependences of the resonance field in NENP and NINO are shown in Figs. 7, 8 and 9. The angle in the ac-plane is defined by θ and the deviation angle from the ac-plane is denoted by ϕ. Figure 10 represents typical angular dependence of the resonance lines in NINO. In NENP, the resonance is broadened out when the angle ϕ becomes larger than 10 degrees, as is shown in Fig. 11. All solid curves in Figs. 7, 8, 9 and 11 are calculated curves by using an effective spin Hamiltonian described later. Weak absorption is found as shown in Fig. 12 when the field is applied along b-axis.

The observed new line is not explained by the standard

antiferromagnetic resonance (AFMR) model. The usual AFMR theory does not expect the decrease in the absorption intensity with decreasing temperature.

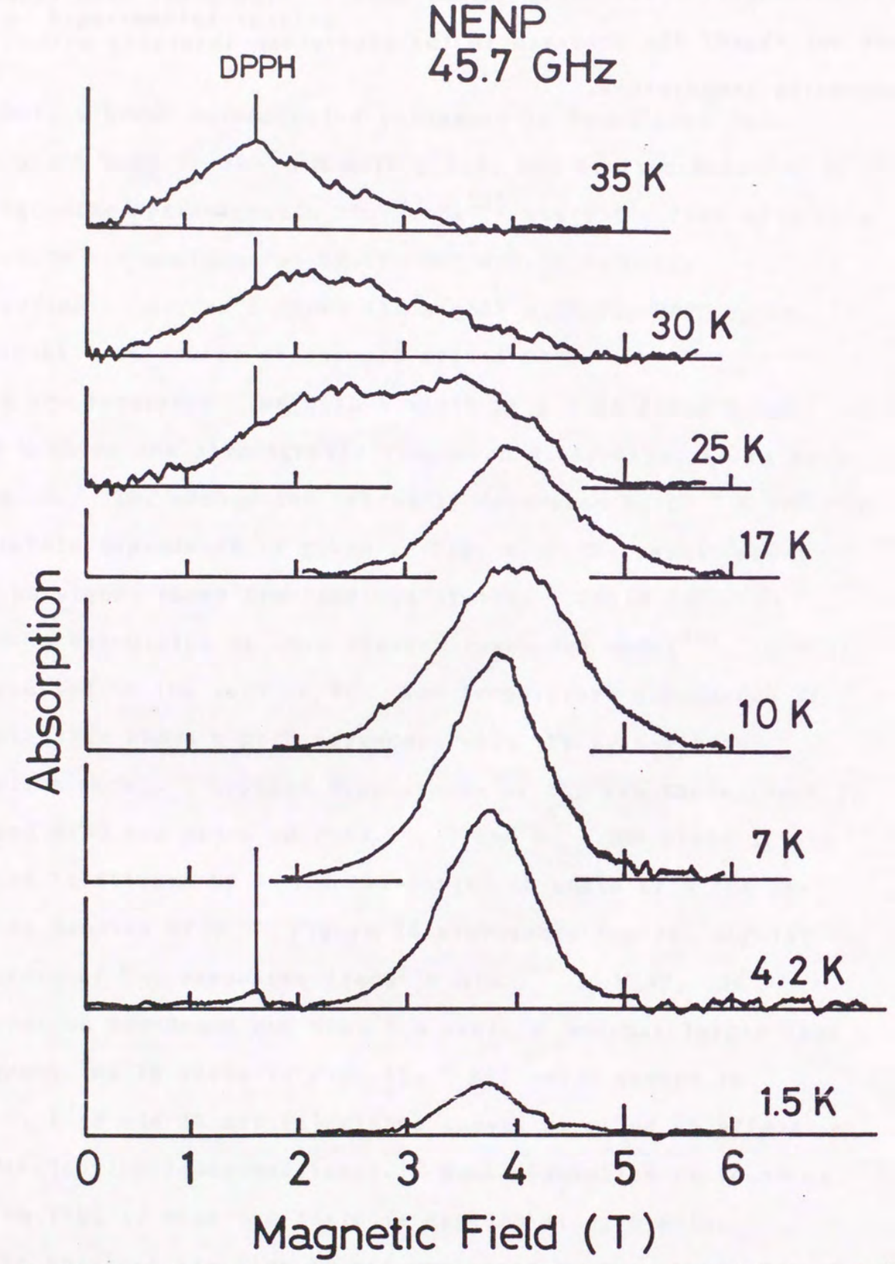

Fig. 5. Temperature dependence of the ESR signal in NENP on a relative scale. Magnetic field is applied in the ac plane at an angle of 30 degrees from the a-axis.

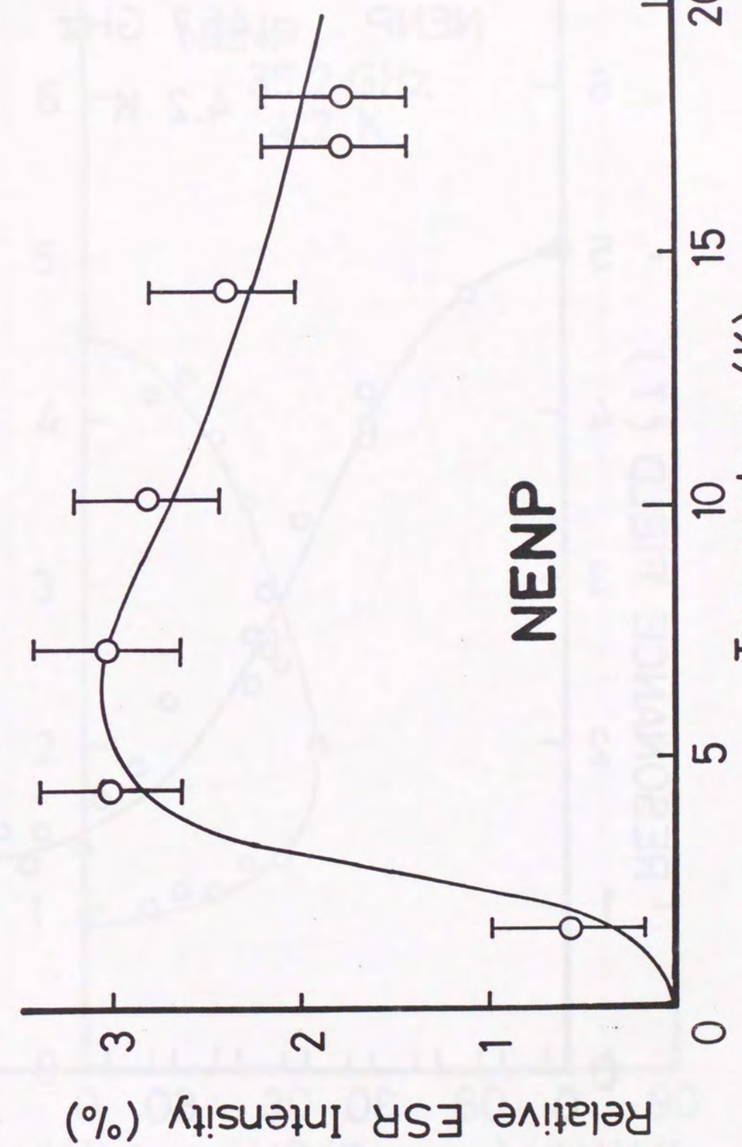

Fig. 6. Temperature dependence of the ESR intensity. % denotes the effective percentage of spins responsible for ESR.

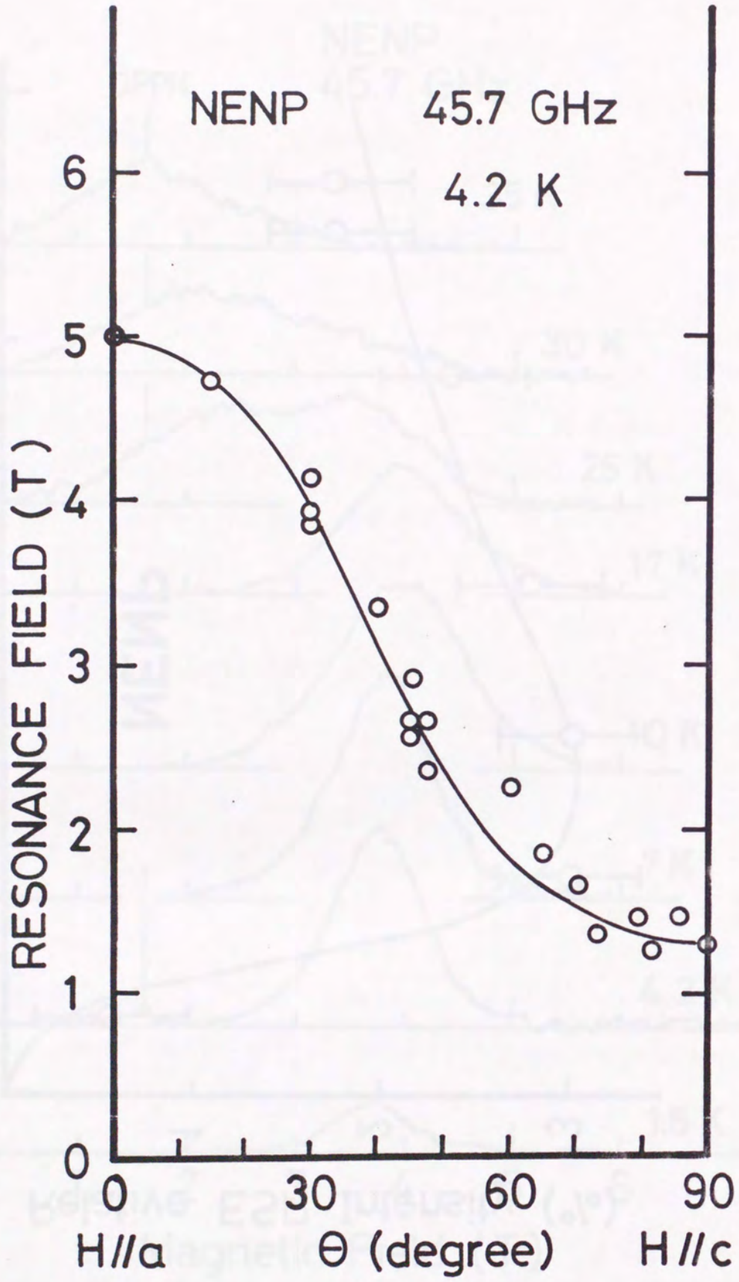

Fig. 7. Angular dependence of the resonance field in NENP at 45.7 GHz. Solid curve is drawn by eq. (6).

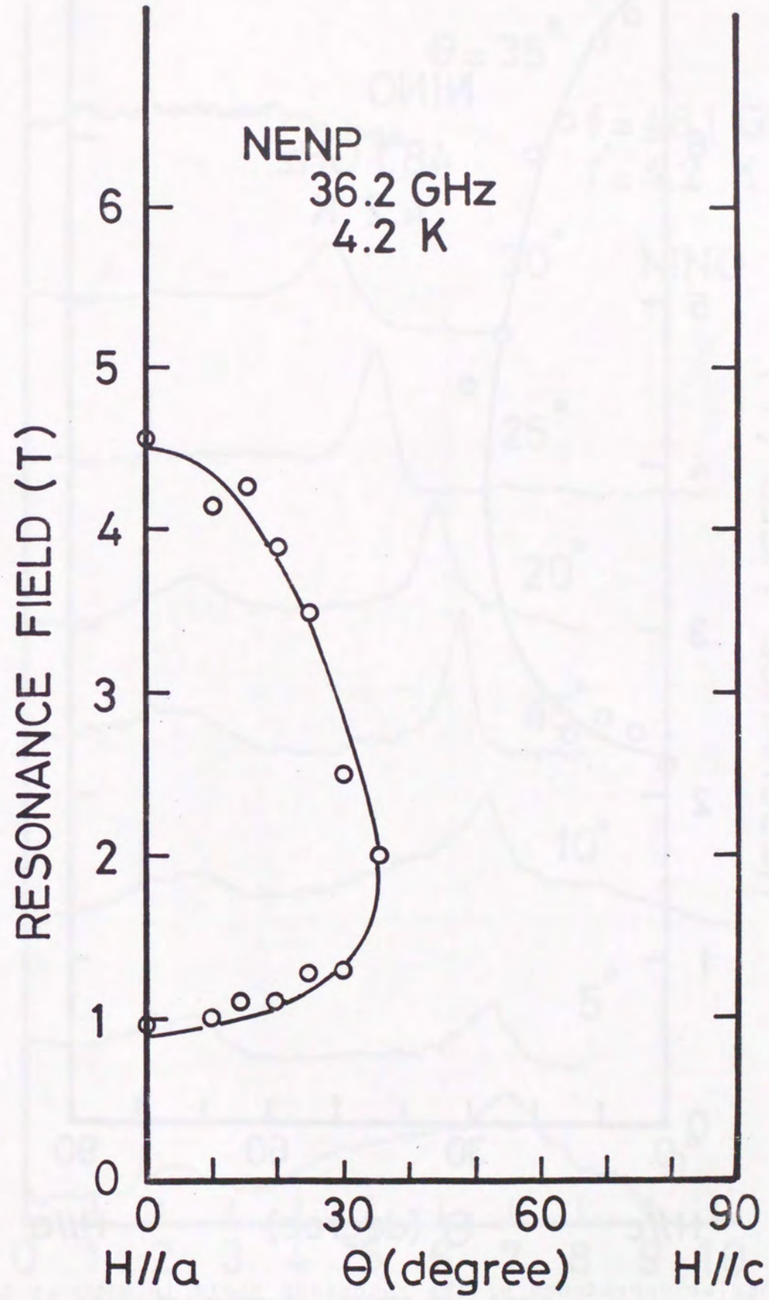

Fig. 8. Angular dependence of the resonance field in NENP at 36.2 GHz. Solid curve is drawn by eq. (6).

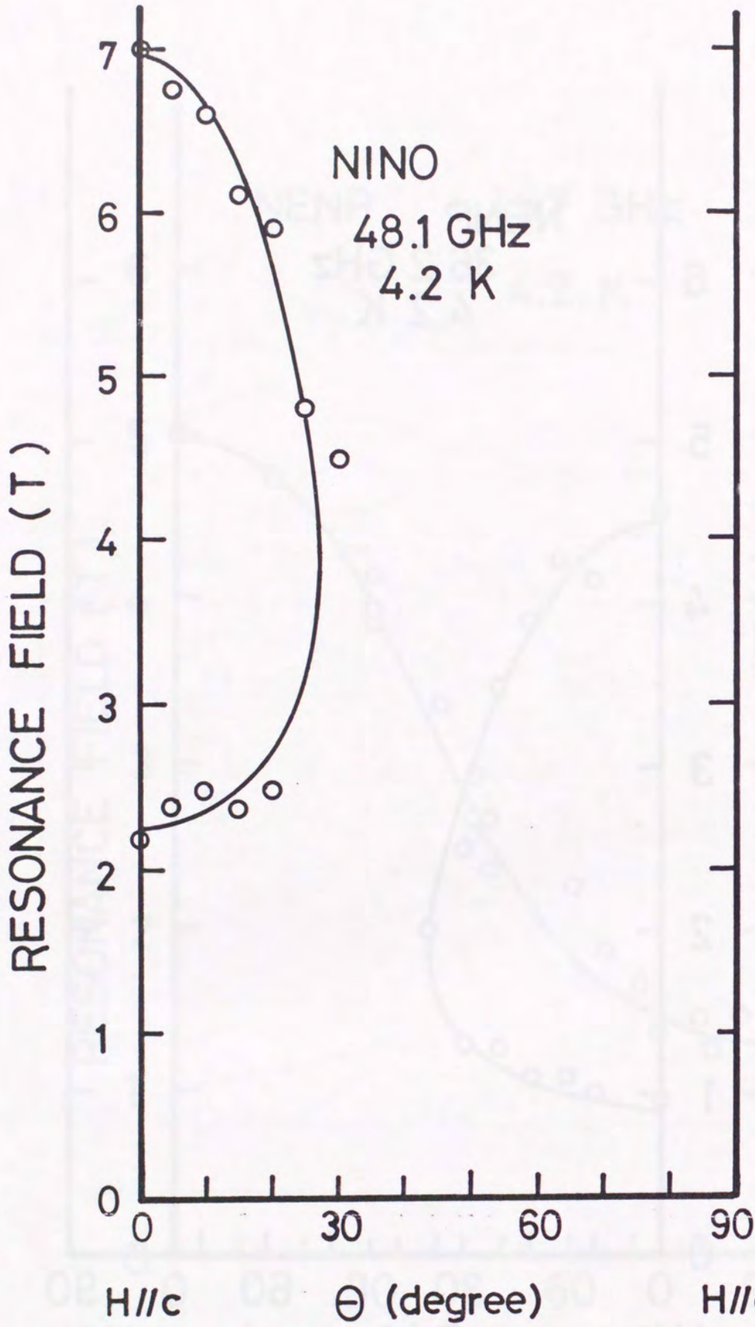

Fig. 9. Angular dependence of the resonance field in NINO at 48.1 GHz. Solid curve is drawn by eq. (6).

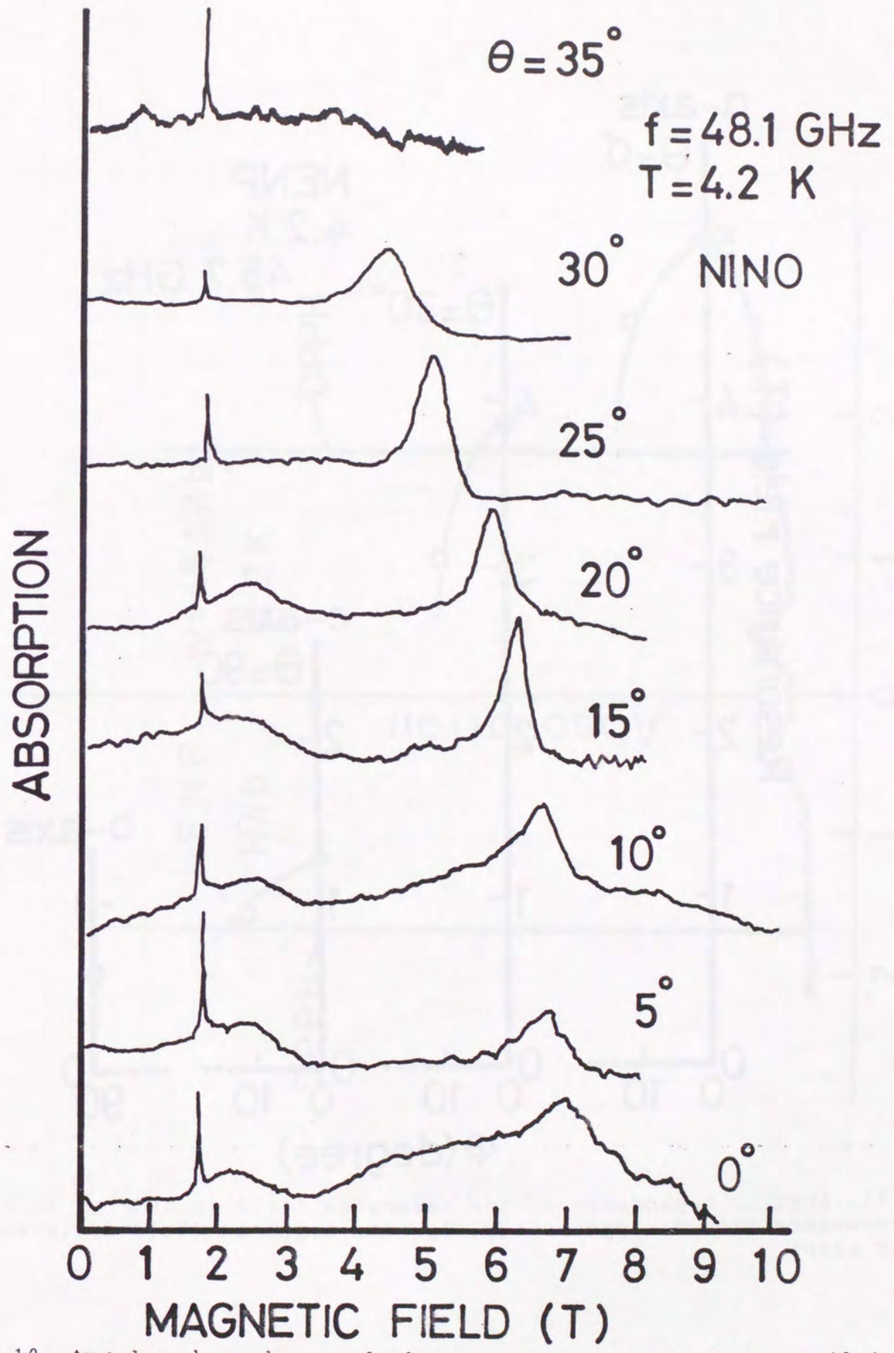

Fig. 10. Angular dependence of the resonance line in NINO at 48.1 GHz. magnetic field is applied in the ac plane.

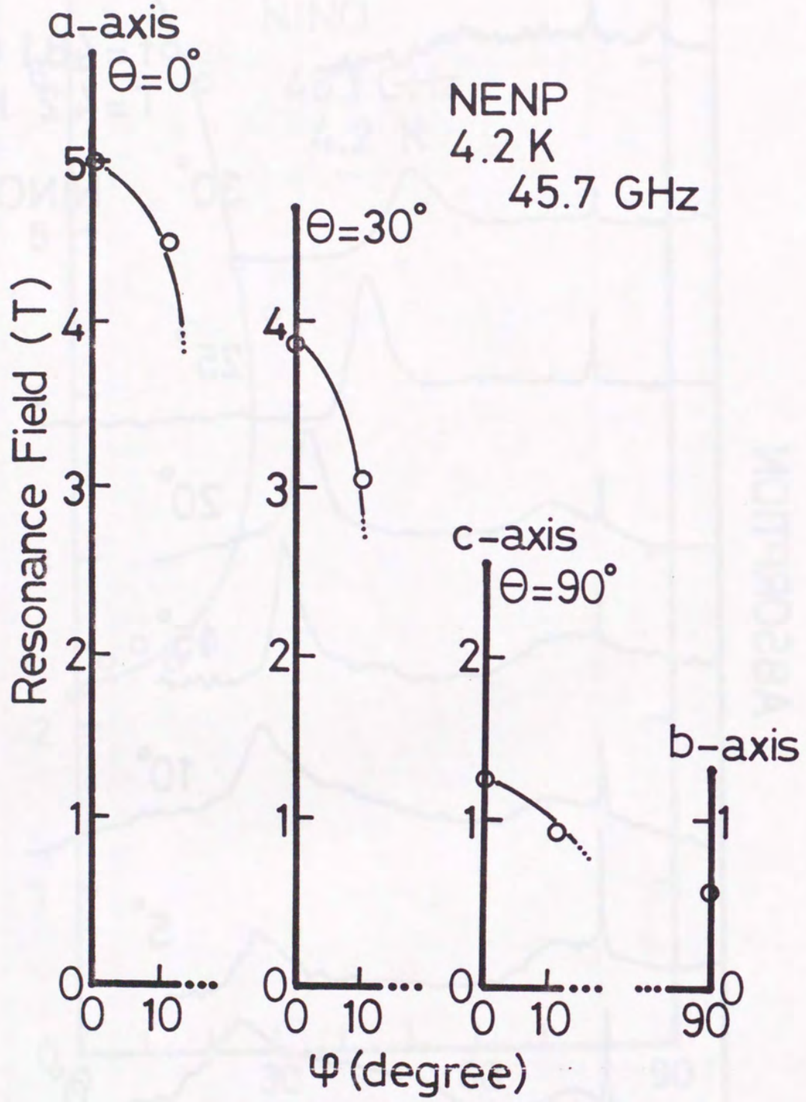

Fig. 11. Angular dependence of the resonance field in NENP at 45.7 GHz. The resonance line disappears rapidly when magnetic field deviates from the ac plane.

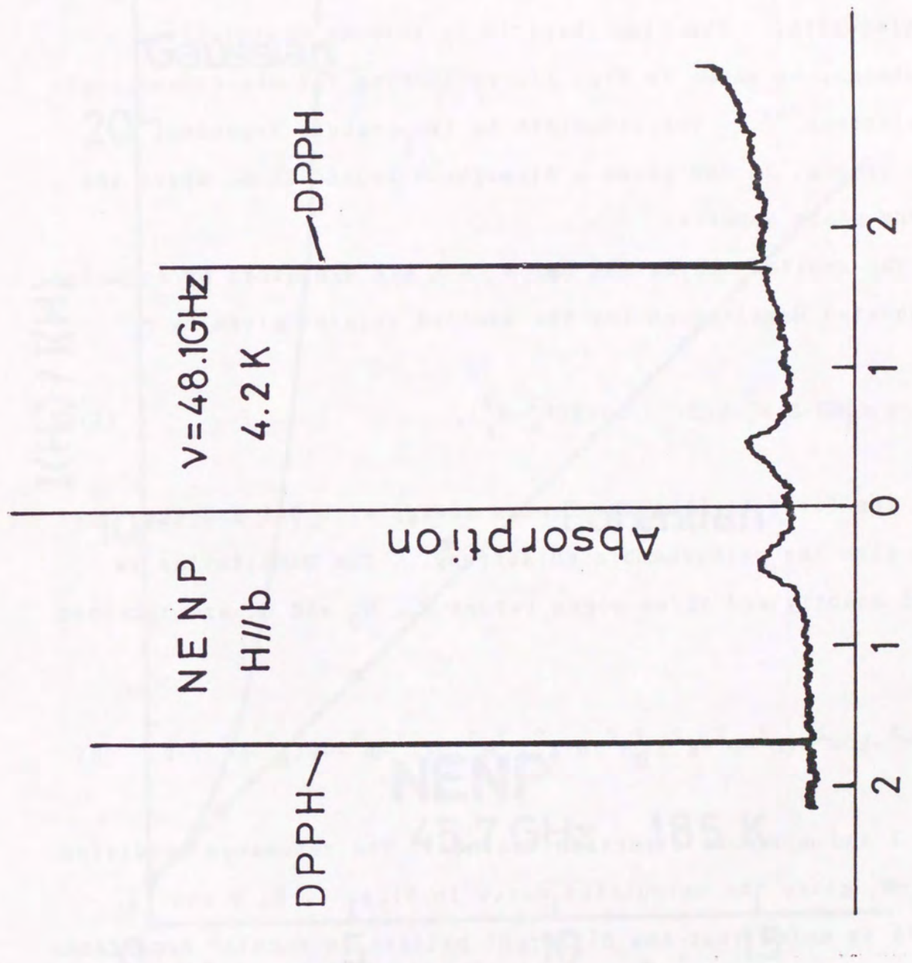

Fig. 12. The resonance line in NENP at 48.1 GHz. Magnetic field is aplied along the b-axis.

6 Analysis and discussions

The paramagnetic resonance is examined in the line shape and the linewidth. The line shape is in between Gaussian and Lorentzian, as shown in Fig. 13, reflecting the one-dimensional correlations[23]. The linewidth is temperature dependent as shown in Fig. 14 and shows a divergence around 20 K, where the Haldane state appears.

The excited states ESR below 20 K are explained by assuming a truncated Hamiltonian for the excited triplet given by

$$\mathcal{H} = g\mu_B SH + D(S_z^2 - S(S+1)/3) + E(S_x^2 - S_y^2), \qquad (5)$$

where the first term is the Zeeman energy with S=1 and the other terms give the orthorhombic anisotropy. The Hamiltonian is solved exactly and three eigen values W_1, W_2 and W_3 are obtained from

$$W^3 - 2DW^2 - (E^2 - D^2 + g^2\mu_B^2H^2)W + g^2\mu_B^2H^2\{D(l^2+m^2) - E(l^2-m^2)\} = 0, \qquad (6)$$

where l and m denote direction cosine. The resonance condition $h\nu = W_i - W_j$ gives the calculated curve in Figs. 7, 8, 9 and 11.

It is noted that the different pattern in angular dependence is observed in Figs. 7~9. The absorption along the a-axis is found at 5 T in NENP as shown in Fig. 9, while no corresponding resonance is found in NINO as shown in Fig. 11, where the resonance shows a loop in the ac-plane and similar pattern is

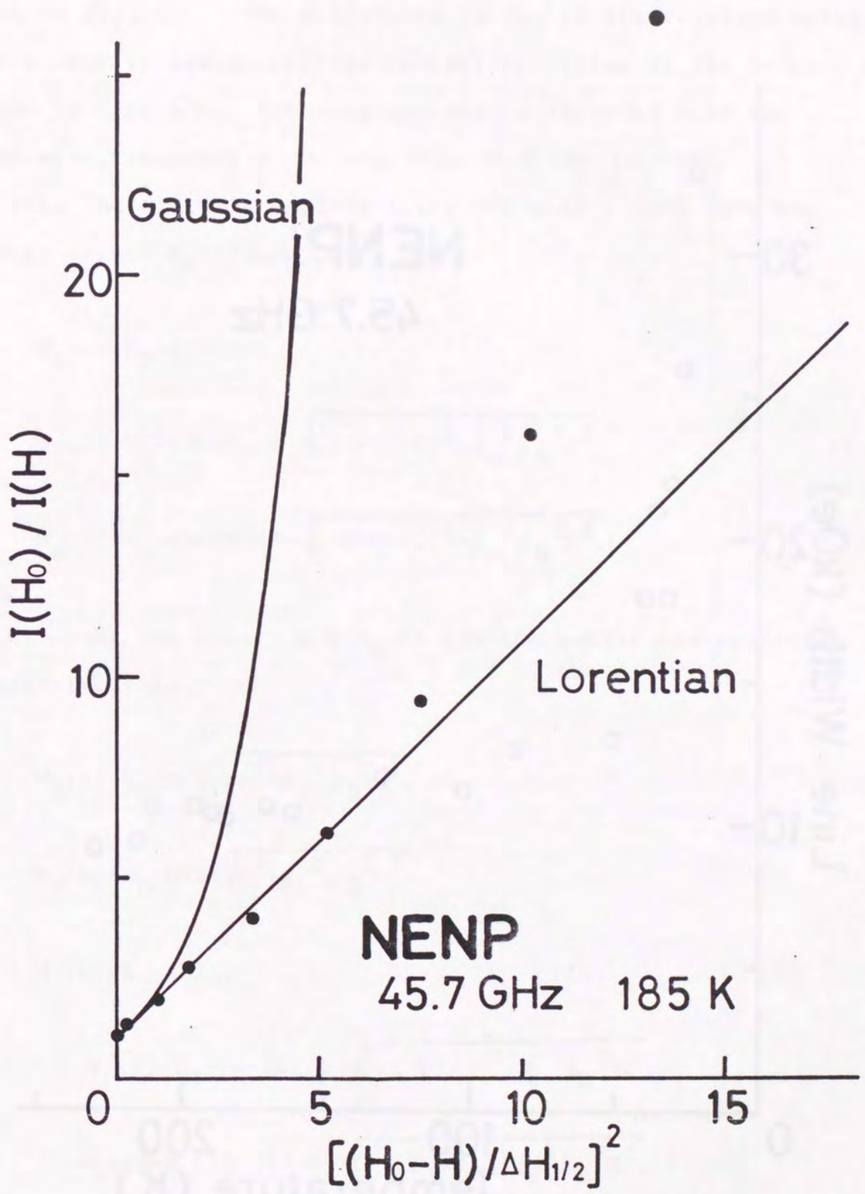

Fig. 13. Line shape of paramagnetic resonance in NENP at 185 K.

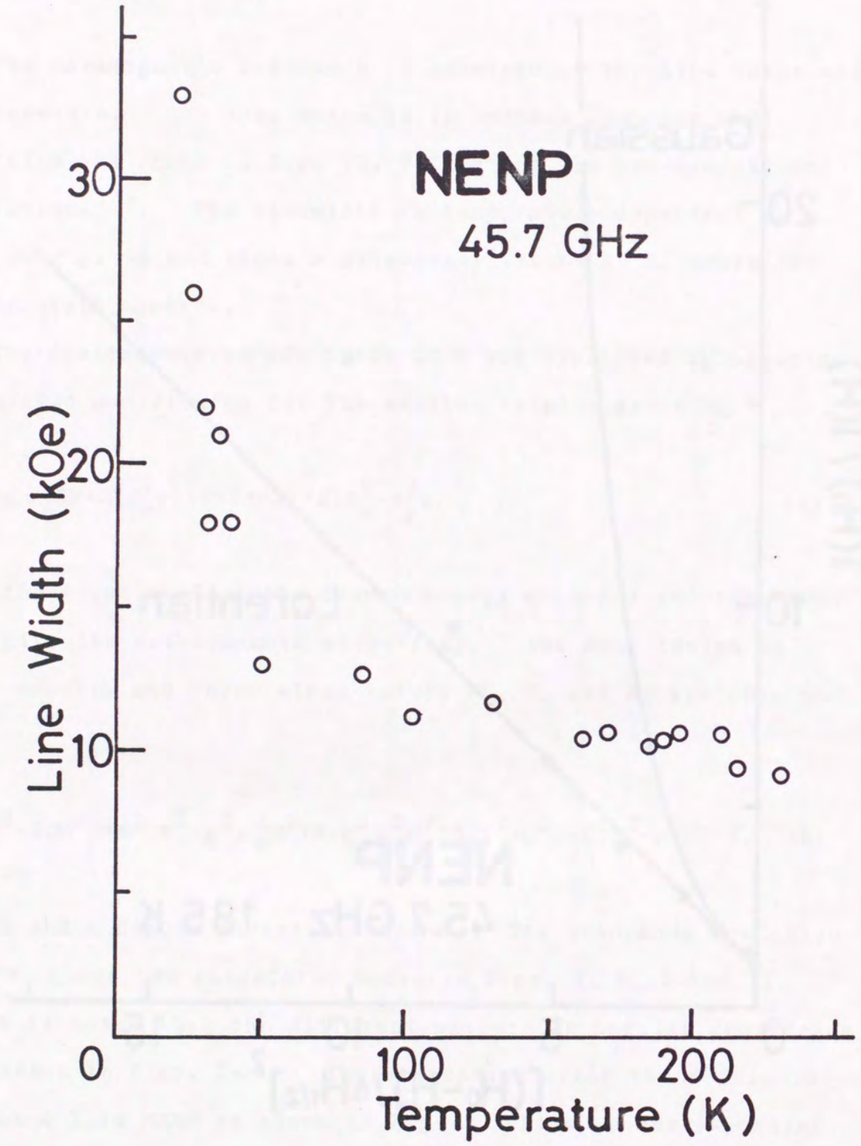

FIg. 14. Temperature dependence of the linewidth in paramagnetic resonance of NENP.

seen in Fig. 10. The difference is due to the relation between the microwave energy and the initial splitting by the E-term, as shown in Fig. 15. The loop-pattern is expected when the microwave frequency ν is less than 37.5 GHz in NENP.

When the field is applied along the a-axis, the obtained energy levels $W_n(a)$ are given by

$$W_1(a)=E_G+D/3+E, \tag{7}$$

$$W_2(a)=E_G-(D+3E)/6-\sqrt{\{(E-D)/2\}^2+g_a^2\mu_B^2H^2}\ , \tag{8}$$

$$W_3(a)=E_G-(D+3E)/6+\sqrt{\{(E-D)/2\}^2+g_a^2\mu_B^2H^2}. \tag{9}$$

$W_n(b)$ along the b-axis and $W_n(c)$ for the c-axis are obtained respectively as

$$W_1(b)=E_G+D/3-\sqrt{E^2+g_b^2\mu_B^2H^2}, \tag{10}$$

$$W_2(b)=E_G+D/3+\sqrt{E^2+g_b^2\mu_B^2H^2}, \tag{11}$$

$$W_3(b)=E_G-2D/3, \tag{12}$$

$$W_1(c)=E_G-(D-3E)/6-\sqrt{\{(E+D)/2\}^2+g_c^2\mu_B^2H^2}, \tag{13}$$

$$W_2(c)=E_G-(D-3E)/6+\sqrt{\{(E+D)/2\}^2+g_c^2\mu_B^2H^2}, \tag{14}$$

$$W_3(c)=E_G+(D-3E)/3, \tag{15}$$

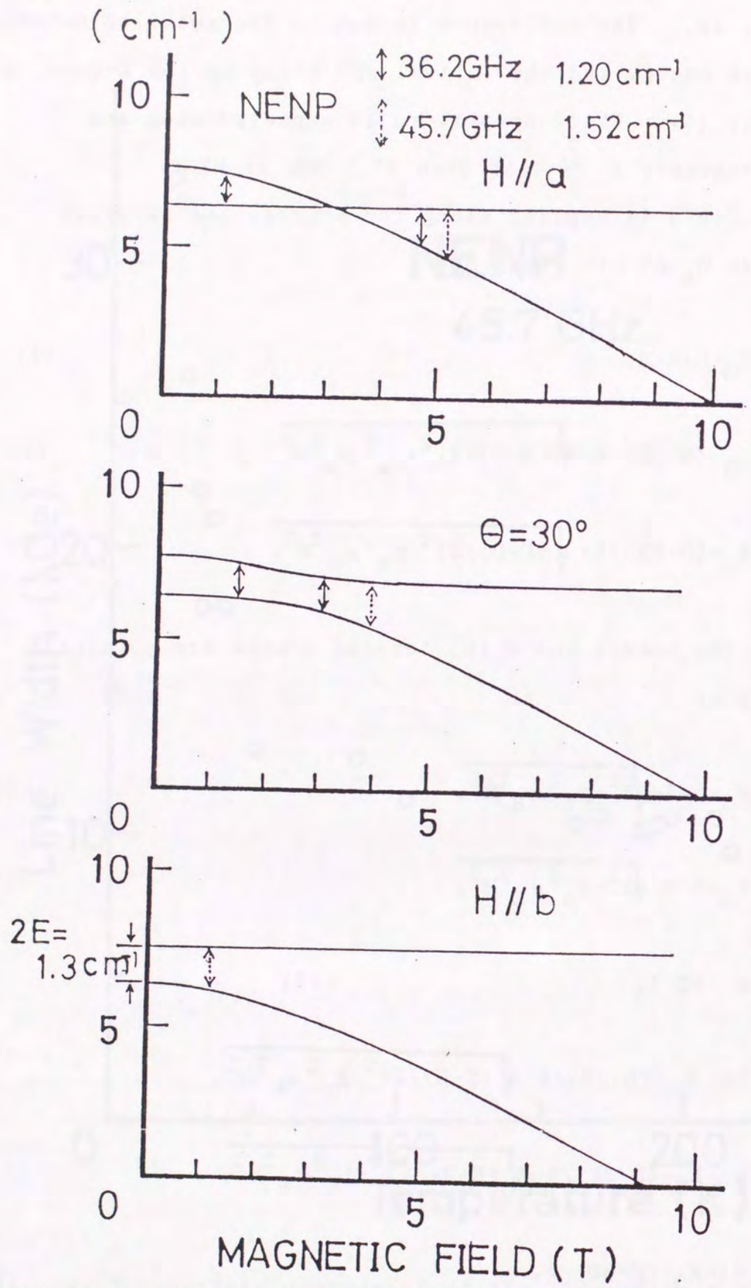

Fig. 15. Energy level scheme in NENP. Solid arrow denotes the magnetic field where microwave absorptions at 36.2 GHz are seen and dotted arrow is for that at 45.7 GHz.

where the center of the triplet is above the Haldane ground state with energy E_G. The obtained energy level diagram associated with the gap is shown in Fig. 16. The energy level scheme is confirmed by recent high frequency ESR in the several hundred GHz region[24),25)]. The Haldane ground state is shown by the zero-energy line and the excited triplet at E_G splits by D and E terms into three singlets at zero magnetic field. These levels show the field dependences and the crossover to the ground state occurs for each low-lying level at the corresponding critical field. The microwave transitions R_a, R_b and R_c are experimentally observed but R_b' and R_b'' are not detected. The results are consistent with the gap model because levels in the spin-wave continuum are usually broadened so that no resonance is expected. The observed R_b intensity is weak because this resonance is allowed by the E-term, which is small compared with the D-term.

The parameters obtained from various experiments are summarized in Table 1. The gap energy in Table 1 is obtained by using the critical-field formulae (2) and (4) by adding the E-term as

$$H_T^a = \sqrt{(E_G-2D/3)(E_G+D/3-E)} \;/\; g_a\mu_B \,, \tag{16}$$

$$H_T^b = \sqrt{(E_G+D/3+E)(E_G+D/3-E)} \;/\; g_b\mu_B \,, \tag{17}$$

$$H_T^c = \sqrt{(E_G-2D/3)(E_G+D/3+E)} \;/\; g_c\mu_B \,. \tag{18}$$

Table 1. Summary of obtained parameters in NENP and NINO.

	E_G (cm^{-1})	D (cm^{-1})	E (cm^{-1})	H_T^a (T)	H_T^b (T)	H_T^c (T)
NENP	9.5	-7.5	-0.67	10.1/10.5#	7.0/7.0	9.2/9.0
NINO	9.5	-11.5	1.05	8.5/7.8	5.6/5.8	10.4/10.6

obtained parameter from ESR / from magnetization measurements.

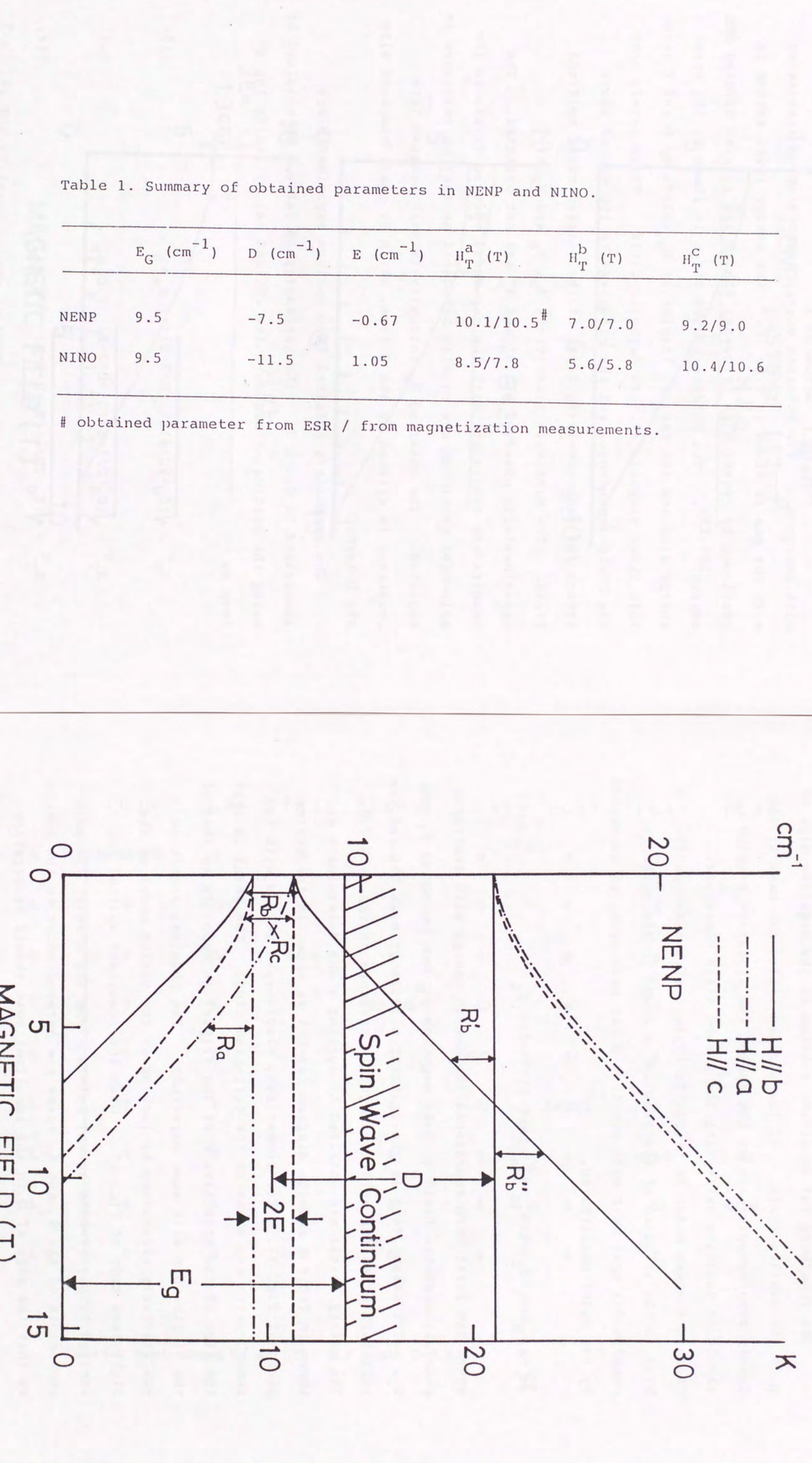

Fig. 16. Energy level diagram under a magnetic field. The field dependence of spin-wave continuum is not shown.

The remaining but important problem is the negative sign of D in the excited state. If the excited states are made of the freely running spin wave on the chain, the effective D-value should be positive reflecting the ground state character. Therefore a new model is needed to explain this discrepancy. A hint to the solution of the problem is found in the exchange coupled S=1 spin pair with positive D for each spin, as expressed by the model Hamiltonian,

$$\mathcal{H} = g\mu_B H(S_1+S_2) + D(S_{1z}^2 + S_{2z}^2 - 2S(S+1)/3) - 2JS_1S_2 \qquad (19)$$

where the first term represents the Zeeman energy with isotropic g-value, magnetic field H, Bohr magneton μ_B for two spins S_1 and S_2. The second term is the uniaxial anisotropy with D>0 and the last term shows the antiferromagnetic exchange energy with J<0. The energy levels are obtained by solving a 9X9 determinant as shown in Table 2 and the diagram for H=0 is shown in the center panel of Fig. 17. For comparison, single-spin levels with the same D-value are shown on the left-hand side. The point is that the sign of the effective D of the triplet is opposite to that of the single spin with same magnitude. The physical reason is qualitatively understood by looking at the vector model on the right-hand side of Fig. 17. When the resultant spin of the excited triplet (white arrow) points along the z-axis, the main components of the S_1 and S_2 spins are perpendicular to the z-axis so that the sign of D in the resultant spin should be negative.

With this in mind, the vector model of the excited triplet

	|1, 1\>	|1, 0\>	|0, 1\>	|1,-1\>	|0, 0\>	|1,-1\>	|0,-1\>	|-1, 1\>	|-1, 0\>	|-1,-1\>
<1, 1|	-2J+2D/3+2G	0	0	0	0	0	0	0	0	0
<1, 0|	0	-D/3+G	-2J	0	0	0	0	0	0	0
<0, 1|	0	-2J	-D/3+G	0	0	0	0	0	0	0
<1,-1|	0	0	0	2J+2D/3	-2J	0	0	0	0	0
<0, 0|	0	0	0	-2J	4D/3	-2J	0	0	0	0
<1, 1|	0	0	0	0	-2J	2J+2D/3	0	0	0	0
<0,-1|	0	0	0	0	0	0	-D/3+G	-2J	0	0
<1, 0|	0	0	0	0	0	0	-2J	-D/3+G	0	0
<1,-1|	0	0	0	0	0	0	0	0	0	-2J+2D/3+2G

Table 2-1. Matrix element for eq. (19). H // z-axis. G= $g_n\mu_n$H.

	| 1, 1 >	| 1, 0 >	| 0, 1 >	| 1,-1 >	| 0, 0 >	|-1, 1 >	| 0,-1 >	|-1, 0 >	|-1,-1 >
< 1, 1 |	-2J+2D/3	G/√2	G/ √2	0	0	0	0	0	0
< 1, 0 |	G/√2	-D/3	-2J	G/√2	G/√2	0	0	0	0
< 0, 1 |	G/√2	-2J	-D/3	0	G/√2	G/ √2	0	0	0
< 1,-1 |	0	G/√2	0	2J+2D/3	-2J	0	G/√2	0	0
< 0, 0 |	0	G/√2	G/√2	-2J	-4D/3	-2J	G/√2	G/√2	0
< 1, 1 |	0	0	G/√2	0	-2J	2J+2D/3	0	G/√2	0
< 0,-1 |	0	0	0	G/√2	G/√2	0	-D/3	-2J	G/√2
< 1, 0 |	0	0	0	0	G/√2	G/√2	-2J	-D/3	G/√2
< 1,-1 |	0	0	0	0	0	0	G/√2	G/√2	-2J+2D/3

Table 2-2. Matrix element for eq. (19). H // x-axis, G= $g_{\perp}\mu_B H$.

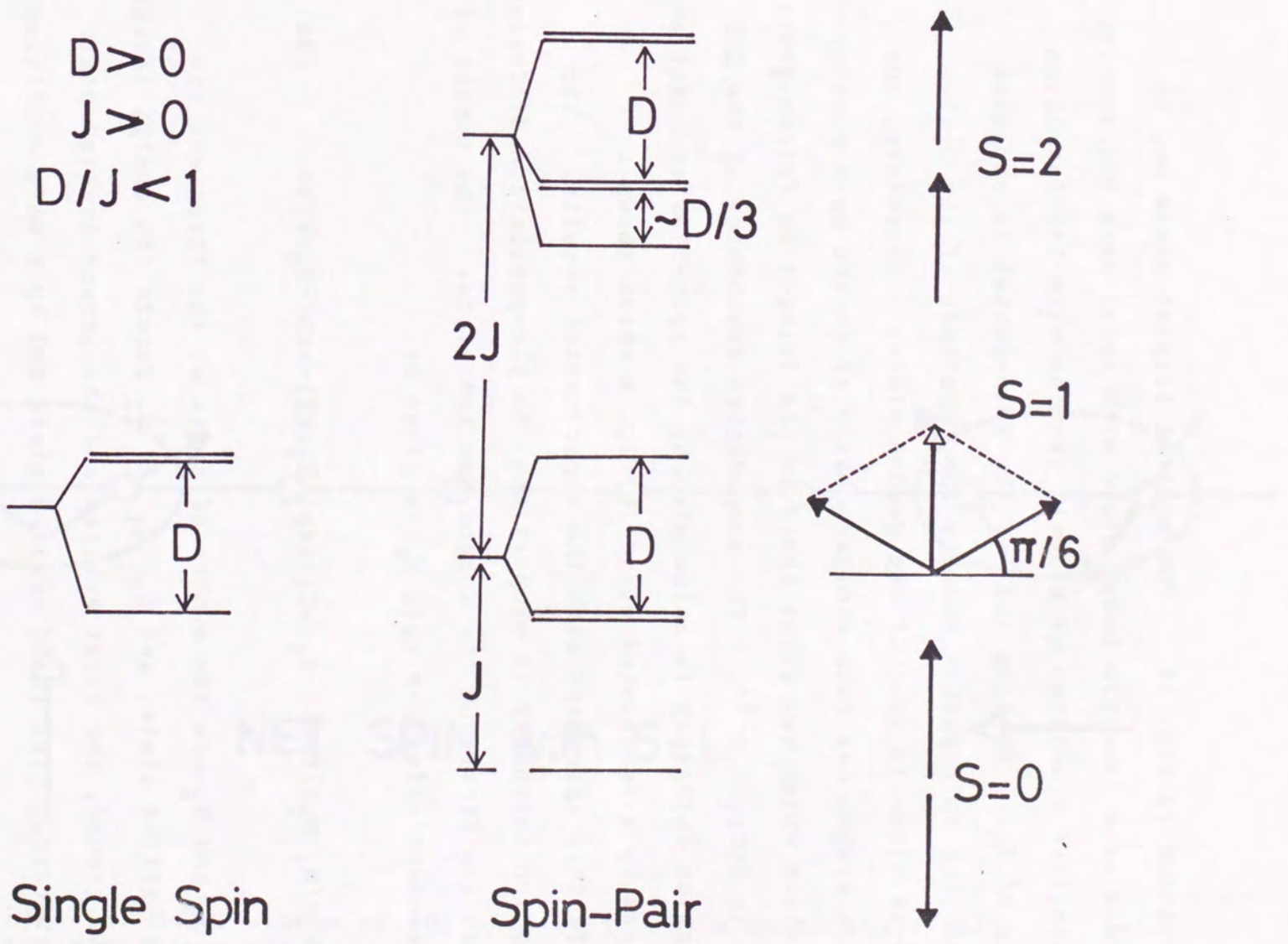

Fig. 17. Energy level splittings for single-spin and spin-pair states.

is sketched in Fig. 18. The excited triplet state may be regarded as a two-spin bound state with total spin S=1 running in a chain like a soliton or a small exciton with the formation energy of E_G. No long tail of the spin-packet is expected because the spin-packet reduces the magnitude of the D-term, which is close to that of the ground state. Therefore, the excited states may have similar character to the spin cluster excitation which was first found in the Ising-like ferromagnetic chain in $CoCl_2 2H_2O$[22]. The temperature dependence of the ESR absorption intensity is calculated by the spin-cluster model as is shown by a calculated curve in Fig. 6 which shows a satisfactory agreement with the experimental results. The absorption intensity is proportional to the population difference between the first and the second excited state. The number of the resonant effective spin N_e is given by

$$N_e=(N_1-N_2)/(\exp(-E_0/kT)+\exp(-E_1/kT)+\exp(-E_2/kT)) \qquad (20)$$

where N_1 and N_2 are the number of spins at the first and the second excited state, and E_0, E_1 and E_2 denote the energy levels for the ground, the first excited and the second excited state, respectively. The third excited state and spin wave continuum are neglected for low temperatures. These factors become important for the intensity at high temperatures so that a deviation between the theory and the experimental can be seen above 15 K. Putting these energy levels into eq (20), the absorption intensity can be obtained as a function of

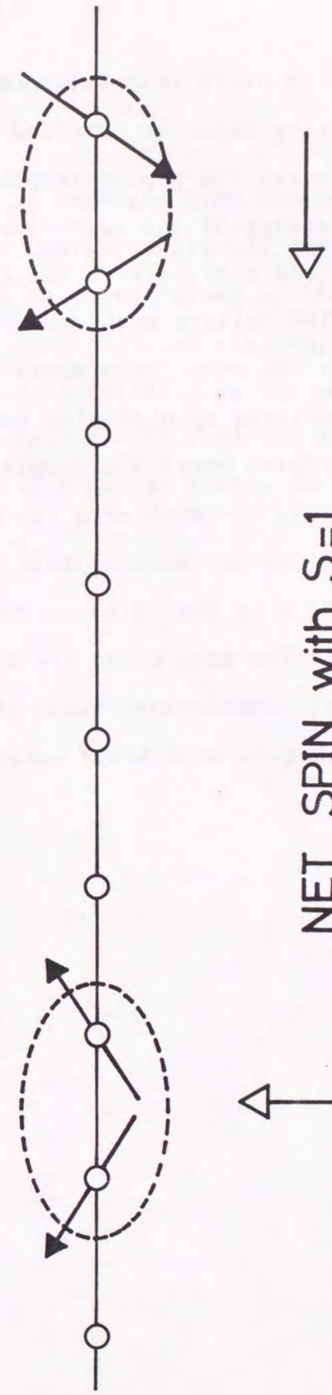

Fig. 18. Model scheme of the excited two-spin bound state with the resultant spin S=1.

temperature. It is noted that the number of localized spin clusters in the Ising chain is obtained by a bosonlike excitation model where the excitation gap corresponding to E_G is $2JS^2$, which is the formation energy of the spin-cluster in a chain. In addition to E_G, D and E terms with the Zeeman energy are taken into account for the Haldane problem. The following difference should be noticed: The mean field model is applicable for calculation of the Ising spin cluster energy while it is not used for the Haldane triplet where the coupling is defined by E_G, which is difficult to estimate with the mean field model.

The present model may also explain the susceptibility crossover around 35 K in Fig. 2(A). The main excitation at low temperatures is the two-spin bound state with negative D while it is positive at high temperatures where the system can be regarded as usual antiferromagnet with short range order.

7. Conclusion

The high-field ESR in NENP and NINO has been done and the excited state ESR in the Haldane state has been observed. The excited triplet state is well understood by the localized two-spin bound model as the elementary excitation. The Haldane state should be described essentially by the many-body quantum effect but the excited state can be sketched as if the excitation is given by a truncated spin packet like a soliton.

REFERENCES

1) H.Bethe: Z. Phys. 71 (1931) 205.

2) J.C.Bonner and M.E.Fisher: Phys. Rev. 135 (1964) A640.

3) D.M.Haldane: Phys. Rev. Lett.: 50 (1983) 1153.

4) Botet, R.Jullien and M.Kolb: Phys. Rev. B28 (1983) 3914.

5) J.B.Parkinson and J.C.Bonner: J. Appl. Phys. 61 (1987) 3941.

6) M.P.Nightingale and H.W.J.Blöte: Phys. Rev. B31 (1986) 659.

7) M.Takahashi: Phys. Rev. Lett. 62 (1989) 2313.

8) T.Sakai and M.Takahashi: Phys. Rev. B43 (1991) 13383.

9) I.Affleck, T.Kennedy, E.H.Lieb and H.Tasaki: Phys. Rev. Lett. 59 (1987) 799.

10) I.Affleck: Phys. Rev. Lett. 62 (1989) 474.

11) W.J.L.Buyers, R.M.Morra, R.L.Armstrong, M.J.Hogan, P.Gerlach and K.Hirakawa: Phys. Rev. Lett. 56 (1986) 371.

12) M.Steiner, K.Kakurai, J.K.Kjems, D.Petitgrand and R.Pynn: J. Appl. Phys. 61 (1987) 3953.

13) J.P.Renard, M.Verdaguer, L.P.Regnault, W.A.C.Erkelens, J.Rossat-Mignod, J.Ribas, W.G.Stirling and C.Vettier: J. Appl. Phys. 63 (1988) 3538.

14) K.Katsumata, H.Hori, T.Takeuchi, M.Date, A.Yamagishi and J.P.Renard: Phys. Rev. Lett. 63 (1989) 86.

15) Y.Ajiro, T.Goto, H.Kikuchi, T.Sakakibara and T.Inami: Phys. Rev. Lett. 63 (1989) 1424.

16) Hagiwara, K.Katsumata, I.Affleck, B.I.Halperin and J.P.Renard: Phys. Rev. Lett. 65 (1990) 3181.

17) A.Meyer, A.Gleizes, J.J.Girerd, M.Verdaguer and O.Kahn: Inorg. Chem. 21 (1982) 1729.

18) T.Takeuchi, M.Ono, H.Hori, T.Yosida, A.Yamagishi and M.Date, to be published in J. Phys. Soc. Jpn.

19) J.Ferré, J.P.Jamet, C.P.Landeé, K.A.Reza and J.P.Renard: J. de Phys. 49 (1988) c8-1441.

20) M.Chiba, Y.Ajiro, H.Kikuchi, T.Kubo and T.Morimoto: J. Magn. & Magn. Mat. 90&91 (1990) 221.

21) M.Date and M.Motokawa: J. Phys. Soc. Jpn. 22 (1967) 165.

22) M.Date and M.Motokawa: Phys. Rev. Lett. 16 (1966) 1111.

23) R.E.Dietz, F.R.Merritt, R.Dingle, D.Hone, D.G.Shilbernagel and P.M.Richards: Phys. Rev. Lett. 26 (1971) 1186.

24) W.Lu, J.Tuchendler, M.von Ortenberg and J.P.Renard: to be published in Physica B.

25) W.Palme, O.Born, H.Kriegelstein, B.Lüthi, M.Enderle and M.Steiner: to be published in J. Magn. & Magn. Mat.

ACKNOWLEDGEMENTS

The author wishes to express his sincere gratitude to Professor Muneyuki Date for his valuable suggestions and enlightening discussions, and his continuous encouragement throughout the present work. Thanks are also due to Professor Mitsuhiro Motokawa of Kobe University for his valuable suggestions on the techniques of high-field ESR.

The author would like to thank Professor Akio Yamagishi of the Research Center for Extreme Materials, Osaka University for many helpful suggestions on use of long-pulse magnet. He would also like to thank Doctor Taturu Yosida of Low Temperature Center, Osaka University for supplying single crystals of NENP and NINO.

He is indebted to Mr. Tetsuya Takeuchi and Mr. Mitsuru Ono for the cooperation in analysis of the magnetization and magnetic susceptibility results. He is also indebted to Mr. Kunihiro Senda for the cooperation in development of high-field ESR systems. Finally, the author wishes to thank all the members of Date laboratory.